EXPERIMENTAL AND THEORETICAL INVESTIGATION OF NUCLEATION AND GROWTH OF ATMOSPHERIC AEROSOLS

A Dissertation

by

JUN ZHAO

Submitted to the Office of Graduate Studies of
Texas A&M University
in partial fulfillment of the requirements for the degree of

DOCTOR OF PHILOSOPHY

December 2007

Major Subject: Atmospheric Sciences

EXPERIMENTAL AND THEORETICAL INVESTIGATION OF NUCLEATION AND GROWTH OF ATMOSPHERIC AEROSOLS

A Dissertation

by

JUN ZHAO

Submitted to the Office of Graduate Studies of
Texas A&M University
in partial fulfillment of the requirements for the degree of

DOCTOR OF PHILOSOPHY

Approved by:

Chair of Committee, Renyi Zhang
Committee Members, Don R. Collins
Robert A. Duce
Robert L. McGraw
Simon W. North
Head of Department, Richard E. Orville

December 2007

Major Subject: Atmospheric Sciences

ABSTRACT

Experimental and Theoretical Investigation of Nucleation and Growth of Atmospheric Aerosols. (December 2007)

Jun Zhao, B.E., South China University of Technology

Chair of Advisory Committee: Dr. Renyi Zhang

Aerosol particles have profound impacts on human health, atmospheric radiation, and cloud microphysics and these impacts are strongly dependent on particle sizes. However, formation and growth of atmospheric particles are currently not well understood. In this work, laboratory and theoretical studies have been performed to investigate the formation and growth of atmospheric particles. The first two parts of the dissertation are a laboratory investigation of new particle formation and growth, and a theoretical study of atmospheric molecular complexes and clusters. The nucleation rate was considerably enhanced in the presence of cis-pinonic acid and ammonia. The composition of the critical cluster was estimated from the dependence of the nucleation rate on the precursor concentration and the time evolution of the clusters was then simulated using molecular dynamic simulations. Results from quantum chemical calculations and quantum theory of atoms in molecules (QTAIM) reveal that formation of strong hydrogen bonding between an organic acid and sulfuric acid is likely responsible for a reduction of the nucleation barrier by modifying the hydrophobic properties of the organic acid and allowing further addition of hydrophilic species (e.g., H_2SO_4, H_2O, and possibly NH_3) to the hydrophilic side of the clusters. This promotes

growth of the nascent cluster to overcome the nucleation barrier and thus enhances the nucleation in the atmosphere.

The last part of this dissertation is the laboratory investigation of heterogeneous interactions of atmospheric carbonyls with sulfuric acid. Direct measurement has been performed to investigate the heterogeneous uptake of atmospheric carbonyls on sulfuric acid. Important parameters have been obtained from the time-dependent or time-independent uptake profiles. The results indicated that the acid-catalyzed reactions of larger aldehydes (e.g. octanal and 2, 4-hexadienal) in sulfuric acid solution were attributed to aldol condensation in high acidity. However such reactions do not contribute much to secondary organic aerosol (SOA) formation due to the low acidity under tropospheric conditions. On the other hand, heterogeneous reactions of light dicarbonyl such as methylglyoxal likely contribute to SOA formation in slightly acidic media. The reactions of methylglyoxal in the atmospheric aerosol-phase involve hydration and subsequent polymerization, which are dependent on the hygroscopicity, rather than the acidity of the aerosols.

DEDICATION

This dissertation is dedicated to my family: My wife, Hongtao, and my daughter, Lucy.

ACKNOWLEDGEMENTS

I would like to thank my advisor, Dr. Renyi Zhang, for his support and guidance throughout my Ph.D. program. I wish to thank my committee members, Dr. Donald R. Collins, Dr. Robert A. Duce and Dr. Simon W. North for their helpful comments and discussions. I would like to thank Dr. Robert L. McGraw, a committee member of special appointment, for helping me with an understanding of nucleation in this important field of atmospheric chemistry.

I also want to thank my former colleagues, Drs. Wenfang Lei, Dan Zhang, Inseon Suh, Edward Fortner, Jiwen Fan and Mr. Nick Levitt for their generous help and teamwork. Thanks also to my current group members, Dr. Jun Zheng, Mr. Guohui Li and Mr. Huaxin Xue. Special thanks to Dr. Alexei Khalizov, who helped me set up the mass spectrometer and gave me much help with my dissertation research. I would also like to thank our departmental office staff for helping me with both academic and non-academic stuff and making my study a happy journey at Texas A&M.

I am thankful to my wife, Hongtao, and my daughter, Lucy, for their support and patience during my study.

The author also acknowledges financial support from the Robert A. Welch Foundation (A-1417), and the Texas Air Research Center (TARC) and additional support from the Texas A&M University Supercomputing Facilities and the use of the Laboratory for Molecular Simulations at Texas A&M University.

TABLE OF CONTENTS

Page

ABSTRACT iii

DEDICATION v

ACKNOWLEDGEMENTS vi

TABLE OF CONTENTS vii

LIST OF TABLES ix

LIST OF FIGURES x

CHAPTER

I INTRODUCTION 1

II LABORATORY INVESTIGATION OF NEW PARTICLE FORMATION AND GROWTH 10

2.1 Introduction 10
2.2 Experimental methodology 13
2.2.1 New particle generation 13
2.2.2 Ion-drift Chemical Ionization Mass Spectrometry (ID–CIMS) 15
2.2.3 UCPC/DMA system 20
2.3 Results and discussion 22
2.3.1 Nucleation rate determination 22
2.3.2 Losses of nucleating precursors in the nucleation system 27
2.3.3 Binary nucleation of sulfuric acid and water 29
2.3.4 Vapor pressure measurement of cis-pinonoic acid 33
2.3.5 Ternary nucleation of cis-pinonic acid–sulfuric acid–water 35
2.3.6 Nucleation involving ammonia 39
2.4 Summary 42

III THEORETICAL INVESTIGATION OF NEW PARTICLE FORMATION 44

3.1 Introduction 44
3.2 Theoretical methods 49

CHAPTER Page

3.3 Results and discussion 50
3.3.1 Geometrical analysis 50
3.3.2 Thermodynamic analysis 62
3.3.3 Topological analysis 68
3.3.4 Molecular dynamic simulations of clusters 76
3.4 Summary 82

IV LABORATORY INVESTIGATION OF HETEROGENEOUS INTERACTIONS OF ATMOSPHERIC CARBONYLS AND SULFURIC ACID: IMPLICATIONS FOR SECONDARY ORGANIC AEROSOL FORMATION 83

4.1 Introduction 83
4.2 Experimental methodology 87
4.3 Results and discussion 96
4.3.1 Heterogeneous chemistry of octanal and 2,4-hexadienal with sulfuric acid 96
4.3.2 Heterogeneous chemistry of methylglyoxal with sulfuric acid 104
4.4 Summary 112

V SUMMARY 114

REFERENCES 116

VITA 139

LIST OF TABLES

TABLE Page

3.1 Bond Length and Bond Angle of the Hydrogen Bonds in the Sulfuric Acid/Organic Acid/Ammonia/Water Complexes.. 56

3.2 Contact Distance d(O---O) of the Hydrogen Bond (-O-H•••O=) in the Organic Acid–Sulfuric Acid Complexes and Their Homomolecular Dimers. 59

3.3 The Calculated Stretching Frequencies of Dimers of Sulfuric Acid and Organic Acid and Their Monomers. 61

3.4 The Calculated Stretching Frequencies of Sulfuric Acid/Organic Acid/Water Complexes... 61

3.5 The Calculated Stretching Frequencies of Organic Acid/Ammonia Complexes.…. 61

3.6 Thermochemical Parameters for the Complex Formation at G2(MP2, SVP) Level. 65

3.7 Thermochemical Parameters for the Complex Formation at CCSD(T) + CF Level.… 65

3.8 Thermochemical Parameters for the Complex Formation at B3LYP and PW91PW91 Level.… 65

3.9 Comparison of the Equilibrium Bond Length and the Bond Path Length of the Complexes. … 73

3.10 Topological Parameters (Charge Densities, Laplacian, Kinetic Energy Densities, Potential Energy Densities and Total Energy Densities) at BCPs of the Hydrogen Bonds of the Complexes.… 75

4.1 Summary of H* Measurements for Octanal in H_2SO_4.… 99

4.2 Summary of γ Values of 2,4-hexadienal in H_2SO_4.… 102

4.3 Summary of H* for Methylglyoxal in H_2SO_4. 109

LIST OF FIGURES

FIGURE Page

2.1 Schematic presentation of experimental set-up for new particle formation… 14

2.2 Spectral scan for the reagent ions under typical experimental conditions… 19

2.3 The axial temperature distribution in the nucleation system …..... 24

2.4 The axial distribution of RH (dashed line) and equilibrium composition of sulfuric acid (solid line) along the condenser. 24

2.5 The axial distribution of saturation ratio with (square) and without (triangle) diffusion loss correction … 25

2.6 The axial distribution of particle number density in the nucleation system. 26

2.7 The axial concentration distribution of sulfuric acid (diamond), cis-pinonic acid (circle) and ammonia (square), assuming a concentration of 1 x 10^9 molecule cm^{-3} at the beginning of the condenser…..... 29

2.8 The binary H_2SO_4–H_2O nucleation rate J as a function of H_2SO_4 concentration at various RHs in logarithmic scales. … 31

2.9 The same figure as Figure 2.8, the only difference is that both axes are in linear scales.… 32

2.10 Plot of flow f as a function of Ps at a bath temperature of 303 K.… 36

2.11 Plot of the vapor pressure of cis-pinonic acid in logarithmic scale versus the inverse of temperature (1/T).…..... 36

2.12 The ternary (H_2SO_4–cis-pinonic acid–H_2O) nucleation rate J as a function of H_2SO_4 concentration at various RHs..… 38

2.13 The ternary (H_2SO_4–cis-pinonic acid–H_2O) nucleation rate J as a function of cis-pinonic acid concentration at RH = 13.2%..… 40

2.14 The size distribution of the ternary nucleation of H_2SO_4–cis-pinonic acid–H_2O in the presence of cis-pinonic acid....… 40

FIGURE Page

2.15 The nucleation rate (J) of the ternary H_2SO_4–H_2O–NH_3 as a function of sulfuric acid concentration at (a) RH = 13.2% and (b)RH = 20.2%..... 42

3.1 The optimized geometries of hydrogen bonded complexes at B3LYP/6-31G(d, p) level..... 52

3.2 The calculated vibrational frequencies and the corresponding absorption intensities of cis-pinonic acid–sulfuric acid complex and its onomers..... 63

3.3 Molecular graphs of the organic acid–sulfuric acid complexes showing the BCPs, ring critical points, bond path and ring path..... 70

3.4 Molecular graphs of the sulfuric acid–water, sulfuric acid–ammonia and benzoic acid–ammonia complexes showing the BCPs, ring critical points, bond path and ring path..... 71

3.5 Plot of r1/r2 as a function of equilibrium bond length..... 73

3.6 The shape and size of a cluster composed of 1 cis-pinonic acid, 4 sulfuric acid and 10 water..... 80

3.7 Fluctuation of the total energy, kinetic energy and potential energy during a typical simulation run..... 81

3.8 Fluctuation of the cell parameters (a, b, c) during the same simulation run..... 81

4.1 Schematic representation of the flow reactor coupled to the ion drift – chemical ionization mass spectrometry (ID–CIMS)..... 88

4.2 Spectral scans for the reagent ions (a, *m/z* = 10~100) and protonated methylgloxal (b, *m/z* = 60~200) for a typical experimental condition (before an uptake experiment)..... 91

4.3 Schematic representation of kinetic processes of heterogeneous uptake of trace species into liquid droplets or aerosol particles 92

4.4 A simple resistance model of the kinetic processes shown in Figure 4.3..... 92

4.5 Temporal profiles of octanal when repeatedly exposed and not exposed to a 20 cm length of sulfuric acid..... 97

FIGURE Page

4.6 Plot of 1/γ as a function of $t^{1/2}$ for (a) data displayed in Figure 4.5, (b) 1/γ as an acid content of 65.1 wt % at T = 273 K and P = 1.1 Torr. 98

4.7 Mechanistic presentation of aldol condensation of octanal and 2, 4-hexadienal in sulfuric acid solution. 100

4.8 Temporal profiles of 2, 4-hexadienal when exposed and not exposed to a 20 cm length of sulfuric acid. 101

4.9 Intensity of 2,4-hexadienal as a function of injector distance.… 103

4.10 Temporal profiles (I, intensity) of methylgloxal when exposed to a 20 cm length of a vessel containing (a) a 80 wt % H_2SO_4 at T = 273 K, (b) a 58 wt % H_2SO_4 at T = 253 K (c) 68 wt % H_2SO_4 at *T* = 263 K …. 106

4.11 Plots of 1/γ vs $t^{½}$, corresponding to Figure 4.10.…. 108

4.12 Possible aqueous reaction mechanism of methylglyoxal in H_2SO_4… 110

CHAPTER I

INTRODUCTION

Aerosol particles are defined as liquids or solids suspended in air and they are ubiquitous in the Earth's atmosphere. Atmospheric particles are usually classified into four size ranges: nucleation mode (1–20 nm), Aitken mode (20–90 nm), accumulation mode (90–1000 nm) and coarse mode (>1 μm) [*Kulmala et al.,* 2004]. According to the source origin, atmospheric particles can be divided into two categories: primary particles and secondary particles [*Seinfeld and Pandis,* 1998]. Primary particles are produced from direct sources, e.g. soot particles from combustion, sea salt from ocean spray, mineral dust dispersed from desert and pollen and spores from biological sources, and secondary particles are generated by gas-particle conversion, e.g. sulfate and nitrate from oxidation of sulfur dioxide and nitrogen oxides, respectively, and organic aerosol from photo-oxidation of volatile organic compounds (VOCs) in the atmosphere. The number concentration of particles covers a considerably wide range from less than 10 particles cm^{-3} in the stratosphere [*Curtius et al.,* 2005] to greater than 10^5 particles cm^{-3} in the polluted urban area [*Jaenicke and Hanusch,* 1993]. The sub-micro fine particles comprise the majority of the total number concentration while the fewer coarse particles (D_p > 1 μm) make up of a large fraction of the total aerosol mass in the atmosphere [*Kulmala et al.,* 2004].

Aerosol particles have profound impacts on human health, atmospheric radiation, and cloud microphysics and these impacts are strongly dependent on the

---

This dissertation follows the style and format of the *Journal of Geophysical Research.*

particle sizes [*Seinfeld and Pandis,* 1998; *Finlayson-Pitts and Pitts,* 2000]. Human health is considered as one of the most important factors in regulating the national ambient air quality standard [*NCEA,* 1996]. Upon inhaling into the respiratory system, large aerosol particles remain trapped in the nasopharyngeal cavity, while small particles, especially ultra-fine particles, can penetrate the alveolar section of the lungs and therefore be more harmful to human health. In addition, recent epidemiological research has shown increases in adverse cardiovascular and respiratory effects related to ultra-fine particles, which contain higher concentration of toxic air pollutants than larger particles [*Seaton et al.,* 1995; *Schulz et al.,* 2005]. Atmospheric aerosol particles influence the Earth's radiation balance directly by scattering and absorbing solar radiation, and indirectly by acting as cloud condensation nuclei (CCN) [*Charlson et al.,* 1987; *Alley,* 2001; *IPCC,* 2007]. Aerosol particles in the size range of 0.1–1.0 μm are major contributors to visibility degradation in the urban area because of their highly efficient light scattering properties [*Horvath,* 1995; *Seinfeld and Pandis,* 1998; *Cheng and Tsai,* 2000]. Aerosol formation and growth processes (e.g. nucleation, condensation, coagulation) also influence cloud formation, thereby modifying cloud microphysics [*Charlson et al.,* 2001; *Kanakidou el al.,* 2005]. Globally atmospheric aerosols are believed to be an important contributor to climate change by affecting the atmospheric radiation budget and modifying cloud properties. Many efforts have been exerted to evaluate the radiative forcing of the total aerosol effects including direct and indirect effects. *IPCC* [2007] recently reported an average radiative forcing of –0.5 and –0.7 W m^{-2} for the direct effect and indirect effect (in term of cloud albedo), respectively.

However, large uncertainties still exist in current estimates of aerosol forcing due to incomplete knowledge regarding the formation, growth, distribution and the physical and chemical properties of aerosols as well as aerosol-cloud interactions.

Secondary particles experience several processes during their lifetime in the atmosphere including nucleation, growth by condensation of condensable species and coagulation with other particles, aging by heterogeneous aerosol phase reactions or surface reactions, removal by dry deposition at the Earth's surface or wet deposition via incorporation into the cloud droplet during the formation of precipitation. Residence times of the tropospheric particles vary from a few days to a few weeks [*Seinfeld and Pandis,* 1998]. Researches on these processes constitute several of the current frontiers in the aerosol research community. Among those processes, new particle formation or nucleation is an important and also the least understood one due to its inherent complexity. The thermodynamics and kinetics of nucleation have been investigated extensively since the 1930s when classical nucleation theory (CNT) was created [*Volkmer and Weber,* 1926; *Farkas,* 1927; *Becker and Doring,* 1935]. Some important modifications to the classical nucleation theory have been made over 80 years [*Lothe and Pound,* 1962; *Reiss,* 1977; *Drossinos and Kevrekidis,* 2003]. CNT is based on the capillarity approximation where a particle in a nascent phase is assumed to have a sharp boundary and the same uniform properties (e.g. density and surface tension) as the bulk phase [*Lothe and Pound,* 1969; *Bostanov et al.,* 2000]. In the case of homogenous nucleation, cluster formation and initial growth play important roles in the nucleation processes. The initial growth of clusters is due exclusively to fluctuations as addition of

a molecule to the clusters is thermodynamically unfavorable. Once the clusters grow larger enough to reach a critical size, further addition of monomer to the clusters will be thermodynamically favorable and thus the cluster will grow spontaneously. In CNT, the nucleation rate J (in particles cm^{-3} sec^{-1}) in a steady state is proportional to the exponential of the height of the nucleation barrier ($-\Delta G^*$) in the form of

$$J = J_0 \exp(-\Delta G^* / kT) \tag{1.1}$$

where J_0 is the pre-exponential factor and k is Boltzmann's constant and T is the temperature. *Reiss* [1950] used kinetic and thermodynamic treatments to show that nucleation goes through the saddle point of the free energy surface, following the steepest descent of the surface in size space. However, the capillarity approximation becomes questionable since the critical cluster is very tiny and only consists of a few tens of molecules, as will be discussed next.

The application of CNT to binary nucleation of sulfuric acid and water dates back to 46 years ago. *Doyle* [1961] used *Reiss's* theory [1950] to estimate the nucleation rate in the sulfuric acid–water system including the dependence of the surface tension on sulfuric acid composition. Doyle's theory assumed that the cluster composition is uniform and no surface enrichment effects are allowed for the given total numbers of molecules in the cluster, which has been shown to lead to thermodynamic inconsistencies [*Renninger et al.,* 1981; *Wilemski,* 1984]. The thermodynamically consistent theory by *Wilemski* [1984, 1987] took into account the difference between the interior and surface compositions. Doyle's theory and Wilemski's theory predict different sizes and compositions of the nuclei and different nucleation rates by several

orders of magnitude under atmospheric conditions [*Kulmala et al.,* 1998]. By accounting for the hydrate effects, the binary nucleation rate decreases due to the stabilizing effects of the hydrates on the sulfuric acid vapor [*Shugard et al.,* 1974; *Heist and Reiss,* 1974]. The predictions of sulfuric acid–water nucleation rates using the thermodynamically consistent theory incorporating another hydration correction by *Noppel* [1998] are in accordance with the experimental results of *Wyslouzil et al.* [1991] and *Boulaud et al.* [1977] obtained at 293 and 298 K. However, the predicted dependence of nucleation rates on temperature is stronger than that of the experiments at a given concentration of sulfuric acid, and the nucleation rate is ~3–6 orders of magnitude lower than that of the hydration correction by *Jaecker-Voirol, Mirabel, and Reiss* [1987]. *Kulmala et al.* [1998] presented a parameterization of homogeneous binary nucleation of sulfuric acid and water, in reasonable agreement with *Wilemski's* thermodynamically consistent theory incorporating *Noppel's* hydration correction. A recent version of the hydration model with many improvements has been presented by *Noppel et al.* [2002]. The improvements increase the predicted nucleation rates compared to the earlier version of the model and the predicted nucleation rates are comparable to those of the available experimental data. The quasi-unary kinetic model by *Yu* [2005] reduces the binary homogeneous nucleation of H_2SO_4–H_2O to quasi-unary nucleation by assuming that the clusters are in equilibrium with H_2O and the predicted nucleation rates with this kinetic model are consistent with results from nucleation experiments [*Viisanen et al.,* 1997; *Ball et al.,* 1999]. The classical nucleation theory and its variants are still the dominant

models to predict nucleation rates in the atmosphere, although there exists high uncertainty within the classical theory framework.

Sulfuric acid has long been considered as a major atmospheric nucleating agent and most of the earlier studies have focused on nucleation of sulfuric acid, since sulfate aerosol represents an important component of nucleation mode aerosol. It has been suggested that new particle formation depends on the sulfuric acid concentration and the number of molecules in the critical nucleus can be derived from this dependence. Several laboratory experiments have been implemented to elucidate mechanisms of the H_2SO_4–H_2O nucleation involving high sulfuric acid concentration (in the order of 10^9–10^{10} molecules cm^{-3}) and near atmospheric sulfuric acid concentration (10^6–10^7 molecules cm^{-3}) conditions [*Wyslouzil et al.,* 1991; *Viisanen et al.,* 1997; *Ball et al.,* 1999; *Berndt et al.,* 2000, 2005]. However, there exist significant discrepancies among these measurements regarding the values of the power dependence of the nucleation rate on the sulfuric acid concentration and these values range broadly from 2 to 14. On the other hand, atmospheric observation shows that the dependence is much less, with a value of 1–2 [*McMurry et al.,* 2005; *Kulmala et al.,* 2006]. Regardless of these discrepancies, it is commonly believed that complex and pre-nucleation cluster formation is the starting point for binary H_2SO_4–H_2O nucleation. Pre-nucleation clusters containing up to 8 sulfuric acid molecules in the H_2SO_4–H_2O system have been detected in recent years [*Eisele and Hanson,* 2000; *Hanson and Eisele,* 2002; *Couling et al.,* 2003], although these measurements need to be further validated.

Binary H_2SO_4–H_2O nucleation, however, is not sufficient to explain the observed atmospheric nucleation rates without contribution from additional species according to the revised nucleation theory and laboratory data [*Boy et al.,* 2003]. Ternary nucleation involving the ubiquitous species NH_3 has been suggested as an explanation for the observed nucleation rates in the atmosphere [*Weber et al.,* 1999], but the concentration of atmospheric sulfuric acid (typically up to 10^7 molecules cm^{-3}) is insufficient to account for the growth of these new particles into detectable sizes (~3 nm). Other possible routes for the atmospheric new particle formation include ion-induced nucleation [*Yu and Turco,* 2001], nucleation involving iodine species in coastal areas [*O'Dowd et al.,* 2002], and nucleation involving organics [*Zhang et al.,* 2004]. Organic compounds may play important roles in new particle formation due to their abundance in the atmosphere. Recent field measurements have shown that organic compounds are important constituents of the atmospheric aerosols [*Kulmala et al.,* 2004; *Kanakidou et al.,* 2005]. *Zhang et al.* [2004] showed that new particle formation in the H_2SO_4–H_2O system is considerably enhanced in the presences of sub ppb level of aromatic acids (e.g. benzoic acid, m-toluic acid, p-toluic acid), which are produced from photochemical oxidation of aromatic hydrocarbons emitted from automobiles in the urban atmosphere. Quantum chemical calculations [*Zhang et al.,* 2004] show that formation of an unusually stable aromatic acid–sulfuric acid complex likely reduces the nucleation barrier and hence is responsible for the observed rate enhancement.

While aromatic organic acids have been shown to considerably enhance nucleation in the urban area [*Zhang et al.,* 2004], the roles that the biogenic organic

acids play in nucleation remain unknown in the forested area. Biogenic volatile organic compounds (VOCs) are emitted into the atmosphere at a rate of about 1.2 x 10^{14} gram C yr^{-1} on a globe scale [*Guenther et al.,* 1995; *Seinfeld and Pandis*, 1998], of which ~ 11% is composed of monoterpenes, with α- and β-pinene being the most abundant monoterpenes. The pinenes (α- and β-pinene) are removed from the atmosphere primarily by reactions with OH radicals, NO_3 radicals and O_3 [*Atkinson,* 1990]. Due to their high reactivity toward these oxidants, atmospheric oxidation of the pinenes contributes significantly to ozone and secondary organic aerosol (SOA) formation in the troposphere. Oxidation of pinenes by atmospheric oxidants results in the production of multiple functional organic compounds (e.g. aldehydes, ketones and carboxylic acids) with sufficiently low vapor pressure, which are important precursors for secondary organic aerosol or new particle formation. The low volatility compounds are either partitioned into the preexisting particles or involved in new particle formation [*Zhang et al.,* 2004]. However, the detailed roles of organic compounds in new particle formation still remain largely unknown. Since the organics are important components in the atmosphere, their involvement in atmospheric nucleation needs to be evaluated.

Newly-formed particles are expected to grow to larger sizes via both physical and chemical processes in the atmosphere. Physical processes include condensation of organic/inorganic species and coagulation between particles. Low volatility compounds are condensed onto the particles and hence contribute to the aerosol growth. Small particles, however, undergo relatively rapid Brownian motion, leading to sufficient particle-particle collision to cause coagulation. Chemical processes however are more

complicated. They involve surface reactions and heterogeneous particle-phase reactions. Heterogeneous reactions involving atmospheric organic compounds and their roles in secondary organic aerosol formation have not been studied until recently. Recent environmental chamber studies [*Jang et al.,* 2002, 2004; *Kalberer et al.,* 2004] have suggested that acid-catalyzed particle-phase reactions of carbonyls contribute to secondary organic aerosol (SOA) formation, contrary to conventional view, since carbonyls have not been considered to be insignificant contributors to particle growth due to their generally high volatility and limited ability to partition into aerosols. The heterogeneous reactions include hydration, polymerization, hemiacetal/acetal formation, aldol condensation and cationic rearrangement. Reactions of carbonyls in the aerosol-phase have been suggested to result in the formation of low-vapor pressure products or polymers [*Jang et al.,* 2002, 2004; *Kalberer et al.,* 2004], which considerably increases the organic mass. However, for a specific carbonyl or carbonyl category, which reactions will play important roles and the detailed mechanisms for the acid-catalyzed reactions are still unknown. In addition, how acidity affects these reactions in SOA formation remains unresolved.

CHAPTER II

LABORATORY INVESTIGATION OF NEW PARTICLE FORMATION AND GROWTH

2.1 Introduction

As mentioned in Chapter I, sulfuric acid has long been believed as an atmospherically important nucleating species and previous experimental studies focused on the binary H_2SO_4–H_2O nucleation. *Reiss et al.* [1976] presented the first experimental study of H_2SO_4–H_2O nucleation. *Wyslouzil et al.* [1991] performed the first systematic investigation of this binary system and the authors found nucleation rate extremely sensitive to parameters such as relative acidity, humidity and temperature. A critical nucleus was predicted to have 14 sulfuric acid molecules, assuming a perfect agreement on the nucleation rate between classic nucleation theory and the experiment. *Viisanen et al.* [1997] presented measurements of binary nucleation with H_2SO_4 concentration ranging from (1–3) x 10^{10} molecules cm^{-3} at two relative humidities (*RH* = 38.2 and 52.3 %). The measured nucleation rates vary between 2 and 3000 particles cm^{-3} sec^{-1}, in reasonable agreement with prediction of the revised classical nucleation theory incorporating the hydration effect of *Jaecker-Voirol, Mirabel, and Reiss* [1987]. *Ball et al.* [1999] investigated the particle nucleation with on-line down-stream detection of sulfuric acid using chemical ionization mass spectrometry (CIMS). The dependences of the particle formation rate on sulfuric acid and water were found to be eighth and fifth power, respectively. *Berndt et al.* [2000] presented experimental results in the binary nucleation, and the dependence of particle formation rate on the sulfuric acid

concentration was determined to be ~ 2–3, dramatically different from the previous studies. The sulfuric acid vapor was generated from bulk liquid sulfuric acid in the above-mentioned experiments, whose concentration is usually in the order of 10^{10} molecules cm^{-3}, substantially higher than the sulfuric acid concentration in the atmosphere. In a recent study, *Berndt et al.* [2005] used an in-situ method to generate sulfuric acid from SO_2 to investigate formation of sulfate particles under near-atmospheric conditions with sulfuric acid concentration ranging from 6 x 10^6 to 1 x 10^8 molecules cm^{-3}. The power dependence of the nucleation rate on the sulfuric acid concentration was determined to be ~ 3–5. A nucleation rate of 0.3 – 0.4 particles cm^{-3} sec^{-1} was predicted at a sulfuric acid concentration of 10^7 molecules cm^{-3}, in agreement with observed nucleation rates in the atmosphere. These findings provide valuable insights into the new particle formation mechanisms for H_2SO_4–H_2O nucleation. However, significant discrepancies still exist regarding the measured nucleation rates and the dependence of the nucleation rate on sulfuric acid concentration.

The involvement of other species (e.g. organics and ammonia) in H_2SO_4–H_2O nucleation has been an active research topic in recent years. *Zhang et al.* [2004] recently showed that new particle formation of the H_2SO_4–H_2O system is considerably enhanced in the presence of sub ppb level of aromatic acids (e.g. benzoic acid, m-toluic acid, p-toluic acid). In addition, the power dependence of the nucleation rate on sulfuric acid concentration was inferred to be ~ 8 at sulfuric acid concentrations of (4–11) x 10^9 molecules cm^{-3}. In this study, we choose cis-pinonic acid as our model biogenic organic acid to investigate ternary nucleation of sulfuric acid, water and organic acid because

cis-pinonic acid was found to be one of the most abundant low volatility products from the photooxidation of pinenes in the atmosphere [*Kavouras et al.,* 1998]. Mechanisms leading to the formation of cis-pinonic acid have been proposed to involve the reaction of the Cregiee intermediate with water, followed by rearrangement and elimination of water [*Glasius et al.,* 2000]. Alternatively, cis-pinonic acid can be formed from isomerization of the Cregiee intermediate (so called ester channel) [*Winterhalter et al.,* 2003]. In this study, we reinvestigated new particle formation from binary and ternary nucleation with better-controlled experiments. The sulfuric acid concentration was monitored on-line using ion drift chemical ionization mass spectrometry (ID–CIMS), and particle size distribution and number concentration were measured simultaneously using a nano-DMA/UCPC system. We characterized the nucleation zone and estimated the losses of the nucleation precursors in the flow tube system. We determined the dependences of the nucleation rate on both sulfuric acid and organic acid concentrations upon addition of cis-pinonic acid.

Ammonia is a ubiquitous species in the atmosphere; however, nucleation mechanisms involving ammonia remain largely unknown. Previous experimental studies showed that tens of ppt of ammonia is able to promote large enhancements of binary H_2SO_4–H_2O nucleation [*Ball et al.,* 1999; *Hanson and Eisele,* 2002]. *Yu* [2006] employed the classical ternary homogeneous nucleation (THN) theory constrained by the laboratory experiments of *Ball et al.* [1999] and *Kim et al.* [1998] and predicted up to 30 orders of magnitude enhancement of the nucleation rates in the presence of ppt level of NH_3. Other model studies employing the classical nucleation theory [*Coffman and*

Hegg, 1995; *Korhonen et al.,* 1999; *Napari, et al.,* 2002a, b] also predicted several orders of magnitude enhancements of binary H_2SO_4–H_2O nucleation in the presence of 1 ppt ammonia. Quantum chemical calculations, as will be discussed in Chapter III, however, showed great discrepancies regarding the role of ammonia in new particle formation [*Ianni and Bandy,* 1999; *Larson et al.,* 1999; *Kurten et al.,* 2006, 2007a, b]. In this study, we investigated the enhancement of new particle formation in the presence of ammonia. We compared the effect of organic acid with that of ammonia to new particle formation.

2.2 Experimental Methodology

2.2.1 New particle generation

The experiments were carried out in a nucleation system coupled to multiple analytical instruments as shown in Figure 2.1. The nucleation system consists of (1) A mixing unit with a length of 30 cm and an inner diameter of 2 cm, and (2) A condenser unit with a length of 60 cm and the same inner diameter as that of the mixing unit. Both the mixing unit and the condenser unit were constructed from precision-bore Pyrex tubing. The outer wall of the mixing unit was wrapped with a heating tape (Samox insulated heating tape) and a thermocouple was deployed into the unit through a ¼ inch diameter port. The distance between the tip of the thermocouple and the inner wall surface of the unit is ~ 0.5 cm. A temperature controlling system (Honeywell temperature controller) was used to control the gas temperature inside the mixing unit by controlling the output power to the heating tape and the temperature of the mixing vapor was regulated at 353 ± 0.5 K. The gas temperature inside the condenser was controlled

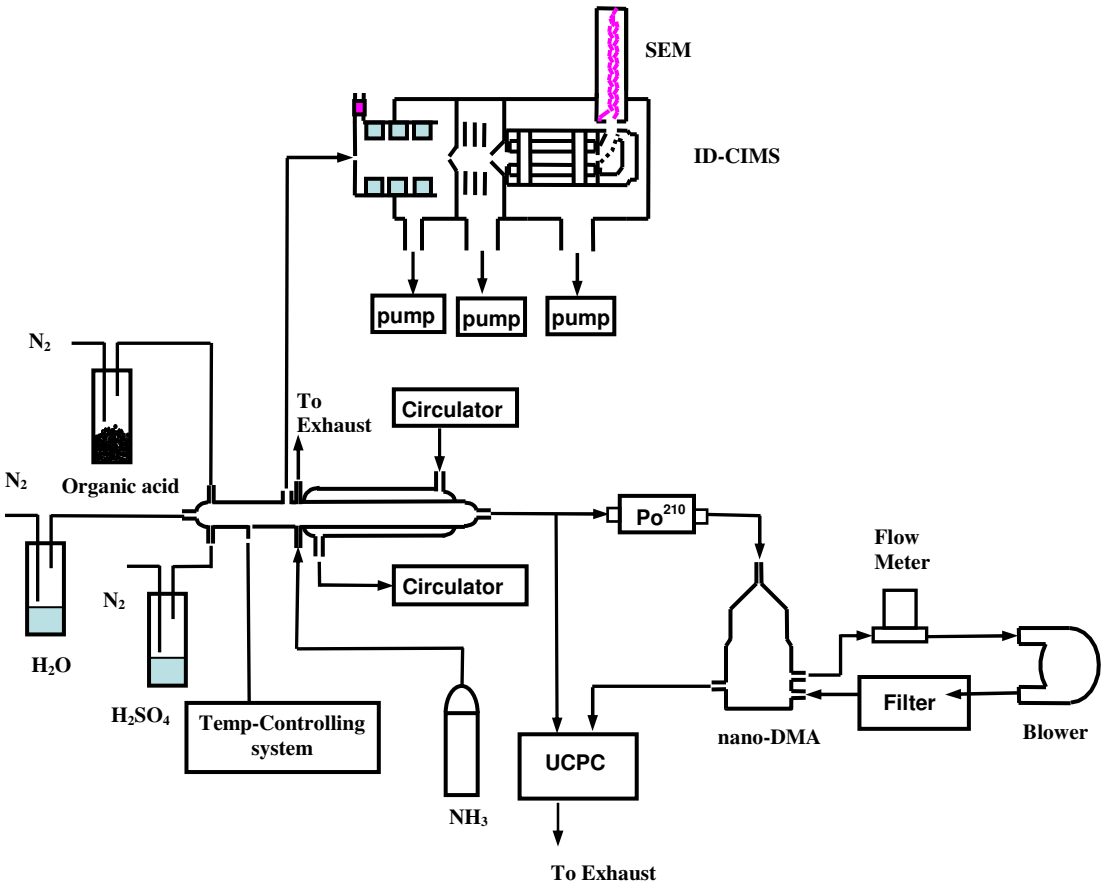

Figure 2.1. Schematic presentation of experimental set-up for new particle formation.

by circulating cold methanol through the middle layer of the circulator and was kept at 280 ± 0.5 K. The axial temperature distribution at the center of the condenser was measured by a calibrated thermocouple, as will be discussed in Section 2.3.1. Gaseous sulfuric acid was introduced by passing a small flow of nitrogen through a saturated bubbler containing liquid sulfuric acid (98%, Aldrich) and the inlet of the bubbler was heated to ~393 K to reduce the wall loss of sulfuric acid. The bubbler was immersed into a water bath container which was regulated at 311 K. Water vapor was admitted by

bubbling a flow of nitrogen through a Pyrex bubbler containing deionized water (*resistivity* = 18 MΩ·cm). The bubbler was immersed into a water bath container, which was kept at 312 K. The water droplets from the bubbler were vaporized through a ~ 50 cm long and an inner diameter of 3/8 inch inlet wrapped with a heating tape kept at 393K before water vapor was introduced into the mixing unit. The humidity in the condenser unit was calibrated using a hygrometer by measuring the dew point of the water vapor. The measured relative humidity was in good agreement with that calculated value from the volumetric flow assuming 100% saturation ratio of water in the bubbler. The gaseous sulfuric acid and water were mixed in the mixing unit and then entered the condenser where binary nucleation of sulfuric acid and water occurred. For ternary or multi-component nucleation, organic acid was introduced by passing a flow of nitrogen through the organic acid (solid powder) bubbler and the inlet of the bubbler was kept at a temperature of 413 K to reduce loss of organic acid to the wall. In some experiments, ammonia was admitted by diluting a small fraction of ammonia from the cylinder into the desired concentration and the resultant flow was directed into a sidearm right before the entrance of the condenser. In order to prevent loss of heat into the ambient air and disturbance from the ambient air circulation, the whole mixing system was sealed into an aluminum box to ensure good isolation.

2.2.2 Ion-drift Chemical Ionization Mass Spectrometry (ID–CIMS)

We recently developed an ion-drift chemical ionization mass spectrometer (ID–CIMS), capable of quantifying a gaseous species (e.g. volatile organic compounds, sulfuric acid, organic acid, nitric acid, N_2O_5) without the necessity of calibration. A

detailed description of the ID–CIMS technique can be found in a recent publication [*Fortner et al.,* 2004] and here the instrument relevant to this work is described. The ID–CIMS system consists of an ion source to produce positive or negative reagent ions, a drift tube where the ion-molecule reaction occurs, and a quadrupole mass spectrometer where the ions are analyzed. The drift tube was constructed of a 10-cm-length Pyrex tube, containing a set of 15 stainless steel rings connected in series with 1MΩ resistors between rings. The rings had an inner diameter of 1.4 cm through which the flow passed. The ion-molecule reactions between the reagent ions and the neutral compound to be detected and quantified occur in this region. The pressure in the drift tube was regulated at ~ 3 torr. A voltage was applied to the rings to accelerate the ions and minimize formation of ion clusters, which might complicate the ion-molecule reactions. At the downstream end of the drift tube, the majority of the flow was diverted into a vacuum pump while a small portion of the flow passed through an aperture (0.2 mm) into the intermediate chamber, where three lenses with various voltages were applied to guide the ions into the quadrupole analyzer (Balzers QMS 420) chamber. The aperture was biased with a voltage for ion-tuning purposes, and the polarity and the voltage was dependent on the polarity of the reagent ions produced. The sampled ions were focused with internal ion optics. To reach the quadrupole rod system, the ions must possess high enough kinetic energy and the ion lenses in such a specific system need to be tuned to ensure the ions are properly transported into the quadrupole. The ions were then analyzed with a quadrupole mass filter, and detected by a deflexed (90˚) secondary electron multiplier (SEM). The multiplier was connected with a preamplifier, which

converted the raw signal into TTL pulses allowing them to be processed by the National Instrument data acquisition card and communicated with a personal computer.

A constant flow (~1200 sccm) of gas mixture of sulfuric acid, water and/or organic acid was diverged at a 90° angle and drawn through a pinhole of approximately 350 μm diameter into the drift tube region (not shown in Figure 2.1). The distance between the divergent point of the flow and the pinhole was minimized to prevent stagnation in this region and to reduce the wall loss around the pinhole. Gaseous sulfuric acid was monitored in-situ and quantified upstream of the condenser with negative ion mode using either $NO_3^-(HNO_3)_n$ (n = 0, 1, 2) ions [*Eisele and Tanner,* 1993] or CO_x^- (x = 3, 4) as the reagent ion [*Schoon et al.,* 2002; *Salcedo et al.,* 2004].

$$H_2SO_4 + NO_3^-(HNO_3)_n \rightarrow HSO_4^-(HNO_3)_n + HNO_3 \quad (2.1)$$

$$\text{or} \quad H_2SO_4 + CO_x^- \rightarrow HSO_4^- + HCO_x \quad (2.2)$$

Typical relative intensity of the reagent ions is in the following order: $NO_3^-(HNO_3) > NO_3^-(HNO_3)_2 > NO_3^-$ and sulfuric acid were detected at m/z = 97, 160 and 223 Dalton. The ion-molecule rate constants between H_2SO_4 and $NO_3^-(HNO_3)_n$ were determined experimentally with a value of 2.32, 1.86, 1.72 x 10^{-9} cm^3 $molecule^{-1}$ sec^{-1} for n = 0, 1, 2, respectively [*Viggiano et al.,* 1997]. Alternatively, CO_x^- (x = 3, 4) can be used as the reagent ions to detect H_2SO_4, and the ion-molecule rate constants between H_2SO_4 and CO_x^- were estimated with average-dipole orientation (ADO) theory [*Su and Bowers,* 1973; *Su and Bowers,* 1975], which has been validated for the proton transfer reaction between VOCs and hydronium ions (H_3O^+) [*Zhao and Zhang,* 2004].

Gaseous organic acid was detected and quantified using either H_3O^+ (positive mode) via proton transfer reaction or $CO_2 \bullet O_2^-$ (negative mode) as reagent ions via switching reaction,

$$\text{Organic acid} + H_3O^+ \rightarrow \text{Organic acid-}H^+ + H_2O \quad (2.3)$$

or

$$\text{Organic acid} + CO_2 \bullet O_2^- \rightarrow \text{Organic acid-}O_2^- + CO_2 \quad (2.4)$$

For example, cis-pinonic acid was detected at m/z = 185 and 216 Dalton for H_3O^+ and $CO_2 \bullet O_2^-$ as the reagent ions, respectively. An ion-molecule rate constant of 3.64 and 2.06 cm^3 $molecule^{-1}$ sec^{-1} was determined using ADO theory for reactions with H_3O^+ and $CO_2 \bullet O_2^-$, respectively [*Su and Bowers,* 1973; *Su and Bowers,* 1975; *Zhao and Zhang,* 2004]. Figures 2.2a–b show the spectral scan for the reagent ions under typical experimental conditions, the highest peaks being $NO_3^-(HNO_3)$ and $CO_2 \bullet O_2^-$, respectively.

The unique feature of the ID–CIMS is its capability of detecting and quantifying a species using either negative or positive reagent ions. For the ion molecule reaction $X + R^{\pm} \rightarrow Y^{\pm} + Z$, the concentration of a neutral species X was determined by $[X]=S(Y^{\pm})/(S(R^{\pm}) \bullet k \bullet t)$, where $S(Y^{\pm})$ and $S(R^{\pm})$ is the intensity of product ion and reagent ion, respectively; k is the ion-molecule rate constant and t is the ion drift time, which is well defined in the drift region for both positive and negative ions and determined by the ion mobility of the reagent ions. A reduced ion mobility of 2.33 cm^2 sec^{-1} $volt^{-1}$ in N_2 at 300K for NO_3^- was taken from experimental measurement by *Viehland and Fahey* [1983]. We estimated the reduced ion mobilities of 1.9 and 1.4 for $NO_3^- \bullet HNO_3$ and $NO_3^- \bullet (HNO_3)_2$ in N_2 at 300K, respectively, based on a value of 2.2 cm^2

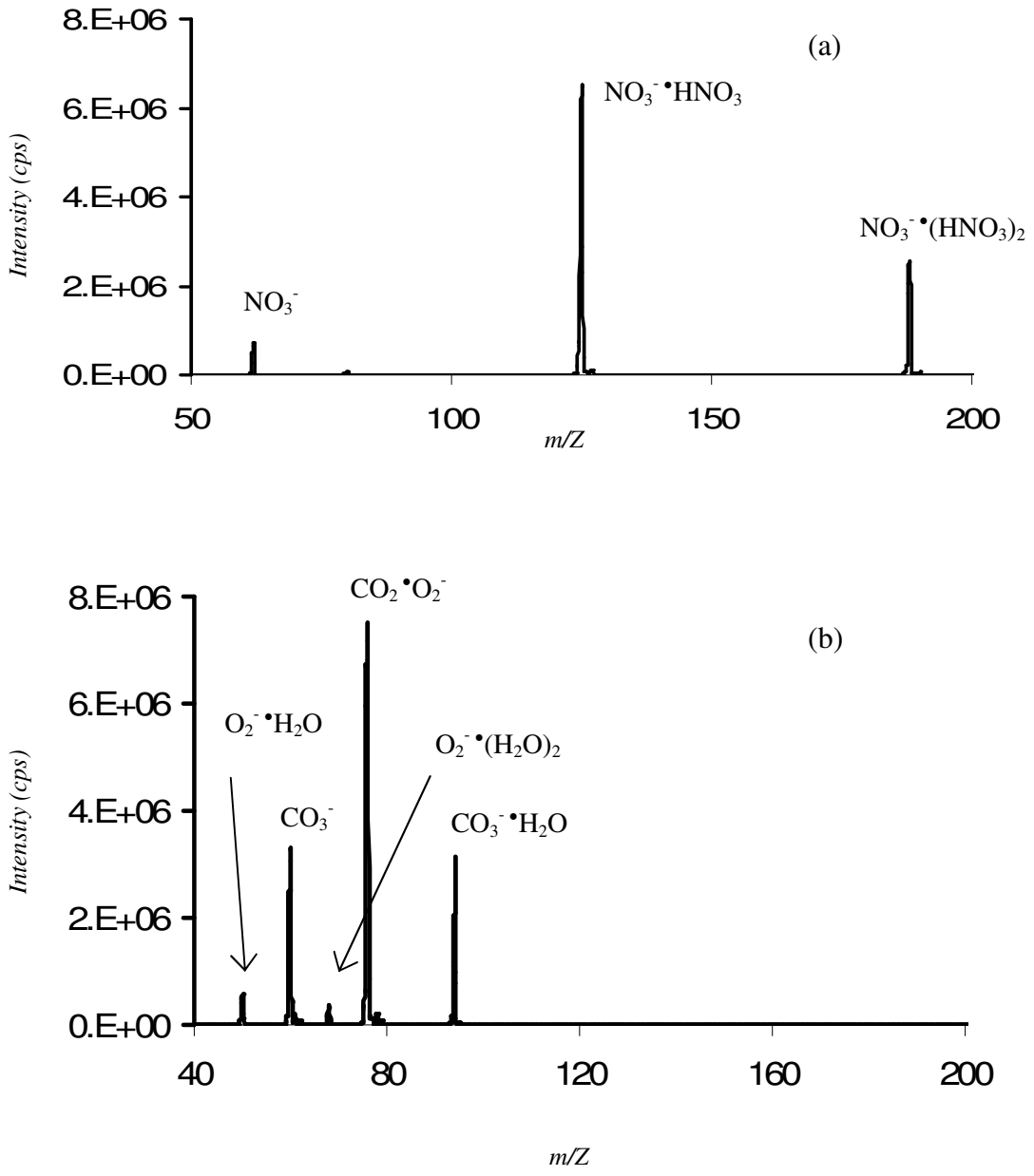

Figure 2.2. Spectral scan for the reagent ions under typical experimental conditions.

sec^{-1} $volt^{-1}$ for the reduced ion mobility of $NO_3^-•H_2O$ in N_2 at 300K reported by *Eisele et al.* [1981]. Since no reduced ion mobility of CO_3^- and $CO_2•O_2^-$ in N_2 was reported, we adopted a measured value of 2.5 and 2.4 for CO_3^- and $CO_2•O_2^-$ in O_2 at 300K, respectively [*Perkins et al.,* 1981]. The ion-drift time for positive and negative reagents is on the order of 10^{-5} and 10^{-2} seconds, respectively. The concentration profiles of sulfuric acid and organic acid along the condenser were then obtained by accounting for the diffusion loss on the wall, which will be discussed in section 2.3.1.

2.2.3 UCPC/DMA system

An ultra-fine condensation particle counter (UCPC, model 3025A, TSI) was employed to count the particle number density and it can be combined with a nano-differential mobility analyzer (nano-DMA, model 3085, TSI) [*Chen et al.,* 1998] to measure the particle size distributions. This UCPC can detect particle size down to 3.0 nm and the detection efficiency at this size is 50%. In this study, the UCPC was operated in a high-flow mode (1.5 L min^{-1}) to minimize the particle loss during transportation from the exit of the condenser to the detector. We kept the gas flow in the condenser at the same constant rate of 1.5 L min^{-1}. The size of the nano-DMA classified covers a range of particle mobility diameter from 2 to 150 nm. The nano-DMA has a center electrode with an outer radius of 0.937 cm and a grounded electrode with an inner radius of 1.905 cm. The characteristic length has been reduced to 4.987 cm (compared to a length of ~ 44 cm for model 3081 long DMA) to decrease the residence time of the particle in the classification zone and hence minimize the diffusion loss of the particles. The particles are classified according to their size-dependent electric mobilities. In

principle, the electrical mobility holds a unique relationship with particle size for particles with one elementary charge. *Knutson and Whitby* [1975] determined a relationship between the particle electrical mobility and the DMA parameters, and the applied voltage to the nano-DMA was correlated to the particle size. A size distribution was thus determined by scanning the voltage applied to the nano-DMA, which creates an electric field to separate particles according to their mobilities (hence sizes). Since we focused on the particle size less than 10 nm, we took diffusion broadening into account [*Stolzenburg,* 1988]. *Berndt et al.* [2006] recently reported that the UCPC 3025A can measure particles down to ~2 nm in the case of sulfuric acid particles. We adopted their recommendation and changed the cut-off diameter from 3 nm to 2 nm. We defined the detection efficiency of the size range studied by fitting the detection efficiency function as reported by *Mertes et al.* [1995], assuming the detection efficiency is 90% and 100% for a diameter of 10 nm and 20 nm, respectively.

The newly-formed polydispersed aerosol particles drawn from the exit of the condenser unit were charged with a Polonium 210 radioactive diffusion charger, which produced both positive and negative charged particles. The charged particles then entered the DMA and the voltage applied to the nano-DMA was exponentially ramped up from 11 (corresponding to 2 nm) to 276 volt (corresponding to 10 nm) (referred to up scan) and then back down for another scan (back scan) [*Wang and Flagan,* 1990]. The sheath and excess flows were connected by a regenerative blower in a recirculation loop. The desired flow rate measured using a laminar volumetric flow meter (Alicat Scientific) was achieved by varying the voltage applied to the blower and a ratio of 1/10 for the

sample flow to sheath flow was maintained. The relative humidity was uniform upon equilibration of the sheath flows and the sample flow in this way. Hydrophobic Osmonics filters (0.45 m^2, 0.22 mm pore size) were used to minimize uptake or release of water within the recirculation loop. The UCPC/DMA sizing system was automatically controlled using data acquisition cards interfaced with LabVIEW software (National Instruments). The size-selected mono-dispersed aerosol ultimately entered the UCPC, which detects individual particles larger than 2.0 nm by growing them to an optically active size through condensation of butanol vapor. The counts were then used to generate the overall size distribution. For most of the experiments, only UCPC was used to monitor the number density of the particles, and the nucleation can be estimated by the number density and the nucleation time, which will be discussed in the next section.

2.3 Results and Discussion

2.3.1 Nucleation rate determination

The nucleation rate is defined as the formation rate of the critical nuclei, which is typically ~ 1 nm in diameter. The UCPC used in this study is only able to detect a minimum size of 2 nm in the case of sulfuric acid particles as mentioned in the above section so that the particles are undercounted. The other important parameter of the nucleation rate is the nucleation time, which was determined by the flow conditions and the location of the nucleation zone, where nucleation occurs. Since the mixing unit was kept at a temperature of ~353 K and the condenser unit was regulated at ~ 284 K, a transition zone characteristic of a dramatic decrease of temperature is expected. Figure 2.3 shows the axial temperature distribution of the nucleation system, measured using a

thermocouple attached to a movable injector. The temperature decreases along the mixing unit, and the temperature difference between the entrance and the exit of the mixing unit is around 30 K. Since the temperature is quite high (>353 K), the wall loss is minimized and no nucleation occurs in this region. The gas temperature along the axial direction dropped sharply by ~70 K in the first 10 cm of the condenser and then the temperature became almost invariant at ~284 K until it was warmed up a few degrees at the exit of the condenser. Since the relative humidity is dependent on the temperature, an axial distribution of RH was expected. We can thus determine the equilibrium composition of sulfuric acid in the H_2SO_4–H_2O system at fixed RH and temperature using the aerosol inorganic model presented by *Carslaw et al.* [1995]. We obtained an axial distribution of the equilibrium composition of sulfuric acid in the binary H_2SO_4–H_2O system. Fig 2.4 shows the axial distribution of RH and equilibrium concentration (in wt %) (solid circle) of sulfuric acid in the H_2SO_4–H_2O system. To better characterize the location where the nucleation occurs, we need to determine the axial distribution of the saturation ratio of sulfuric acid along the condenser. We calculated the saturation vapor pressure of the sulfuric acid along the condenser according to the axial distribution of the equilibrium composition and the temperature using the sulfuric acid data from Perry's Chemical Engineers' Handbook [*Perry et al.,* 1997] so that we can determine the axial distribution of the equilibrium concentration of sulfuric acid. The saturation ratio of the sulfuric acid is dependent on the sulfuric acid concentration, and for simplification a sulfuric acid concentration of 1×10^9 molecules cm^{-3} was assumed to calculate the saturation ratio of sulfuric acid with respect to the equilibrium sulfuric acid

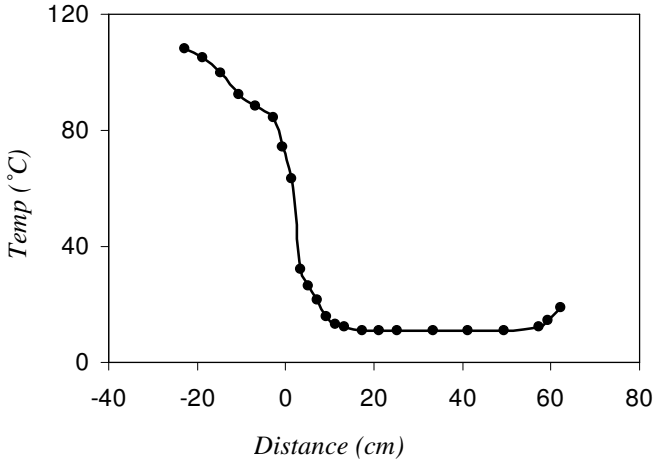

Figure 2.3. The axial temperature distribution in the nucleation system. The distance 0 was defined as the beginning of the condenser unit.

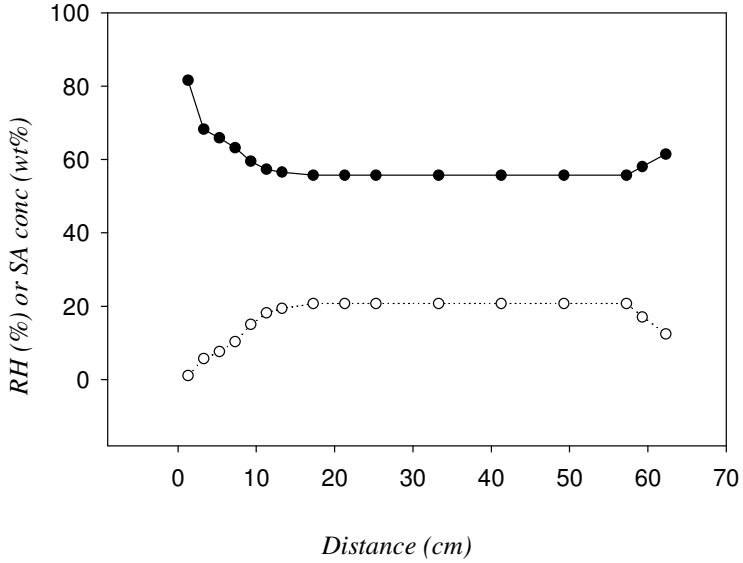

Figure 2.4. The axial distribution of RH (dashed line) and equilibrium composition of sulfuric acid (solid line) along the condenser. Distance 0 was defined in the same way as Figure 2.3.

composition along the condenser. Figure 2.5 shows the axial distribution of the saturation ratio without (triangle) and with (square) diffusion loss correction (the wall loss of sulfuric acid will be discussed in the next section). The saturation ratio was increased dramatically (from 0.005 at 1.3cm to 5600 at 9.3cm) with the sharp decrease of the temperature in the first 10 cm of the condenser, strongly indicating that the nucleation occurs at the very beginning of the condenser, since the H_2SO_4–H_2O nucleation can be considered as quasi-unary nucleation of H_2SO_4 in equilibrium with H_2O vapor [*Yu,* 2004]. The total flow in the condenser was 1.5 L min^{-1} and the nucleation time was estimated to be ~ 7.2 s. It should be pointed out that since the particles were undercounted, the apparent nucleation rate determined in this study was smaller than the real nucleation rate. To better characterize the formation and growth of

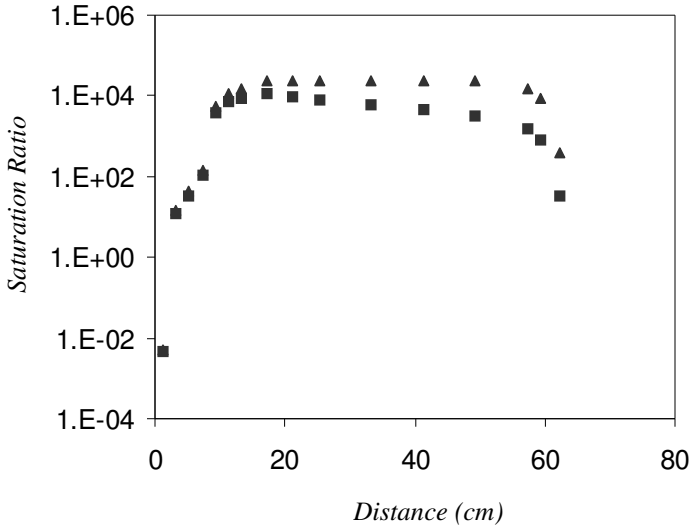

Figure 2.5. The axial distribution of the saturation ratio with (square) and without (triangle) diffusion loss correction.

new particles, a 120 cm long movable injector was used to measure the particle number density along the axial direction of the condenser. Figure 2.6 shows the particle number density as a function of the movable injector position relative to the entrance of the condenser under typical experimental conditions. There is almost no particle, or very few particles (particle diameter smaller than 2 nm), produced up to a length of 40 cm of the condenser and then a sharp increase in the particle counts was observed. The particle counts still increase at the exit, indicating that nucleation still occurs at the end of the condenser. Since a short (~ 30 cm) 3/8 inch diameter conductive tubing was used between the exit and the inlet of the UCPC, the residence time is expected to be very short and we can assume there is no nucleation in this portion. As mentioned above, the nucleation occurs almost at the beginning of the condenser and the particles were detected only after a certain length of the condenser (e.g. after 40 cm), indicating that the

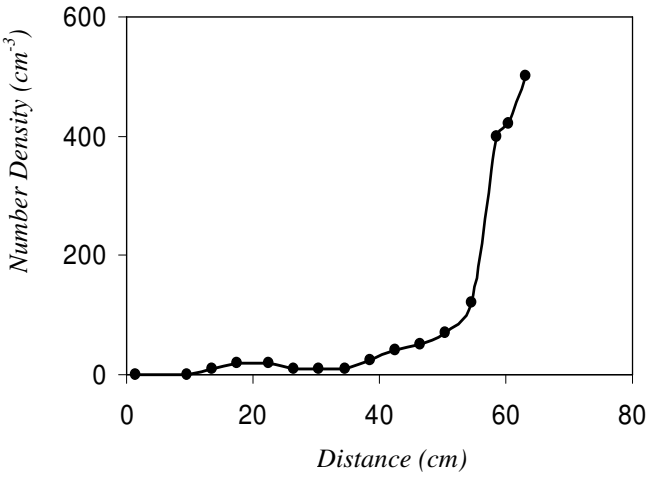

Figure 2.6. The axial distribution of particle number density in the nucleation system. The measured sulfuric acid concentration was ~ 3 x 10^9 molecules cm^{-3}.

particles grow from ~ 1 nm to 2 nm within a distance of 40 cm. A growth rate of ~ 0.2 nm sec^{-1} was estimated based on the above observation and a particle diameter of 2.5 nm can be obtained at this growth rate, indeed consistent with the measured particle size distribution at the end of the condenser. It should be pointed out that the growth rate is dependent on the sulfuric acid concentration introduced, and it was bigger under higher sulfuric acid conditions.

2.3.2 Losses of nucleating precursors in the nucleation system

Wall loss for nucleating species is an important issue and correction needs to be made in order to better understand the processes of the formation and growth of the new particles. Since sulfuric acid and organic acid were detected upstream before they entered the condenser, the loss was estimated from the detection point to the end of the condenser. Diffusion loss of sulfuric acid and organic acid to the mixing region wall was minimized because the wall was heated, and this loss is expected to be small (~2%) compared to the loss on the wall of the condenser. A corrected diffusion coefficient of 0.0871 cm^2 sec^{-1} at 284 K [*Hanson and Eisele,* 2000] was used to estimate the wall loss of sulfuric acid on the condenser. A pseudo-first order loss [*Ball et al.,* 1999] was assumed for simplicity and the loss is proportional to the diffusion coefficient and inversely proportional to the square of the diameter of the condenser. Since the temperature is not uniform along the condenser, a temperature dependent loss was estimated and a power dependence of 1.75 on temperature was used to determine the diffusion coefficient [*Zhang et al.,* 1997] for temperatures other than 284 K. For simplicity, we divided the condenser into several isothermal segments based on the axial

temperature distribution (Figure 2.3) and calculated the diffusion loss of each segments and hence the total diffusion loss can be obtained. Loss of sulfuric acid to particles which is not a first order process in sulfuric acid concentration is insignificant compared to the wall loss. For example, for the largest number concentration of ~ 10^4 particles cm^{-3} for binary nucleation, the loss to 4–9 nm particles is estimated to be 3 orders of magnitude lower than that of the wall loss [*Viisanen et al.,* 1997]. Loss induced by thermal-driven convection due to the dramatic decrease of temperature might be also important. However, this loss is not included in the concentration correction since it is very difficult to quantify. Approximate 90% of the overall diffusion loss of sulfuric acid was adopted for the whole condenser. For cis-pinonic acid, however, there is no available gas-phase diffusion coefficient in the literature and it was estimated by the method described by *Fuller et al.* [1966], with the improvements suggested by *Marrero and Luecke* [1996]. The gas-phase diffusion coefficient for cis-pinonic acid is calculated to be ~ 0.0543 cm^2 sec^{-1} at 284 K and a first order loss constant of 0.322 sec^{-1} was obtained. Similar to the case of sulfuric acid, we did not account for other losses (e.g. loss to the particles and the convection loss). We determined the axial concentration distribution of cis-pinonic acid using the same methods as sulfuric acid and an overall diffusion loss is estimated to be 76%. Ammonia suffers severe diffusion loss to the wall due to its high diffusion coefficient (~0.228 cm^2 sec^{-1} at 284 K) [*CRC handbook,* 2003] and the total loss was estimated to be more than 99.9%. Loss of water is not an issue due to its high concentration in the flow system and a thin layer of water film was quickly formed on the wall, which can then be in equilibrium with the water vapor in the

condenser. Figure 2.7 depicts the axial concentration distribution of sulfuric acid, cis-pinonic acid and ammonia assuming a concentration of 1 x 10^9 molecule cm^{-3} at the entrance of the condenser. It should be pointed out that all the losses account only for the diffusion losses and the actual losses might be less once the wall was saturated.

2.3.3 Binary nucleation of sulfuric acid and water

The binary H_2SO_4–H_2O nucleation experiments were performed at three different relative humidities (RH = 5.6%, 13.2%, 20.2%) to test the system stability and reproducibility. A N_2 flow of 60–120 sccm was introduced through the bubbler containing concentrated H_2SO_4 (~98 wt %) and a saturation vapor pressure of 10^{-4} torr

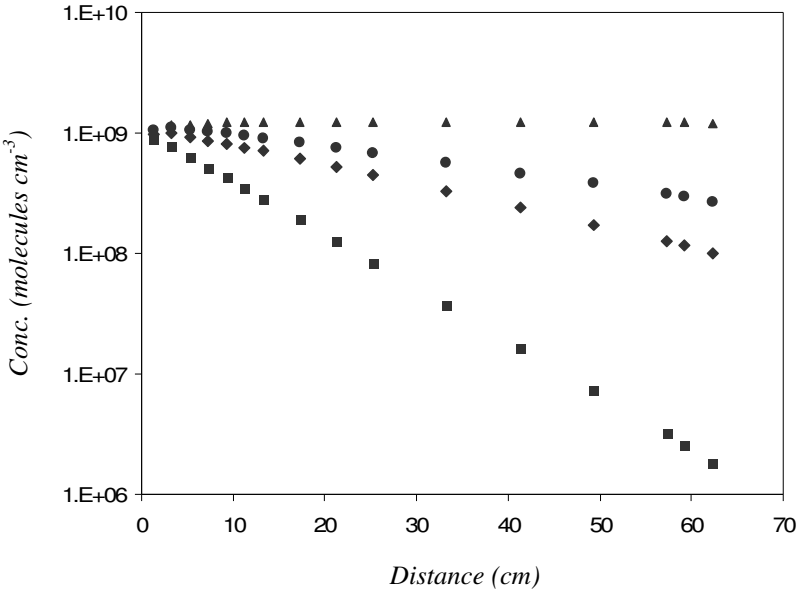

Figure 2.7. The axial concentration distribution of sulfuric acid (diamond), cis-pinonic acid (circle) and ammonia (square), assuming a concentration of 1 x 10^9 molecules cm^{-3} at the beginning of the condenser.

was estimated at a bath temperature of 311K. A gaseous sulfuric acid concentration of about 5 x 10^9 – 2 x 10^{10} molecules cm^{-3} was calculated assuming a saturation ratio of 10% for sulfuric acid [*Ball et al.,* 1999]. However, in-situ measurements of sulfuric acid downstream of the mixing unit showed that only 15%–40% of the volumetrically determined concentration was measured. The possible reasons for this low measured ratio were attributed to a lower saturation ratio than the assumed 10% and/or significant wall loss during transportation of sulfuric acid through the mixing unit and through the mass spectrometry system. The sulfuric acid concentration corresponds to the concentration where nucleation occurs, which is the upstream measured concentration. The concentration thereafter might be less due to continual loss to the wall. Figure 2.8 shows the binary H_2SO_4–H_2O nucleation rate (J) as a function of sulfuric acid concentration at three different RHs, plotted as log J versus log [SA], where [SA] is the sulfuric acid concentration. The sulfuric acid concentrations are in the range of 8.0 x 10^8 –1.6 x 10^{10} molecules cm^{-3} and the nucleation rates cover a range of 0.1–10^3 particles cm^{-3} sec^{-1}. At fixed RH, the nucleation rate J can be expressed as $J = A [SA]^X$, where A is a RH-dependent coefficient, [SA] is the concentration of sulfuric acid, assuming A and X is independent of sulfuric acid concentration. It can be seen that the nucleation rate J increases with sulfuric acid concentration and the dependence of X of J on sulfuric acid concentration is fitted to be around 5 at RH=5.6% and 3 at RH = 20.2%. This power dependence is in agreement with the results from the recent in-situ sulfuric acid generation method by *Berndt et al.* [2005], which also showed a power dependence of 3–5 and suggested a trimer or dimer nucleation mechanism. However, the sulfuric acid

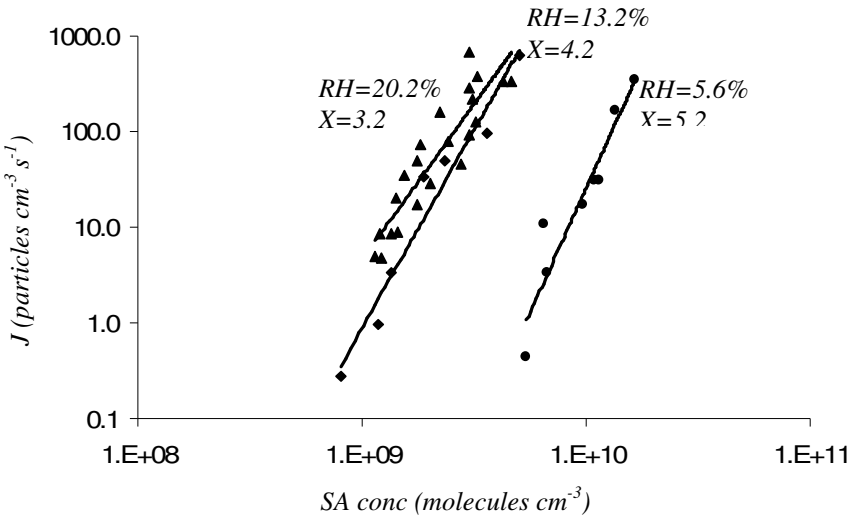

Figure 2.8. The binary H_2SO_4–H_2O nucleation rate J as a function of H_2SO_4 concentration at various RHs in logarithmic scales.

concentration used in their experiments is 2 orders of magnitude lower than ours and no mechanistic explanation was provided for the observed particle growth at such low sulfuric acid concentration. Interestingly, the results from our previous study and Ball et al.'s showed a 8-power dependence on sulfuric acid concentration, indicating a substantial barrier for formation of critical nuclei under these experimental conditions. In our present experiment, the nucleation zone was kept at 284 K, a temperature substantially lower than the one in our previous experiment and Ball et al.'s, which might be an explanation for the discrepancy of the power dependency.

The effect of RH on J is less pronounced at higher RH, as depicted in Figure 2.9, the J curves at RH = 13.2% and 20.2% are very close to each other. The observed lesser dependence of J on higher RH is consistent with other experimental results of the binary

H_2SO_4–H_2O nucleation. *Ball et al.* [1999] reported a dramatic change in the dependency of J on RH in the parameterization change below RH = 8%, and *Berndt et al.* [2005] showed similar pattern at higher RH (e.g. between RH = 28% and 49.5% in Figure 3 in their paper). As discussed in the Chapter I, hydration of sulfuric acid in the gas phase has a stabilizing effect on the vapor and it decreases the concentration of free sulfuric acid, resulting in the decrease of the nucleation rate, which provides an explanation for the observed lesser humidity dependence on high relative humidity. In addition, more scattering of the data can be seen in Figure 2.8 at higher RH, suggesting the detection of sulfuric acid becomes more complicated at higher humidity possibly due to the formation of more hydrate cluster ions in the mass spectrometer.

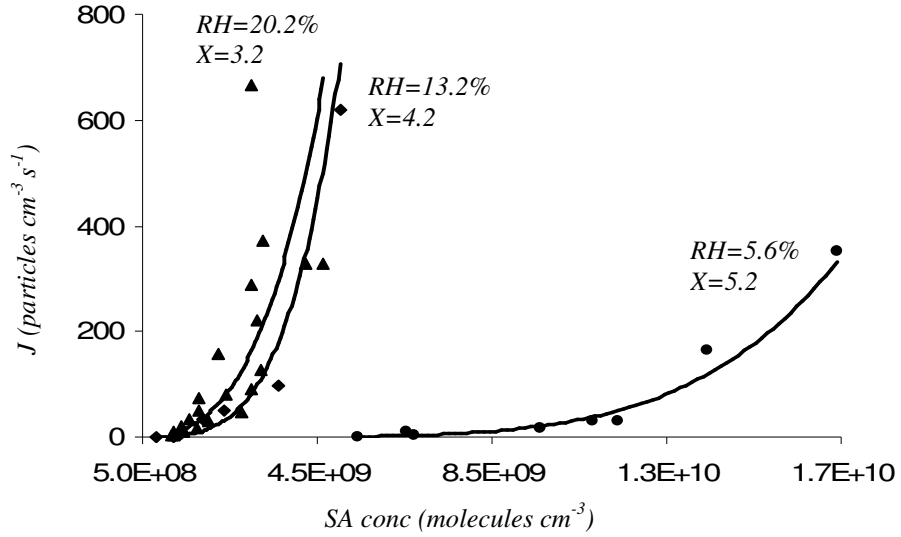

Figure 2.9. The same figure as Figure 2.8, the only difference is that both axes are in linear scales.

2.3.4 Vapor pressure measurement of cis-pinonoic acid

We choose cis-pinonic acid as a model biogenic organic acid to evaluate its role in new particle formation since cis-pinonic acid has been identified as one of the major aerosol components in the pinenes–O_3 oxidation experiments. In order to better understand the role of biogenic organic acids in new particle formation, knowledge of physical parameters (e.g., vapor pressure) is needed. However, only one such study was found in the literature. *Bilde and Pandis* [2001] measured the temperature-dependent vapor pressures of the organic acids (e.g., pinic acid, trans-norpinic acid) using the tandem differential mobility analyzer (TDMA) technique. Measurement of the vapor pressure of cis-pinonic acid in their study was proven to be problematic due to sample impurity. We measured the vapor pressure of cis-pinonic acid (solid powder) using the ID–CIMS technique over the temperature range of 303–329 K. We introduced cis-pinonic acid directly into the drift tube via a heated inlet and the pressure in the cis-pinonic bubbler (P_b) was measured using a Baratron (MKS, 10 torr full range). Cis-pinonic acid was detected and quantified using negative ions (CO_3^- and CO_4^-) as reagent ions. Cis-pinonic acid in concentrations of 5 x 10^7 – 1 x 10^{10} molecule cm^{-3} was introduced into the drift tube, detected at m/z = 183 (ions of (cis-pinonic acid - H)), 244 (cis-pinonic acid–CO_3^-) and 216 (cis-pinonic acid–O_2^-), with ion at m/z = 216 being the strongest. The volumetrically determined cis-pinonic acid can be expressed as

$$[cisPA] = x \frac{f}{\sum f} \frac{P_0(T)}{P_b} \frac{P_{dt}}{760} \times 2.47 \times 10^{19} \qquad (2.5)$$

where f , ∑f is the flow rate through the cis-pinonic acid bubbler and the total flow in the

drift tube, respectively. $P_0(T)$, P_{dt} is the saturation vapor pressure of cis-pinonic acid at temperature T and the pressure in the drift tube, respectively. x is the saturation ratio of cis-pinonic acid in the bubbler. The concentration of cis-pinonic acid in the drift region can also be formulated using the ID–CIMS technique as follows,

$$[\,cisPA\,] = \sum \frac{S_i}{k_i S_{CO_X^-} t} \approx \frac{1}{kt}\left(\frac{S_{183} + S_{244}}{S_{CO_3^-}} + \frac{S_{216}}{S_{CO_4^-}} \right) \tag{2.6}$$

where S_i, $S_{CO_X^-}$ are the ion counting rate of the corresponding cis-pinonic acid ions and the reagent ions, respectively. The ion-molecule rate constants of the reactions of cis-pinonic acid with CO_3^- and CO_4^- were calculated to be 2.2 and 2.1 x 10^{-9} cm^3 $molecule^{-1}$ sec^{-1}, respectively. For simplicity, we chose the rate constants of the above ion-molecule reactions as 2 x 10^{-9} cm^3 $molecule^{-1}$ sec^{-1}. We then obtained a relationship between the flow rate f and the pressure incorporated counting ratio P_s,

$$f = \frac{1}{ckt} P_S \tag{2.7}$$

where

$$c = \frac{x}{\sum f} \frac{P_0(T) P_{dt}}{760} \times 2.47 \times 10^{19}$$

$$S = \left(\frac{S_{183} + S_{244}}{S_{CO_3^-}} + \frac{S_{216}}{S_{CO_4^-}} \right) \quad \text{and} \quad P_S = P_b S$$

By plotting the flow f as a function of Ps, we can determine $P_0(T)$ as

$$P_0(T) = \frac{760 \sum f}{2.47 \times 10^{19} xktP_{dt} S_l} \tag{2.8}$$

where the slope of the linear least square fit is $S_l = 1/(ckt)$. Figure 2.10 shows a plot of f

as a function of P_s at 303 K. By assuming a saturation ratio of 10% (similar to that of sulfuric acid), we calculated the vapor pressure of cis-pinonic acid over a temperature range of 303–329K. Figure 2.11 depicts the vapor pressure of cis-pinonic acid in logarithmic scale versus the inverse of temperature (1/T). The heat of vaporization of cis-pinonic acid was determined to be 27.3 kcal mol^{-1} according to the Clausius–Clapeyron equation and it is independent of the saturation ratio of cis-pinonic acid in the bubbler. We obtained an explicit expression for the vapor pressure over the temperature range of 296–329K, $\log_{10}(P_0/Pa)=-5970.27K/T + 16.48$. We found that the vapor pressure of cis-pinonic acid at 296 K (assuming valid extrapolation of the data) was a factor of 3 higher than that obtained from *Bilde and Pandis* [2001], possibly due to an assumption of a lower saturation ratio (eq. 2.8).

2.3.5 Ternary nucleation of cis-pinonic acid–sulfuric acid–water

We have discussed the binary H_2SO_4–H_2O nucleation and the vapor pressure of cis-pinonic acid in the previous sections. For ternary nucleation involving cis-pinonic acid, we first established relatively stable particle counts of the binary H_2SO_4–H_2O system. Cis-pinonic acid with desired concentration was then introduced into the binary system to determine its effect on the particle counts and the particle size distribution to assess its role in new particle formation. Cis-pinonic acid was detected at m/z = 216 using $CO_2 \bullet O_2^-$ as reagent ions. Surprisingly, the masses at m/z = 183 and 244 were found to be weak. In contrast certain amounts (30%) of cis-pinonic acid was detected at these two masses in the vapor pressure measurement, most likely due to a substantially lower (several orders of magnitude) concentration of cis-pinonic acid being admitted to the

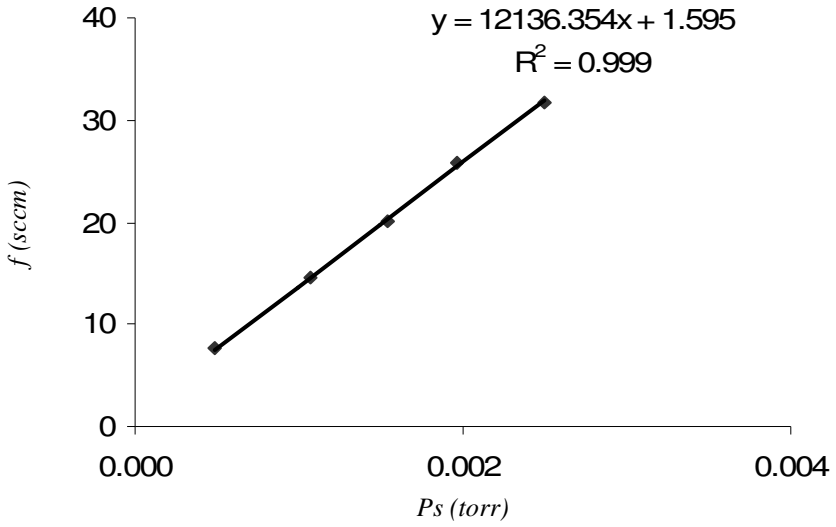

Figure 2.10. Plot of flow *f* as a function of P_s at a bath temperature of 303 K.

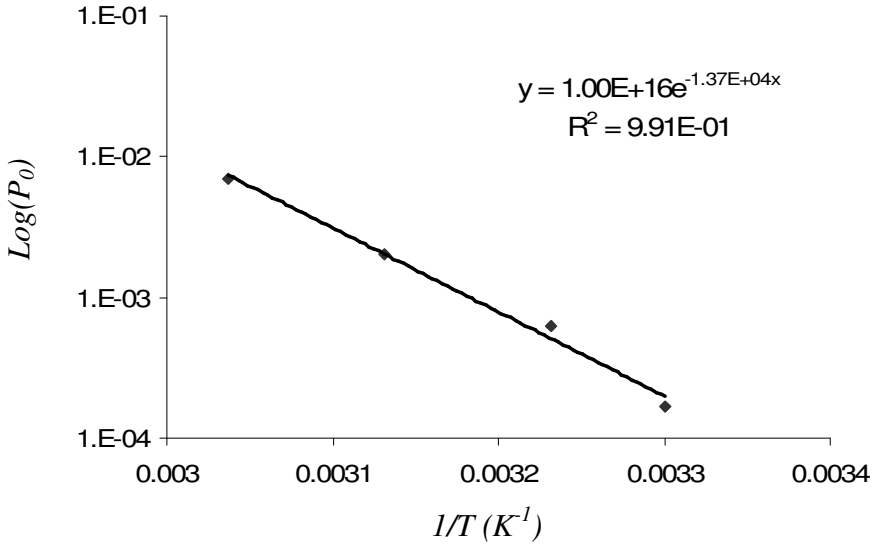

Figure 2.11. Plot of the vapor pressure of cis-pinonic acid in logarithmic scale versus the inverse of temperature (1/T).

drift tube. The uncertainty in the measured concentration of cis-pinonic acid was associated with the uncertainty in the ion-molecular rate constants using the ADO theory and the calculated ion-molecular reaction time. We estimated an uncertainty of less than 30% in our measured concentration of cis-pinonic acid. The effect of cis-pinonic acid is represented by an enhancement factor (EF), which is defined as the ratio of the nucleation rate in the presence of cis-pinonic acid versus that in the absence of cis-pinonic acid. Fig. 2.12 shows the nucleation rate J as a function of H_2SO_4 concentration in the absence and in the presence of various concentration of cis-pinonic acid. The nucleation rate increased to some extent, depending on the cis-pinonic acid added. For example, the nucleation rate increases by a factor of 4–10 in the presence of 82 ppt cis-pinonic acid for RH = 5.6%. The enhancement became less pronounced with increasing RH. For example, an enhancement factor of 5–14 was obtained only when ~240 and 280 ppt cis-pinonic acid was added at RH = 13.2% and 20.2%, respectively. The change of the power dependence of the nucleation rate on sulfuric acid concentration at various concentration of cis-pinonic acid was small for RH = 5.6 and 13.2%, while for RH = 20.2% this change was found to be a little bigger (from 3.1 in the absence of cis-pinonic acid to 2.3 in the presence of 280 ppt cis-pinonic acid). Figure 2.13 depicts the dependence of the nucleation rate on organic acid concentration by fitting the nucleation J vs organic acid concentration. For example, the dependence becomes weaker with increasing sulfuric acid concentration. The power dependence of around 1.4 changed to 0.7 when the sulfuric acid concentration increased from 8×10^8 to 5×10^9 molecules cm^{-3} at a relative humidity of 13.2%. From the dependence of J on sulfuric acid and

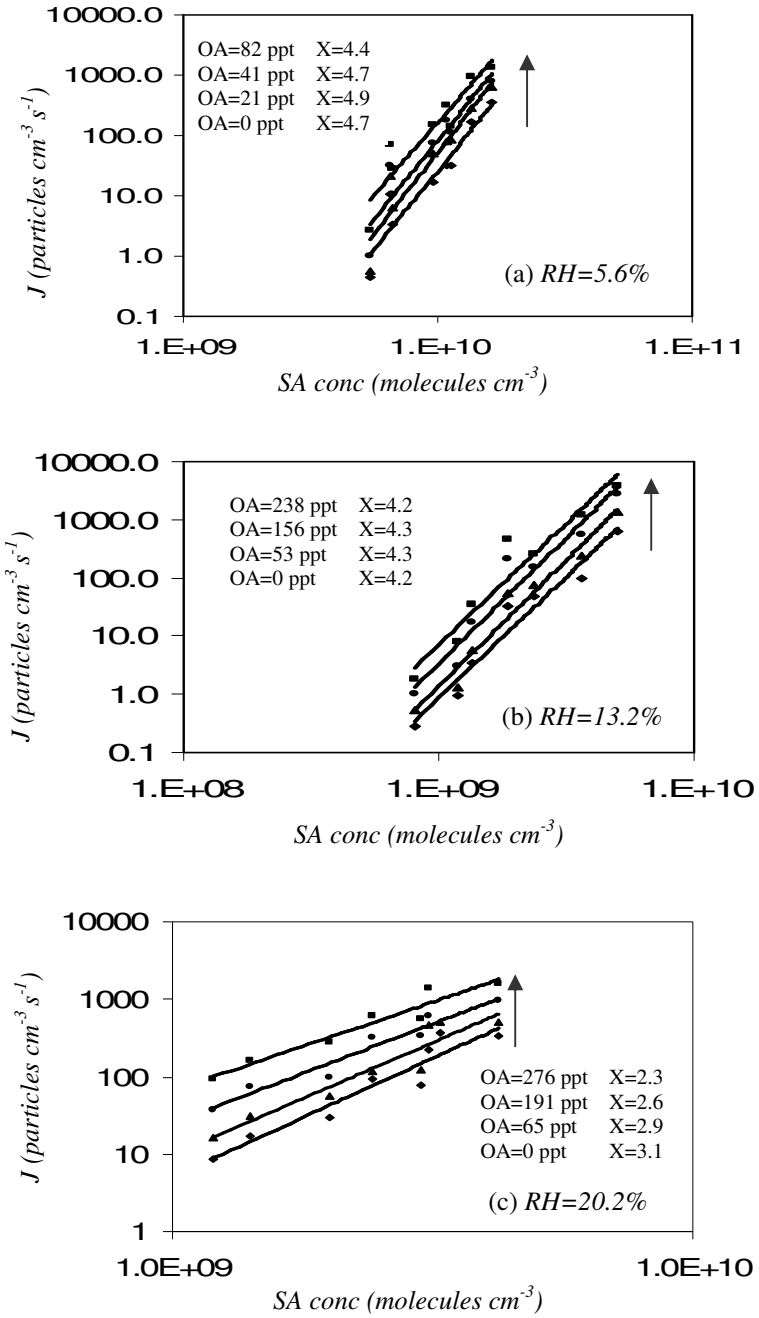

Figure 2.12. The ternary (H_2SO_4–cis-pinonic acid–H_2O) nucleation rate J as a function of H_2SO_4 concentration at various RHs.

cis-pinonic acid, we estimated the critical cluster was composed of 3-5 H_2SO_4 and 1 cis-pinonic acid.

The shifting of the particle size distribution to larger size is an indicator of the involvement of cis-pinonic acid in new particle formation. As shown in Figure 2.14, the average particle size was increased from 2.31 to 2.53, 2.75 nm at cis-pinonic acid concentration of 0, 190, 280 ppt, respectively, corresponding to a volume change of 30% (70%) from the binary nucleation to the ternary nucleation in the presence of 190 (280) ppt cis-pinonic acid.

2.3.6 Nucleation involving ammonia

We carried out preliminary tests for the enhancement from ammonia on the binary H_2SO_4–H_2O nucleation. Similar to the ternary nucleation of organic acid–H_2SO_4–H_2O, ammonia, with volumetrically-determined concentration of 150 and 300 ppt, was introduced upstream before the condenser once the particle counts of the binary H_2SO_4–H_2O were stable for ~2 hrs. We performed experiments under two relative humidities (RH = 13.2 % and RH = 20.2%) with various concentrations of sulfuric acid. Shown in Figure 2.15 is a plot of the nucleation rate as a function of sulfuric acid concentration in the absence and presence of ammonia (150, 300 ppt). At a lower concentration of ammonia (150 ppt), the enhancement factors fall in the broad range of 3–18, while much higher enhancement factors (50–190) were observed at a higher concentration of ammonia (300 ppt). The ammonia concentration drops almost 3 orders of magnitude or even higher across the condenser due to the wall loss and hence hinders further contribution of ammonia to both new particle formation and growth. We also measured

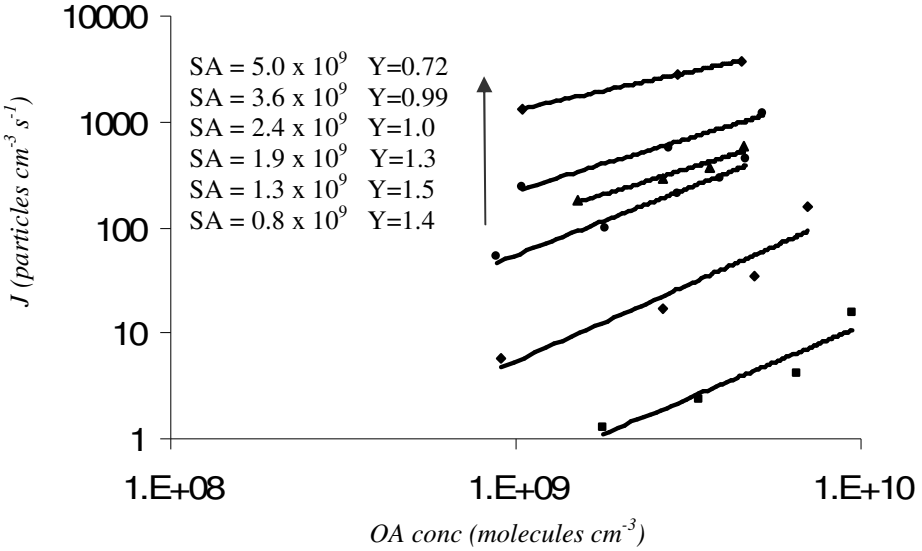

Figure 2.13. The ternary (H_2SO_4–cis-pinonic acid–H_2O) nucleation rate J as a function of cis-pinonic acid concentration at RH = 13.2%.

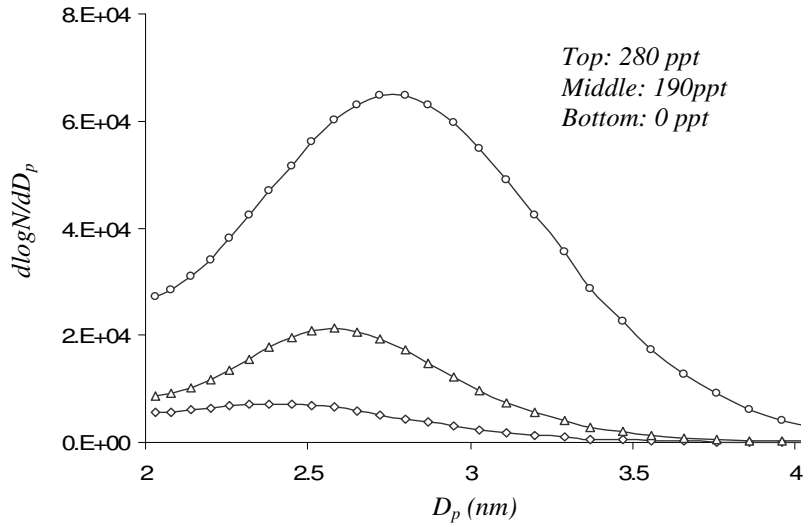

Figure 2.14. The size distribution of the ternary nucleation of H_2SO_4–cis-pinonic acid–H_2O in the presence of cis-pinonic acid.

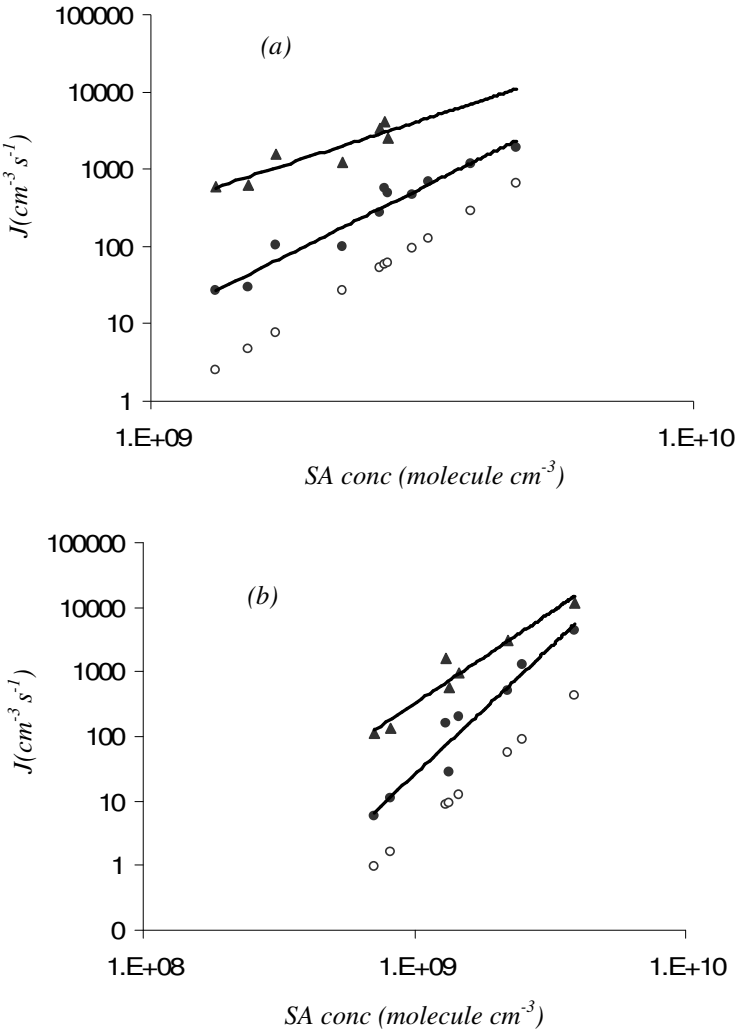

Figure 2.15. The nucleation rate (J) of the ternary H_2SO_4–H_2O–NH_3 as a function of sulfuric acid concentration at (a) RH = 13.2% and (b) 20.2%. Note that the sulfuric acid concentration was not measured but fitted to the measured concentration according to the particle counts in the binary H_2SO_4–H_2O nucleation.

the size distribution of the particles and no obvious growth of the particles was observed. We attribute this observation to the neutralization of sulfuric acid by adding ammonia to the sulfate particles and meanwhile losing the water from the particles. Since the molecular weights of water and ammonia are close, the loss of water and the gain of ammonia are balanced, leading to the observed no growth of the new particles. The results indicate that ammonia can actively enhance the binary H_2SO_4–H_2O nucleation. However, these enhancements are significantly smaller than those predicted by the classical nucleation theory, which needs to be further investigated.

2.4. Summary

We performed experiments to investigate new particle formation and growth using on-line ID–CIMS detection of gas-phase precursors and the UCPC/DMA system for particle size/count measurements. The nucleation zone was characterized by measuring the axial temperature and particle distribution. Both the concentration and the saturation ratio profiles along the condenser were determined and the growth rate of the newly-formed particle was estimated to provide valuable information toward understanding of new particle formation and growth in the flow tube system. Vapor pressure measurement of cis-pinonic acid by ID–CIMS demonstrated the unique capability of this technique and provided an alternative tool to measure the vapor pressure of low volatile compounds. The power dependence of the binary H_2SO_4–H_2O nucleation rate on sulfuric acid concentration was found to be ~ 3–5 in the RH range of 6–20%. The nucleation rate of the binary H_2SO_4–H_2O system was considerably enhanced in the presence of cis-pinonic acid or ammonia and more efficient

enhancement was found for ammonia at the same concentration level. However, the experimental enhancements of ammonia were found to be much less than those predicted by classical nucleation theory. The results shows both cis-pinonic acid and ammonia can efficiently enhance the binary sulfuric acid–water nucleation under experimental conditions. Considering the abundance of the biogenic pinenes in the forested area, carboxylic acids from the oxidation of these pinenes may contribute considerably to the new particle formation and the global organic aerosol loading.

CHAPTER III

THEORETICAL INVESTIGATION OF NEW PARTICLE FORMATION

3.1. Introduction

Regional nucleation events are frequently observed at various locations [*Kulmala et al.,* 2004]. New particle formation involving sulfuric acid as a principal atmospheric nucleating agent represents an important contributor of nucleation mode aerosols [*Kanakidou et al.,* 2005]. Field measurements have consistently shown that the contribution of sulfuric acid to the particle growth is substantially low during the nucleation events in various locations in the USA [*Kulmala et al.,* 2004]. Other field observations also indicate that atmospheric new particle formation is essentially multi-component. Other likely candidates for the nucleation precursors include the ubiquitous species NH_3 and organic compounds. Mixing ratios of NH_3 up to a few ppb have been measured in the atmosphere [*Nowak et al.,* 2006]. Classic and kinetic nucleation models predict much higher nucleation rates in the presence of only ppt levels of NH_3 than those from laboratory measurement in the presence of even ppb to ppm levels of NH_3 for ternary nucleation of H_2SO_4–H_2O–NH_3 [*Coffman and Hegg,* 1995; *Kim et al.,* 1998; *Ball et al,.* 1999; *Korhonen et al.,* 1999; *Napari et al.,* 2002a, b; *Hanson and Eisele,* 2002]. Field measurements have shown that atmospheric aerosol particles contain a substantial fraction of organic compounds [*Kanakidou et al.,* 2005]. As discussed in previous Chapters, recent laboratory experiments indicate that new particle formation in the binary sulfuric acid–water system is considerably enhanced in the presences of sub ppb levels of biogenic organic acid (e.g. cis-pinonic acid) and aromatic acids (e.g. benzoic

acid, m-toluic acid, p-toluic acid) [*Zhang et al.,* 2004]. However, the detailed roles of ammonia and organic compounds in new particle formation still remain largely unknown.

Although atmospheric nucleation involving sulfuric acid has received intensive attention over decades and continuous progress has been made toward understanding the nucleation mechanism in the atmosphere, nucleation at a fundamental microscopic molecular level is still poorly understood. It is commonly recognized that molecular complex and pre-nucleation cluster formations are the initial stages for new particle formation. The molecular complexes and small clusters (usually smaller than 1 nm) containing up to several tens of molecules bridge the gap between single molecules and larger particles (e.g. > 3 nm) and play a vital role in the atmospheric new particle formation process. Knowledge of the thermodynamic properties of these complexes and clusters is still very limited and the kinetic and dynamic molecular processes for formation of molecular aggregates also remain largely unclear, hindering efforts to predict atmospheric nucleation rates.

Atmospherically relevant hydrogen-bonding complexes have been the subjects of numerous computational studies in recent years. The complexes and clusters of sulfuric acid with other species (e.g. water, ammonia and organics) are formed via hydrogen bonds of intermediate strength. Currently, the microscopic mechanism for atmospheric nucleation of sulfuric acid–water system is not known, but in general hydration is most likely the first step in this process based on the fact that most of the gaseous sulfuric acid exists in hydrate form due to its large affinity toward water. The next step is likely the

formation of clusters by condensation of sulfuric acid and other trace species. Previous quantum chemical calculations were focused on sulfuric acid hydrates $(H_2SO_4)_x(H_2O)_y$ (x=1–3, y=0–9) or sulfuric acid–ammonia and their hydrate clusters $(H_2SO_4)_x(H_2O)_y(NH_3)_z$ (x = 1–2, y = 0–5, z = 1). The sulfuric acid monohydrate is the first target complex to be thoroughly investigated by quantum chemical calculations. *Kurdi and Kochanski* [1989] performed ab initio calculations to investigate the monohydrate assuming rigid monomers, and the results indicate that the ionic complex is less stable than the neutral one. *Arstila et al.* [1998] reported a density functional study of sulfuric acid mono-, di- and trihydrates and they found proton transfer is unlikely to occur in the mono- and dihydrate, while low energy barrier allow proton transfer to occur in the trihydrate, consistent with the results by *Bandy and Ianni* [1998], showing that there exists deprotonation in the clusters of $H_2SO_4(H_2O)_n$ (n = 3–7). *Re et al.* [1999] performed a molecular orbital study to explore the stability of the hydrated clusters containing up to 5 water molecules and the results indicate the coexistence of both neutral and ionic structures under investigation. *Ding and Laasonen* [2003, 2004] found that sulfuric acid can be partially deprotonated when three water molecules are present in the cluster and completely deprotonated in hydrated clusters containing eight or more water molecules. For clusters containing two sulfuric acid molecules, the deprotonation of both acids will happen at the cluster containing five or more molecules of water, in contradiction to the results from *Ianni and Bandy* [2000], which show no deprotonation for clusters containing up to 6 water molecules. *Al Natsheh et al.* [2004] performed DFT calculations to investigate the molecular structures of the mono-, di-, and trihydrates of

the sulfuric acid and the results imply that high dipole moments of these hydrates are important factors for the ultrafine particle formation in the atmosphere. Recently, *Kurten et al.* [2006] revisited gas phase sulfuric acid monohydrate and ammonium hydrogen sulfate using different ab initio methods and density functional theory with various basis sets. Their results indicated that different thermochemical parameters (e.g. reaction free energies) were predicted using different methods and basis sets partially due to the basis set superposition error (BSSE) and harmonic approximation. *Ianni and Bandy* [1999] presented a density functional study of clusters $NH_3 \cdot H_2SO_4 \cdot nH_2O$ (n = 0–5) and formation of the ion pair (NH_4^+ and HSO_4^-) is found to be energetically favored until the cluster contains 4 water molecules (n = 4). Their results showed no role of NH_3 in new particle formation. In contrast, another DFT calculation showed that the $NH_3 \cdot H_2SO_4$ exists as the ion pair NH_4^+ and HSO_4^- in the presence of one or two water molecules. A recent density functional study indicated that ammonia is bonded much more strongly to the sulfuric acid–water clusters than water, implying that the ammonia may play a role in new particle formation [*Kurten et al.,* 2007].

From the microscopic molecular point of view, how organic compounds participate in nucleation process remains an open question. Stable carboxylic acid dimers have been determined experimentally [*Emmeluth and Suhm,* 2003; *Nandi et al.,* 2005] and theoretically [*Sloth et al.,* 2004; *Gora et al.,* 2005; *Nadykto and Yu,* 2007]. It has been speculated that formation of stable dimers between carbonxylic acids might be the first step in the new particle formation for the ozonolysis of pinenes [*Koch et al.,* 2000; *Capouet and Muller,* 2006]. Recent quantum chemical calculations indicate that

formation of the unusually stable aromatic acid–sulfuric acid complex likely reduces the nucleation barrier and hence is responsible for the observed enhancement of the binary H_2SO_4–H_2O nucleation in the presence of sub ppb levels of aromatic acids [*Zhang et al.,* 2004]. Very recently, *Nadykto and Yu* [2007] performed quantum chemical calculations to investigate the thermodynamic stability of the hydrogen-bonded complexes of small carboxylic acids (e.g. formic and acetic acid) with free and hydrated sulfuric acid, and with ammonia. Their results indicate that both organic acids and ammonia may have efficiently stabilizing effects on the binary H_2SO_4–H_2O clusters and the organic acids can interact actively with ammonia.

In this study, we report density functional and ab initio molecular orbital study on the molecular complexes of atmospheric aerosol nucleating precursors (e.g. sulfuric acid, organic acids, water and ammonia). The optimized geometries of the complexes and clusters were determined using density functional theory, and the energies were calculated for each stationary point using MP2 and CCSD(T) theories with various basis sets. We employed quantum theory of atoms in molecules (QTAIM) [*Bader,* 1990] to elucidate the nature of the hydrogen bonds of these complexes and clusters and reveal their roles in new particle formation. In addition, we also performed molecular dynamic simulations (MDS) to investigate the fluctuation and conformational changes and to test the stability of the ternary cis-pinonic acid–sulfuric acid–water clusters and estimate the size of the clusters.

3.2. Theoretical Methods

Ab initio orbital molecular calculations were performed on an SGI Altix 3700 supercomputer using the Gaussian 03 software package [*Frisch et al.,* 2003]. All the species were treated with the restricted Hartree-Fock (RHF) formulation. Geometry optimization for complexes and their monomers was executed using Becke's three parameter hybrid method employing the LYP correction function (B3LYP) in conjunction with the split valence polarized basis set 6-31G(d,p). Harmonic vibrational frequency calculations were made using B3LYP/6-31G(d,p) to confirm the energy minima for all the structures of the relevant complex and monomers. The IR spectra for the complexes can be obtained from the frequency calculations. The optimized structures were then employed in single-point energy calculations using frozen core second-order Møller-Plesset perturbation theory (MP2) and coupled-cluster theory with single and double excitations including perturbative corrections for the triple excitations (CCSD(T)) with various basis sets. Recently, the level of ab initio theory applied to complex organic radical species arising from atmospheric hydrocarbon oxidation has been evaluated on the basis of computational efficiency and accuracy [*Lei et al.,* 2000]. A procedure involving determination of a correction factor associated with basis set effects evaluated at the MP2 level and subsequent correction to the energy calculated at a higher level of electron correlation with a moderate size basis set has been developed for accurate energy description [*Lei et al.,* 2000]. The CCSD(T)/6-31g(d) energies were then corrected using the basis set correction method, corresponding to the CCSD(T)/6-31g(d) + CF. Previous work has shown that this method has been validated for several

isoprene reactions initiated by OH, Cl, NO_3, and O_3 [*Lei et al.,* 2000; *Lei and Zhang,* 2000; *Suh et al.,* 2001; *Zhang and Zhang,* 2002; *Zhao et al.,* 2003], toluene reactions initiated by OH and NO_3 [*Suh et al.,* 2002; *Suh et al.,* 2003; *Suh et al.,* 2006], pinenes initiated by OH and O_3 [*Fan et al.,* 2005; *Zhang and Zhang,* 2005] and xylenes initiated by OH [*Fan and Zhang,* 2006].

The topological analysis was performed using quantum theory of atoms in molecules (QTAIM) of *Bader* [1990] with the AIM2000 package [*Biegler-Konig,* 2000; *Biegler-Konig et al.,* 2001; *Biegler-Konig and Schönbohm,* 2002.] at B3LYP/6-31G(d,p) level to investigate the nature of hydrogen-bonded complexes. We focused on the topological properties (e.g. charge density and its Laplacian, energy density) at hydrogen bond critical points (BCPs). In addition, we carried out molecular dynamics simulation with NPT (constant number of molecule, constant pressure and constant temperature) ensemble to provide information on the fluctuation and conformational changes of the clusters. The simulation with consistent force field (CFF) was conducted using the Cerius^2 (Accelrys) software package. The equation of motion was solved using the Verlet algorithm with a time step of 1 fs. These results will provide molecular-level information (e.g. the shape and the dimension of the clusters), which will help to elucidate the mechanisms of new particle formation.

3.3 Results and Discussion

3.3.1 Geometrical analysis

The geometries of the precursors (e.g. H_2SO_4, H_2O, NH_3 and organic acids) were optimized at B3LYP/6-31G(d,p) level using the Gaussian 03 package [*Frisch et al.,*

2003]. The calculated structural parameters (e.g. bond length, bond angle) were found to be in good agreement with the available experimental data. For sulfuric acid, we adopted the trans conformation. Equilibrium structures of the precursors were then employed to construct the relevant complexes and search for their global minima by considering all possible orientations. The DFT-B3LYP has proven to be appropriate by considering the trade offs between the computational accuracy and efficiency due to heavy organic acids used in this study. Several possible stable configurations for the complexes between sulfuric acid, organic acids and ammonia were found; however we only report the most stable configuration with a hydrogen bond pair in the complex.

Figure 3.1 presents the optimized geometries of hydrogen bonded complexes at B3LYP/6-31G(d,p) level between sulfuric acid/ammonia and organic acids. A general feature of the investigated heteromolecular dimer complexes is that they possess a hydrogen bond pair which forms a 6- or 8-membered cyclic ring; the bonding strength of one hydrogen bond is stronger than that of the other. The hydrogen bonds of a trimer containing sulfuric acid, cis-pinonic acid, and/or water are characterized by the two hydrogen bond pairs connected by a molecule of sulfuric acid. The hydrogen bond (O-H•••X) (X = O or N) is in intermediate range between the electron-deficient hydrogen and the high electron density of oxygen or nitrogen. The bond length of the hydrogen bonds ranges from 1.496 Å to 1.724 Å for the stronger and from 1.708 Å to 2.383 Å for the weaker one of the pair as shown in Table 3.1. As indicated by the bond length, one of the hydrogen bonds is much stronger than the other in the sulfuric acid monohydrate (1.627 Å vs 2.094 Å). A similar characteristic feature was found in the sulfuric acid–

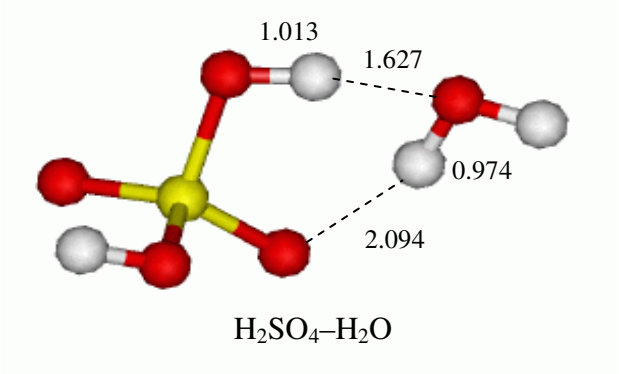

H_2SO_4–H_2O

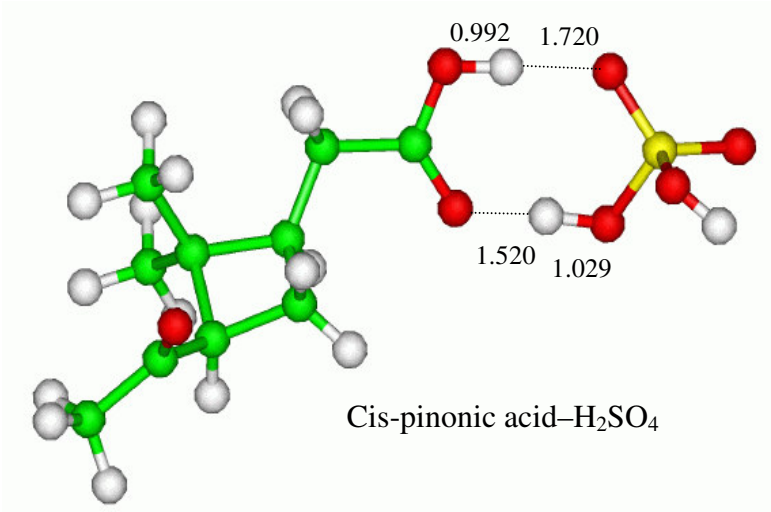

Cis-pinonic acid–H_2SO_4

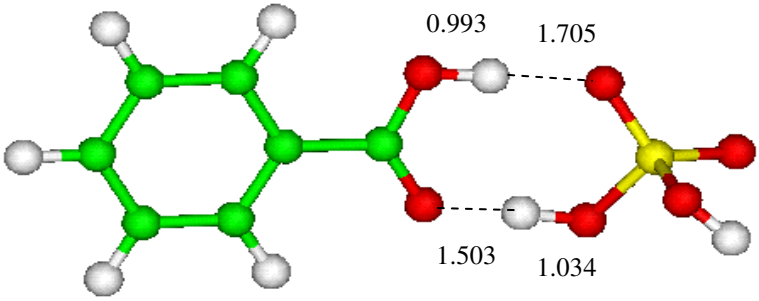

Benzoic acid–H_2SO_4

Figure 3.1. The optimized geometries of hydrogen bonded complexes at B3LYP/6-31G(d,p) level.

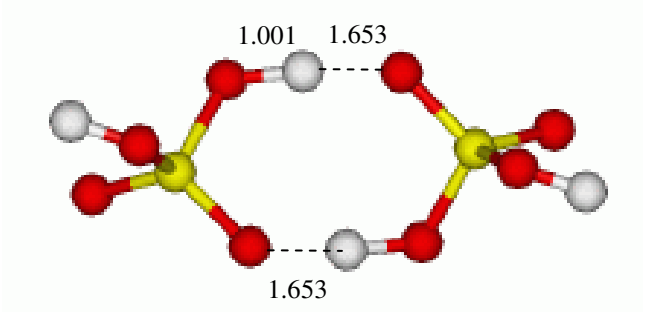

H_2SO_4 dimer

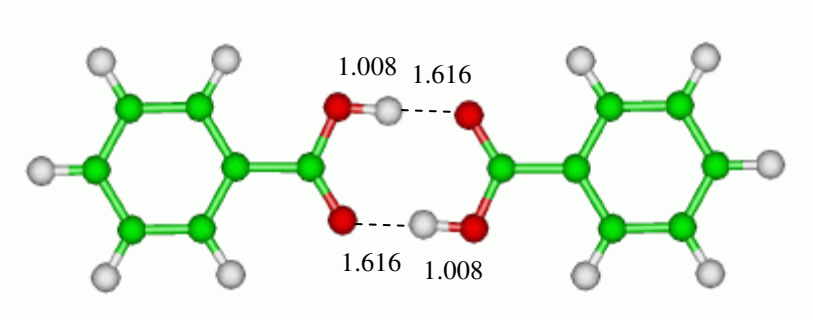

Benzoic acid dimer

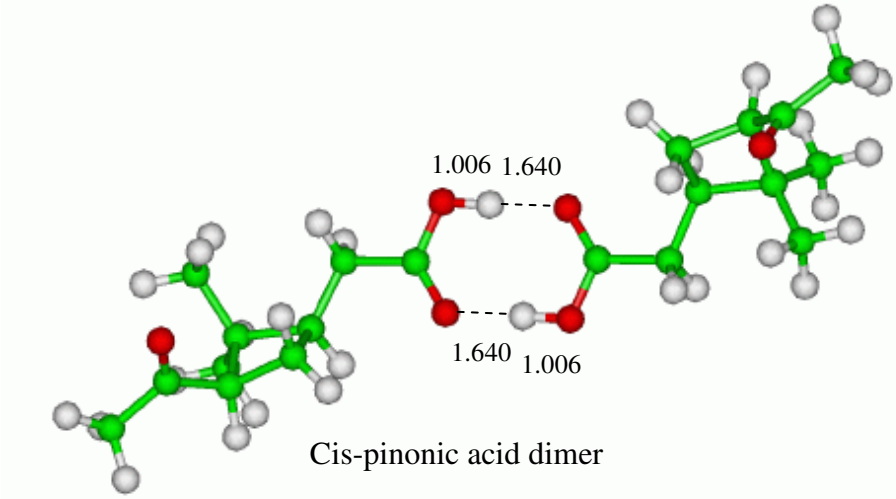

Cis-pinonic acid dimer

Figure 3.1. (continued)

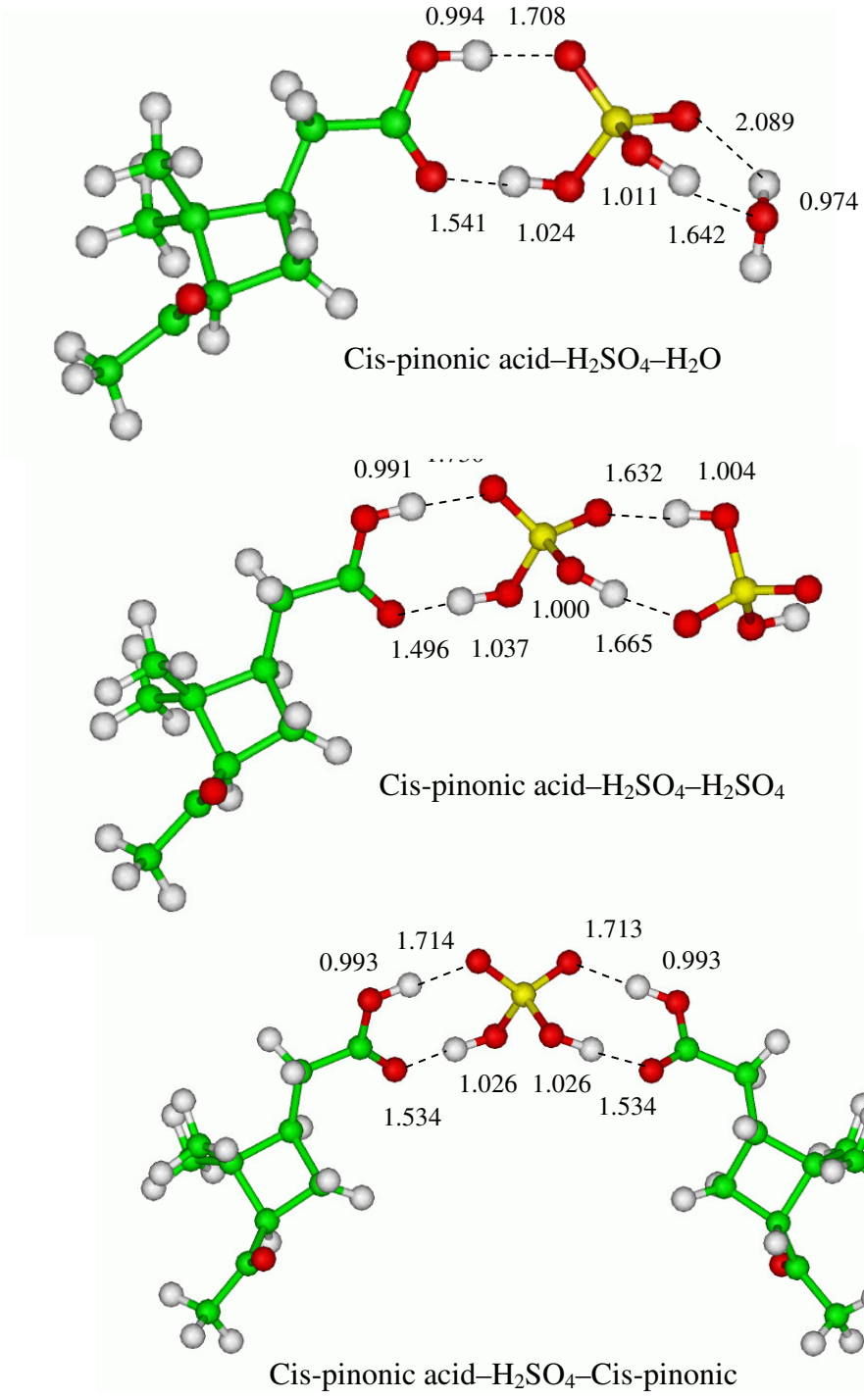

Figure 3.1. (continued)

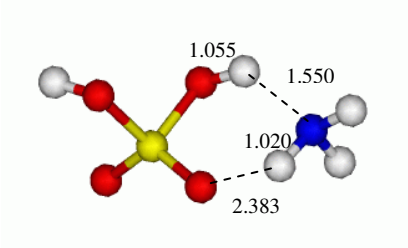

H_2SO_4–NH_3

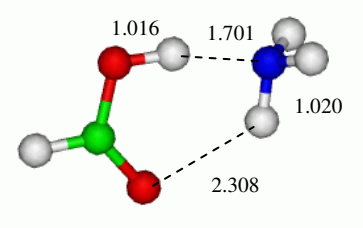

Formic acid–NH_3

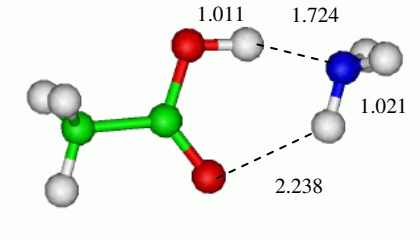

Acetic acid–NH_3

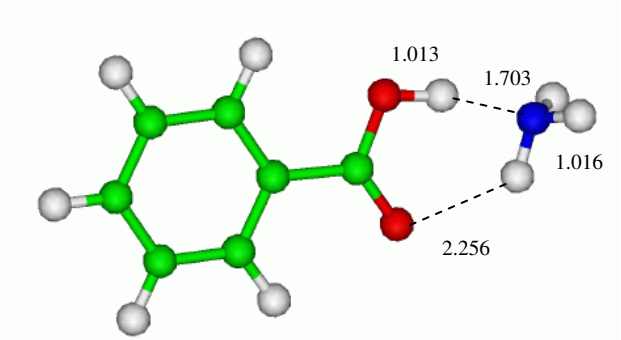

Benzoic acid–NH_3

Figure 3.1. (continued)

Table 3.1. Bond Length and Bond Angle of the Hydrogen Bonds in the Sulfuric Acid/Organic Acid/Ammonia/Water Complexes.

complex[a]	Hydrogen Bond 1[b]		Hydrogen Bond 2[c]	
	r(H···O(or N)	α(O-H···O or N)	r(H···O)	α(N or O-H···O)
W-SA	1.627	164.7	2.094	130.2
BA-SA	1.503	177.13	1.705	178.5
PA-SA	1.520	177.1	1.720	178.0
SA-SA	1.653	175.6	1.653	175.6
BA-BA	1.616	178.7	1.616	178.7
PA-PA	1.640	179.1	1.640	179.1
SA-AM	1.550	171.9	2.383	117.8
FA-AM	1.701	165.8	2.308	123.7
AA-AM	1.724	165.3	2.238	126.5
BA-AM	1.703	166.5	2.256	125.1
PA-SA-W	1.541	177.5	1.708	178.1
PA-SA-SA	1.496	178.1	1.730	178.3
PA-SA-PA	1.534	178.1	1.714	178.3
	Hydrogen Bond 3		Hydrogen Bond 4	
PA-SA-W	1.592	163.2	2.089	131.5
PA-SA-SA	1.632	178.3	1.665	178.1
PA-SA-PA	1.535	178.1	1.713	178.2

[a] W-SA: water-sulfuric acid complex; BA-SA: benzoic acid-sulfuric acid complex; PA-SA: cis-pinonic acid-sulfuric acid complex; SA-SA: sulfuric acid dimer; BA-BA: benzoic acid dimer; PA-PA: cis-pinonic acid dimer; PIA-NA: pinic acid-norpinic acid complex.
[b] Hydrogen bond with shorter bond length r(H···O) and α(O-H···O) is the bond angle.
[c] Hydrogen bond with longer bond length.

ammonia complex; the bond length (1.550 Å) of the hydrogen bond (O-H•••N) is substantially shorter than that (2.383 Å) of the hydrogen bond (N-H•••O), indicating sulfuric acid as the hydrogen donor, water and ammonia as the hydrogen acceptor in both sulfuric acid monohydrate and sulfuric acid–ammonia complexes. The hydrogen bonds in the organic acid–sulfuric acid complexes are comparable; one is slightly stronger than the other. For example, the stronger hydrogen bond has a bond length of 1.503 Å and 1.520 Å and the weaker hydrogen bond has a bond length of 1.705 Å and 1.720 Å for the benzoic acid–sulfuric acid and cis-pinonic acid–sulfuric acid complex, respectively. Since there is still one electron-deficient hydrogen atom left in the sulfuric acid side of the cis-pinonic acid–sulfuric acid complex, addition of water, sulfuric acid or even cis-pinonic acid is possible and results in the formation of a trimer, which generates another hydrogen bond pair, similar to the one mentioned above. The sulfuric acid molecule is located in the center of the trimer, shared by the two cyclic hydrogen-bonded rings. A pair of hydrogen-bonds with equivalent strength was formed in the homomolecular dimer of sulfuric acid, benzoic acid and cis-pinonic acid. The stronger hydrogen bond in the organic acid–ammonia complex (bond length: 1.70–1.72 Å) is weaker than the corresponding hydrogen bond in the sulfuric acid–ammonia complex. The bond length of the weaker hydrogen bond in the organic acid–ammonia complex ranges from 2.24 to 2.31 Å, indicating that the interactions between organic acids and ammonia is likely weaker than that between sulfuric acid and ammonia.

The interaction between organic acids and sulfuric acid involves a category of homonuclear hydrogen bonds (-O-H•••O=) where two oxygen are interconnected by a

system of π-conjugated double bonds, the so-called resonance-assisted hydrogen bonding (RAHB), which has been studied extensively over decades [*Kollman and Allen,* 1972; *Reed et al.,* 1988; *Curtiss and Blander,* 1988; *Gilli et al.,* 1994; *Fiacco et al.,* 2002; *Alabugin et al.,* 2003; *Gilli et al.,* 2006; *Pakiari and Eskandari,* 2006]. The contact distance between the two oxygen atoms in the hydrogen bond (-O-H•••O=) d(O---O) has been employed as an indicator of the hydrogen strength [*Gilli et al.,* 1994]. The distance d(O---O) < 2.5 Å is classified as very strong, 2.5 < d(O---O) <2.65 Å as strong, 2.65 < d(O---O) <2.80 Å as medium and d(O---O) > 2.8 Å as weak. As shown in Table 3.2, all the stronger hydrogen bonds of the pairs in the dimer and trimer fall into the strong hydrogen bond category as defined above with d(O---O) of 2.53–2.63 Å; all the weaker hydrogen bonds of the pairs in these complexes belong to the medium hydrogen bond with d(O---O) of 2.66–2.72 Å. Another characteristic feature of this category of hydrogen bonding is that the bond angles of the above mentioned hydrogen bonds α(-O-H···O=) are very close to 180˚ and hence the nuclei of the hydrogen bond (-O-H···O=) are nearly linear. One common feature in the organic acid–sulfuric acid complex is the formation of a hydrogen bond pair with one strong and one medium strength of hydrogen bonding, which bear both electrostatic and covalent interaction in nature. The heteronuclear hydrogen bonds (O-H•••N and N-H•••O), formed in the complexes of organic acids and ammonia, are weaker than those in organic acid–sulfuric acid complexes. The hydrogen bond pairs in these organic acid–ammonia complexes are medium and weak hydrogen bonding and essentially electrostatic in nature.

Table 3.2. Contact Distance d(O---O) of the Hydrogen Bond (-O-H•••O=) in the Organic Acid–Sulfuric Acid Complexes and Their Homomolecular Dimers.

Complex	HB pair 1		HB pair 2	
BA-SA	2.536	2.698		
PA-SA	2.549	2.712		
PA-SA-W	2.565	2.702	2.625	2.831
PA-SA-SA	2.532	2.720	2.635	2.660
PA-SA-PA	2.560	2.707	2.561	2.706
SA-SA	2.652	2.652		
BA-BA	2.624	2.624		
PA-PA	2.646	2.646		

Other structural modifications of the complexes upon formation of the hydrogen bonds can be evaluated from the lengthening or shortening of certain bonds around the hydrogen-bonded cyclic ring and the corresponding red shift or blue shift of the stretching frequencies from the precursor monomers. The hydrogen bonds (XO-H•••Y) (X = S or C and Y = O or N) or (Z-H•••O) (Z = N or O) in this study exhibit the lengthening or shorting of the O-H or N-H bond, which can be explained by the balance between hyperconjugation and rehybrization. The O-H and N-H bond lengthening and the S-OH bond shortening results in the red and blue shift of the corresponding stretching frequencies, respectively. For example, the O-H bond length in the cis-pinonic acid–sulfuric acid complex is increased by 0.02 and 0.06 Å for the stronger and the weaker hydrogen bond, respectively. Similarly, in the case of benzoic acid–ammonia complex, the O-H and N-H bond is elongated 0.04 and 0.01 Å, respectively. The hyperconjugative interaction (or charge transfer) from the lone pair of the hydrogen

bond acceptor to the antibonding σ*(O-H or N-H) orbital of the hydrogen bond donor leads to the lengthening of the O-H or N-H bond; while the increase in s-character of the O-H or N-H bond due to the decrease of the effective electronegativity of hydrogen upon the formation of hydrogen bond result in the shortening of the N-H or O-H bond [*Alabugin et al.,* 2003]. The calculated lengthening of the N-H or O-H is a result of the balance of these two effects, with the hyperconjugation dominant over the rehybridization for all hydrogen-bonded complexes studied here. The domination of charge transfer on the lengthening of the N-H and O-H bond has been reflected in the charge distribution around the cyclic hydrogen bond ring structure. For example, the Mulliken charges (taken from frequency calculations) of the hydrogen atoms in the hydrogen bond pair are increased from 0.359 of sulfuric acid and 0.321 of cis-pinonic acid to 0.415 and 0.380 of the cis-pinonic acid–sulfuric acid complex, indicating a decrease in the effective electronegativity of hydrogen upon the hydrogen bond formation. Similar increases in the Mulliken charges of the hydrogen atoms in the investigated hydrogen-bonded complexes were observed.

Another evidence of the geometrical change of the complexes upon the formation of the hydrogen bond is the red shift or blue shift of the stretching frequencies due to the lengthening or shortening of the corresponding bonds. Table 3.3 and 3.4 depict the stretching frequencies of sulfuric acid/organic acid/water complexes involving the red shift and blue shift and the corresponding frequencies of the monomers. For example, the lengthening of the SO-H, CO-H bonds in the cis-pinonic acid–sulfuric acid complex is 0.057 and 0.020 Å respectively, resulting in red shifts of the corresponding stretching

Table 3.3. The Calculated Stretching Frequencies of Dimers of Sulfuric Acid and Organic Acid and Their Monomers.

Assig.	SA	W	BA	PA	SA-SA	BA-BA	PA-PA
CO-H			3767	3751		3091	3146
C=O			1819	1841		1759	1779
SO-H	3761				3252		
S=O	1437				1402		
S-OH	847				913		
HO-H		3911					

Table 3.4. The Calculated Stretching Frequencies of Sulfuric Acid/Organic Acid/Water Complexes.

Assig.	SA-W	BA-SA	PA-SA	PA-SA-W	PA-SA-SA	PA-SA-PA
CO-H		3346	3360	3337	3384	3328
C=O		1717	1736	1740	1730	1736
SO-H	3005	2620	2695	3044(2775)*	3129(2579)*	2723
S=O	1169	1139	1140	1142	1254(1124)*	1279
S-OH	890	928	906	841	908(855)**	965
HO-H	3867			3865		

* Values in parentheses are the bond stretching frequencies in PA side
** Value in parentheses is the bond stretching frequencies in center SA

Table 3.5. The Calculated Stretching Frequencies of Organic Acid/Ammonia Complexes.

Assig.	AM	SA-AM	FA-AM	AA-AM	BA-AM
CO-H			2921	3010	2959
C=O			1806	1804	1776
N-H	3587	3598	3589	3617	3587
SO-H		2314			
S=O		1369			
S-OH		915			

frequencies of 1066 and 391 cm^{-1}, respectively. For the same complex, the S=O and C=O bond length also was increased by 0.019 and 0.023 Å, respectively, corresponding to a red shift of 295 and 105 cm^{-1}, respectively. The only blue shift of 59 cm^{-1} in the PA-SA complex was found for the S-OH bond, due to the shortening of ~ 0.052 Å for this bond. Table 3.5 shows a similar red shift of the stretching frequencies for N-H, CO-H and C=O bonds related to the hydrogen bonds of the organic acid–ammonia complexes. We also calculated the absorption intensities of the monomers and the hydrogen bonded complexes, and the distinct features of the corresponding IR spectra were obtained. Figure 3.2 shows the calculated IR spectrum of the sulfuric acid (top), cis-pinonic acid–sulfuric acid complex (middle) and the cis-pinonic acid. The most intense absorption peaks were found to be related to the vibrational stretching modes of the hydrogen bonds. The characteristic features of the calculated IR spectra of the organic acid–sulfuric acid complexes provide valuable information for the detection of these complexes in the atmosphere.

3.3.2 Thermochemical analysis

Relevant thermochemical parameters (e.g. binding energy, enthalpy, entropy and Gibbs free energy) for complex formation at 1 atm and 298K were calculated using various methods with different basis sets. Thermochemical analysis was performed following the procedures introduced by *Ochterski* [2000]. The energy and other thermochemical data were taken from the Gaussian calculations and the above-mentioned thermochemical properties were computed according to the following formula,

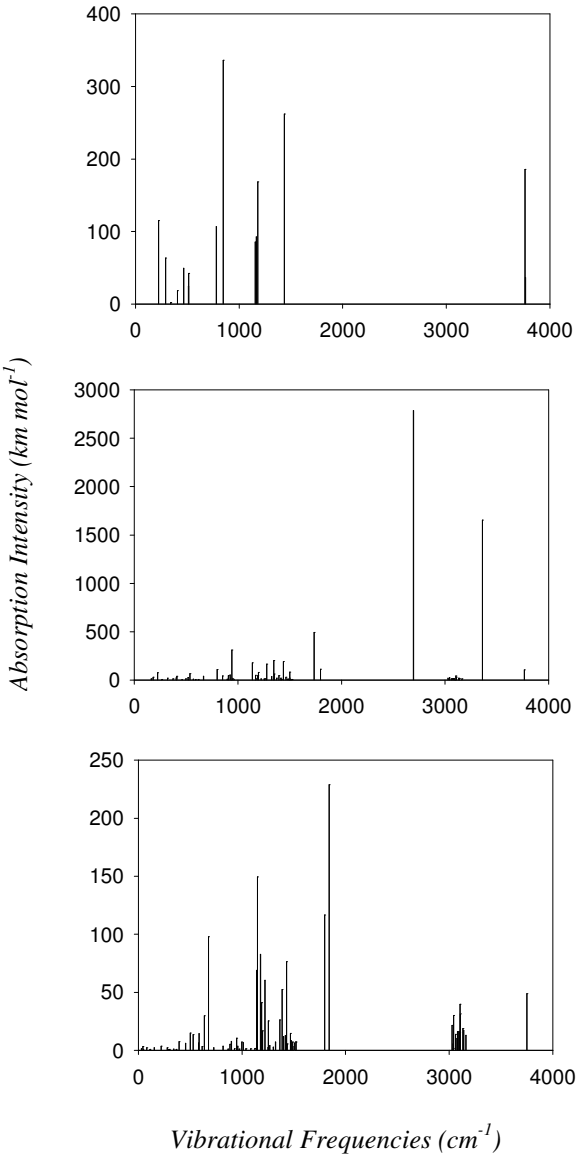

Figure 3.2. The calculated vibrational frequencies and the corresponding absorption intensities of cis-pinonic acid – sulfuric acid complex and its monomers.

$$\Delta_r E_B^o(298K) = \sum(\varepsilon_0 + ZPE)_{prod} - \sum(\varepsilon_0 + ZPE)_{react} \quad (3.1)$$

$$\Delta_r H^o(298K) = \sum(\varepsilon_0 + H_{corr})_{prod} - \sum(\varepsilon_0 + H_{corr})_{react} \quad (3.2)$$

$$\Delta_r G^o(298K) = \sum(\varepsilon_0 + G_{corr})_{prod} - \sum(\varepsilon_0 + G_{corr})_{react} \quad (3.3)$$

$$\Delta_r S^o(298K) = \frac{\Delta_r H^o(298K) - \Delta_r G^o(298K)}{298} \quad (3.4)$$

where $\Delta_r E_B^o(298K)$, $\Delta_r H^o(298K)$, $\Delta_r G^o(298K)$ and $\Delta_r S^o(298K)$ are binding energy, enthalpy, Gibbs free energy and entropy, respectively. ε_0, *ZPE*, H_{corr} and G_{corr} are total energy at 0K, zero-point energy correction, thermal correction to enthalpy and thermal correction to Gibbs free energy, respectively. Table 3.6–3.8 show the thermochemical parameters for the complex formation from the atmospheric nucleating precursors (e.g. sulfuric acid, organic acids, ammonia and water), computed using various methods with different basis sets at 298K and 1 atm. It can be seen that these thermochemical parameters are strongly dependent on the methods and basis sets. In general B3LYP/6-31G(d,p) level predicts the highest binding energies for the complex formation. Binding energies of ~20 kcal mol^{-1} were obtained for cis-pinonic acid–sulfuric acid and benzoic acid–sulfuric acid complexes, about 3–7 kcal mol^{-1} higher than those for organic acid–ammonia complexes at B3LYP/6-31G(d,p) level. Higher levels of theory (e.g. CCSD(T) and G2(MP2, SVP)) were also employed to calculate the binding energies of complex formation. Since the size of the cis-pinonic acid–sulfuric acid complex is very large, higher level calculations (e.g. QCISD(T) and CCSD(T) level) were prohibitive, and only binding energies at B3LYP and PW91PW91 levels are reported for this complex. The binding energies at the two highest levels (G2(MP2, SVP) and CCSD(T) + CF) are in

Table 3.6. Thermochemical Parameters for the Complex Formation at G2(MP2, SVP) Level.

molecule	MP2(full)/ 6-31G(d,p)				QCISD(T)/ 6-31G(d)			G2(MP2, SVP)		
	BE	ΔH	ΔS	ΔG	BE	ΔH	ΔG	BE	ΔH	ΔG
BA_SA	16.47	-16.16	-150.43	-5.48	18.63	-18.37	-7.62	17.84	-18.30	-7.55
BA_AM	8.43	-9.54	-132.79	-0.11	12.02	-13.00	-3.57	9.43	-10.41	-0.98
AA_AM	8.13	-8.50	-126.49	0.48	11.41	-11.55	-2.57	8.85	-8.99	-0.01
FA_AM	8.61	-9.12	-126.46	-0.15	11.63	-11.91	-2.93	9.18	-9.46	-0.48

Table 3.7. Thermochemical Parameters for the Complex Formation at CCSD(T) + CF Level.

complex	B3LYP/ 6-31G(d,p)				CCSD(T)/ 6-31G(d)			CCSD(T)+CF		
	BE	ΔH	ΔS	ΔG	BE	ΔH	ΔG	BE	ΔH	ΔG
BA_SA	19.85	-23.18	-202.88	-8.78	18.23	-21.56	-7.16	17.62	-20.95	-6.55
PA_SA	19.20	-19.17	-158.75	-7.90						
BA_AM	12.80	-16.63	-176.02	-4.08	12.08	-15.91	-3.36	9.27	-13.09	-0.54
AA_AM	15.34	-15.86	-128.64	-6.69	11.45	-11.97	-2.80	8.45	-8.97	0.20
FA_AM	13.08	-13.73	-127.97	-4.61	11.88	-12.53	-3.40	8.73	-9.38	-0.26

Table 3.8. Thermochemical Parameters for the Complex Formation at B3LYP and PW91PW91Level.

complex	B3LYP/ 6-31G(d,p)				B3LYP/ 6-311++G(2d,2p)			PW91PW91/ 6-311++G(2d,2p)		
	BE	ΔH	ΔS	ΔG	BE	ΔH	ΔG	BE	ΔH	ΔG
BA_SA_W	14.12	-14.92	-130.94	-5.59	8.14	-8.94	0.39	9.90	-10.71	-1.37
PA_SA_SA	17.16	-17.19	-149.27	-6.55	13.55	-13.58	-2.94	14.39	-14.43	-3.79
PA_SA_PA	19.03	-18.95	-156.94	-7.76						

good agreement with each other (within 0.6 kcal mol^{-1}) for all the complexes presented in Tables 3.6–3.7. Binding energies of ~17.6, 8.5–9.5 kcal mol^{-1} at G2(MP2, SVP) and CCSD(T) + CF levels were obtained for the benzoic acid–sulfuric acid, organic acid–ammonia complexes, respectively. We estimated binding energy of the same magnitude at both G2(MP2, SVP) and CCSD(T) + CF levels for cis-poninic acid–sulfuric acid complex. The higher binding energies for the organic acid–sulfuric acid than those for the organic acid–ammonia reflect the higher hydrogen bond strength in the former complexes than that in the latter complexes, which is consistent with the geometrical analysis and the topological analysis discussed in the next section. Binding energies of benzoic acid dimer and cis-pinonic acid dimer were found to be 19.5 and 18.4 kcal mol^{-1} respectively, in the same magnitude for the organic acid–sulfuric acid complexes; however, once they formed, no more hydrogen acceptor or donor was available for further growth via hydrogen bonding interactions. Hence homomolecular dimer formation contributes insignificantly to new particle formation. Addition of a third molecule (water, sulfuric acid or cis-pinonic acid) into the cis-pinonic acid–sulfuric acid can further stabilize the complex by ~13, 16, 18 kcal mol^{-1} at B3LYP/6-31G(d, p) level, respectively. We also carried out high levels of calculations and binding energy was found to be 8.1 (13.6) kcal mol^{-1} at B3LYP/6-311++G(2d, 2f) level for addition of a water (sulfuric acid) molecule to the PA_SA complex. The binding energies were found to be 9.9 and 14.4 kcal mol^{-1} at PW91PW91/6-311++G(2d, 2f) level respectively for addition of a water and sulfuric acid molecule to the PA_SA complex. The calculations for the PA-SA-PA complex in both B3LYP/6-311++G(2d,2f) and PW91PW91/6-

311++G(2d,2f) were found problematic and hence no binding energies at these two levels were reported for this complex.

The enthalpy of complex formation was also presented in Table 3.6–3.8 and values of the formation enthalpy were of the same magnitude (within 1 kcal mol^{-1}) as the corresponding binding energies for most of the complexes at various levels except for a few cases, for which the differences between binding energy and the formation enthalpy were found to be ~ 3 kcal mol^{-1} (e.g. BA_SA at B3LYP, CCSD(T) levels). The Gibbs free energies of complex formation were also strongly dependent on the methods and the basis sets. The B3LYP/6-31G(d,p) level predicted higher values of Gibbs free energies. For example, the Gibbs free energies for formation of BA_SA, PA_SA were -8.8, -7.9 kcal mol^{-1}, respectively, while the Gibbs free energies for organic acid–ammonia formation fall in the range of -4.1 ~ -6.7 kcal mol^{-1}. The Gibbs free energies for BA_SA at the two highest levels employed were -7.6 and -6.6 at G2(MP2,SVP) and CCSD(T)+CF level, respectively. However, for organic acid–ammonia complexes, the Gibbs free energies were much less, in the range of 0 ~ -1 kcal mol^{-1} at the same levels. The values of the Gibbs free energies for the organic acid–sulfuric acid complexes were estimated to be several kcal mol^{-1} higher than those for the organic acid–ammonia complexes at the same levels, indicating that the thermodynamic stabilities of the former were much higher than those of the latter. We also found the addition of a third molecule to the PA_SA complex can further stabilize the complex by lowering the Gibbs free energies by 5.6 ~ 7.8 at B3LYP/6-31G(d,p) level. Since the sizes of the organic acid–sulfuric acid complexes used in this study are large, the calculations are very expensive

and even prohibitive with current computation power and hence our thermochemical results for these complexes cannot be considered to be highly accurate. However, our main conclusions were still valid since they were mainly based on the relative differences rather than the absolute values of the Gibbs free energies, which were much less sensitive to the method and the basis sets employed.

3.3.3 Topological analysis

The bond length and binding energy can be used to evaluate the hydrogen bond strength, as discussed in previous sections. Topological properties (e.g. the electron density, Laplacian of the electron density and total energy density) of the hydrogen bonds provide alternative ways to study the hydrogen bond strength. According to *Bader's* theory [1990] of atoms in molecules, the nuclei are defined as the attractors of the gradient vector field of charge distribution, which denote as (3, -3) critical points and have maxima of charge density. An atom is thus viewed as the union of an attractor (nuclear) and its associated basin (electron density distribution). An interatomic surface is defined as the boundary of the basin of the atom that has zero gradient of charge density [*Bieglerkonig et al.,* 1982; *Bader et al.,* 1982]. All the gradient paths except two paths terminate at a point (denoting (3, -1) critical point) such that the Hessian matrix of the charge density at this point has two negative and one positive eigenvalues. The two paths originate from the bond critical point (3, -1) and terminate at neighboring attractors. These two paths form a line, the so-called bond path. A ring surface is defined as an infinite set of gradient paths which originate at a (3, +1) critical point where there are two positive and one negative eigenvalues of Hessian matrix of the charge density. In

contrast, the ring paths originate at the adjacent bond critical point and terminate at the ring critical points (3, +1) [*Bader,* 1990]. In this study, the electronic charge densities of the complexes and clusters were generated at the B3LYP/6-31G(d,p) level and the produced wave functions from DFT calculations were used as inputs of topological analysis. The bond and ring critical points of the electron densities of the complexes and clusters were then calculated and identified in the molecular graph as shown in Figure 3.3–3.4, along with the bond paths and the ring paths. The arrows indicate the bond critical points (BCP) of the hydrogen bonds. The topological feature of the complexes is that there exists a nearly planar, 6- or 8-membered cyclic ring structure with a pair of hydrogen bonds and for each hydrogen bond, the BCP lies closely to the H nuclei. The bond paths connect the atoms in the ring and the Poincare-Hopf relation [*Bader,* 1990] hold for the relationship among the number of nuclei (N), bond critical point (N_{bcp}), ring critical point (N_{rcp}) and cage critical point (N_{ccp}): $N-N_{bcp}+N_{rcp}-N_{ccp} = 1$. The length of the bond path is not necessarily equal to the equilibrium bond length due to the curvature effect. However, the curvature effect on the hydrogen bonds in this study is insignificant; the bond path length (BPL) is very close to the corresponding equilibrium bond length (Re), except for H_2SO_4–H_2O and H_2SO_4–NH_3 complexes, as shown in Table 3.9. The ratio of BPL/Re is as high as 1.077 in the case of H_2SO_4–NH_3 and the bond path is inwardly curved toward the H nuclear in the weaker hydrogen bond of the pair. We found that the ratio of the gradient path length from the BCP to O or N nuclear (r1) and from BCP to H (r2) in the hydrogen bond O(or N)•••H was correlated to the strength of the hydrogen bond. Figure 3.5 shows the ratio r1/r2 as a function of hydrogen bond path

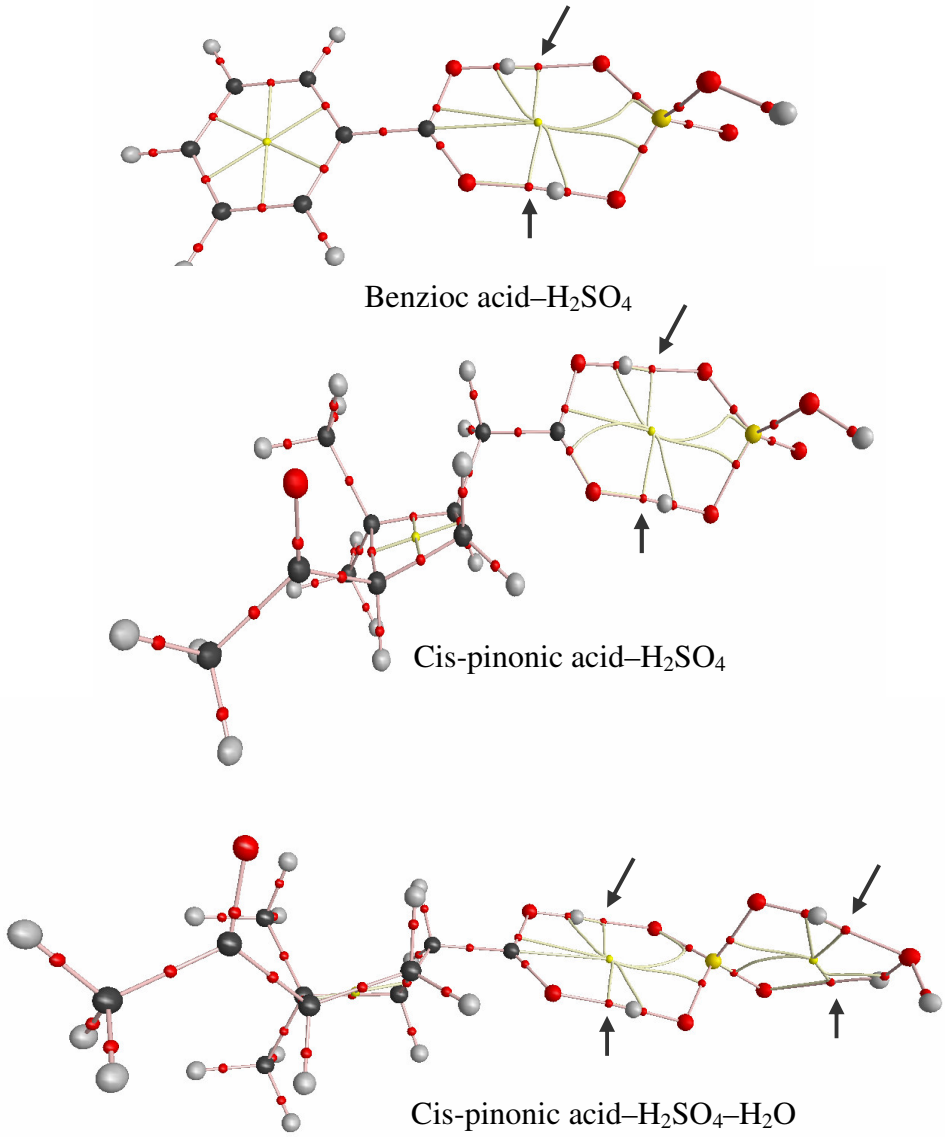

Figure 3.3. Molecular graphs of the organic acid–sulfuric acid complexes showing the BCPs, ring critical points, bond path and ring path.

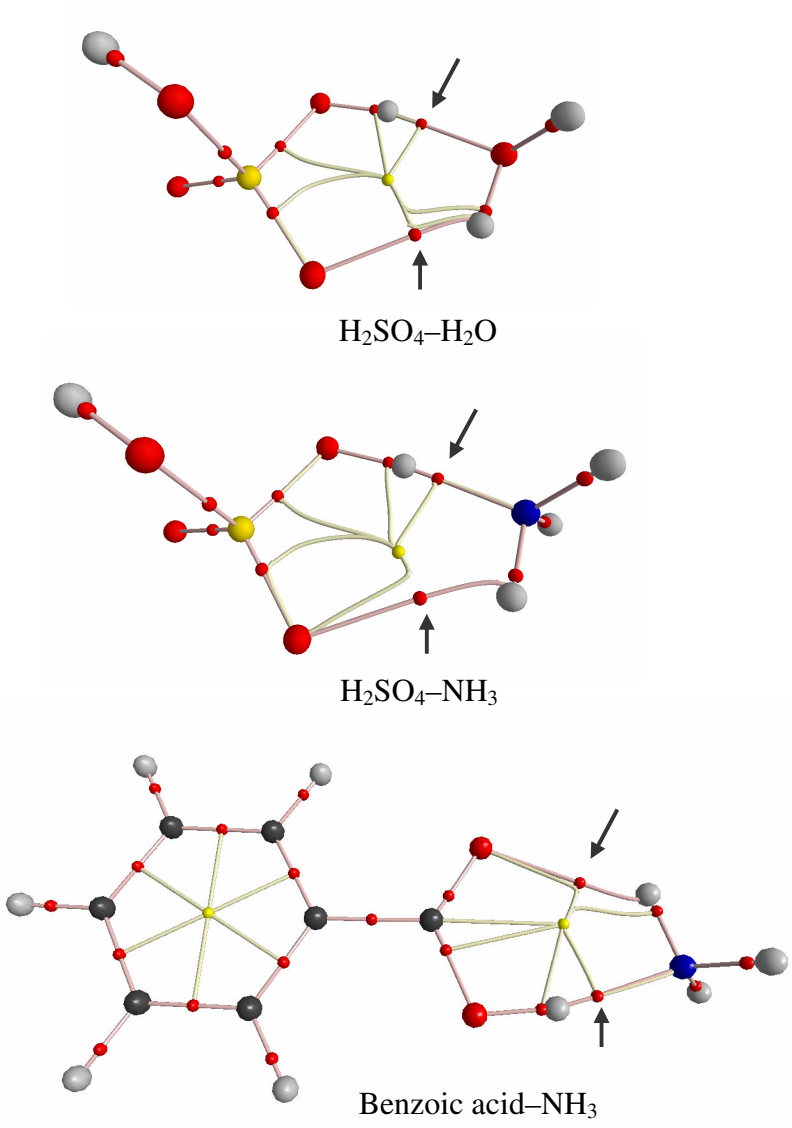

Figure 3.4. Molecular graphs of the sulfuric acid–water, sulfuric acid–ammonia and benzoic acid–ammonia complexes showing the BCPs, ring critical points, bond path and ring path.

length (and hence the equilibrium hydrogen bond length). The ratios range from 2.0 to 2.4 for the bond length of 1.50–1.72 Å and these ratios decrease to 1.5–1.6 when the hydrogen bond length is increased to 2.1–2.4. The figure also shows the shorter the bond path length the higher the ratio, indicating the stronger the hydrogen bonds the higher the ratio (r1/r2). The curvature of the bond path in the molecular graph reflects the deviation of the configuration of the molecular structure to its equilibrium configuration of minimum energy.

Topological parameters (e.g. charge density and its Laplacian, the electronic kinetic, potential and total energies) at the bond critical points (BCPs) can be employed to evaluate the nature of hydrogen bonding interactions in the complexes. *Koch and Popelier* [1995] proposed eight topological criteria based on the theory of atoms in molecules to characterize the types of the hydrogen bonds. The closed-shell interactions (e.g. ionic bonds, hydrogen bonds and van der Waals interactions) correspond to positive value of Laplacian of charge density at BCP, whereas for covalent bonds the Laplacian has negative value. The strength of the hydrogen bonds correlates with the charge density and in general the larger the value of the charge density, the stronger the hydrogen bond. The accumulation of the charge in the bonding region results in a decrease of the curvature of the charge density along the internuclear axis, providing an explanation of minor curvature of the strong hydrogen bonding as mentioned above. Two quantitative criteria were suggested to characterize a hydrogen bond: the charge density and its Laplacian, in the range of 0.002–0.035 au and 0.024–0.139 au respectively [*Popelier,* 1998]. As shown in Table 3.10, the value of charge density of the

Table 3.9. Comparison of the Equilibrium Bond Length and the Bond Path Length of the Complexes.

Species	Hydrogen bond 1					Hydrogen bond 2				
	Re	r1(Å)[a]	r2(Å)[a]	r1/r2	BPL	Re	r1(Å)	r2(Å)	r1/r2	BPL
SA-W	1.627	1.112	0.516	2.155	1.628	2.094	1.304	0.802	1.625	2.106
SA-AM	1.55	1.092	0.457	2.390	1.549	2.238	1.426	0.985	1.448	2.411
SA-SA	1.653	1.112	0.542	2.052	1.654					
BA-BA	1.617	1.101	0.516	2.136	1.617					
PA-PA	1.641	1.113	0.528	2.106	1.641					
BA-SA	1.503	1.047	0.457	2.290	1.504	1.705	1.139	0.568	2.006	1.707
PA-SA	1.52	1.055	0.466	2.263	1.521	1.72	1.146	0.576	1.989	1.722
AA-AM	1.724	1.179	0.545	2.163	1.724	2.238	1.368	0.878	1.559	2.246
BA-AM	1.703	1.169	0.534	2.188	1.703	2.256	1.376	0.890	1.545	2.266
FA-AM	1.701	1.168	0.533	2.189	1.701	2.308	1.400	0.918	1.525	2.318

[a] r1, r2 is the length of gradient path from bond critical point (BCP) to O or N nuclear and from BCP to H nuclear, respectively.

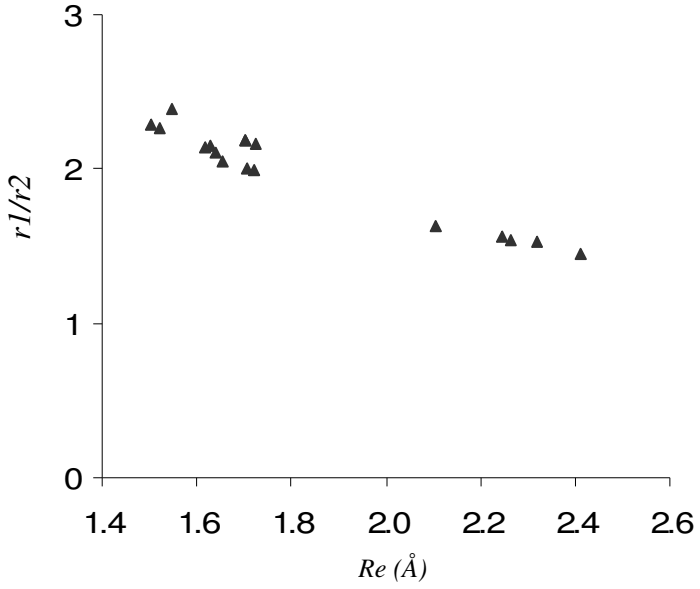

Figure 3.5. Plot of r1/r2 as a function of equilibrium bond length.

stronger hydrogen bond of the pair in this study ranges from 0.046 to 0.080 au and these values exceed the upper value of charge density proposed by *Koch and Popelier* [1995]. Similarly, the Laplacian of charge density of the complexes composed of sulfuric acid, organic acid and water is in the range of 0.14–0.16 au, higher than the upper value of the Laplcian criteria. The high values of charge density and Laplican strongly indicate that the hydrogen bonding interaction between sulfuric acid and organic acids is quite strong, consistent with the above-mentioned geometrical characterization of covalent bonding in nature for the stronger hydrogen bond of the pair. For the organic acid– sulfuric acid complexes, the weaker hydrogen bond of the pair can be classified as medium strength as mentioned in the geometrical analysis, which can be seen from the values of the charge density and the Laplacian, in the range of 0.039–0.045 au and 0.12–0.14 au respectively. However, for sulfuric acid mono hydrate and ammonia–sulfuric acid (or organic acids) complexes, the hydrogen bond pair in these complexes is only in medium to low strength due to a generally-lower values of both charge density and Laplacian of these hydrogen bonds at BCPs, which is also consistent with those from geometrical analysis. The bond ellipticity ($\epsilon = \lambda_1/\lambda_2-1$) ($\lambda_1$, $\lambda 2$ are the first two eigenvalues of the Hessian matrix) of the Hessian matrix provides another measure of not only charge accumulation in a given plane but also its structural stability. Substantial bond ellipticities mean structural instability and in other words, the bonding interaction is not strong and easily broken. We found the bond elliticities of the medium to weak hydrogen bonds are substantially greater than those of the strong hydrogen bonds in this study.

Table 3.10. Topological Parameters (Charge Densities, Laplacian, Kinetic Energy Densities, Potential Energy Densities and Total Energy Densities) at BCPs of the Hydrogen Bonds of the Complexes. (unit in au)

Species	Hydrogen bond 1					Hydrogen bond 2				
	ρ (-2)	$\nabla^2\rho$ (-2)	G(r) (-2)	V(r) (-2)	K(r) (-2)	ρ (-2)	$\nabla^2\rho$ (-2)	G(r) (-2)	V(r) (-2)	K(r) (-2)
SA-W	5.53	14.44	4.02	-4.43	-0.41	2.02	6.37	1.63	-1.66	-0.03
	4.64	12.11	3.49	-3.95	-0.46	1.48	5.43	1.20	-1.04	0.16
SA-AM	7.96	8.88	4.65	-7.08	-2.43	1.24	4.46	1.02	-0.93	0.09
SA-SA	4.58	14.07	3.51	-3.50	0.01					
BA-BA	5.42	14.77	3.98	-4.28	-0.29					
PA-PA	5.11	14.16	3.73	-3.93	-0.19					
BA-SA	7.20	15.61	5.31	-6.72	-1.41	4.09	12.64	3.10	-3.04	0.06
PA-SA	6.87	15.71	5.07	-6.21	-1.14	3.96	12.19	2.98	-2.92	0.06
AA-AM	5.13	10.72	3.20	-3.71	-0.52	1.67	5.20	1.29	-1.28	0.01
BA-AM	5.38	10.95	3.35	-3.96	-0.61	1.61	5.12	1.26	-1.23	0.02
FA-AM	5.44	10.89	3.37	-4.01	-0.65	1.46	4.75	1.14	-1.10	0.04
PA-SA-W	6.49	15.73	4.80	-5.67	-0.87	4.08	12.52	3.08	-3.02	0.05
PA-SA-SA	7.35	15.36	5.38	-6.93	-1.54	3.87	11.91	2.91	-2.85	0.06
PA-SA-PA	6.63	15.66	4.88	-5.85	-0.97	4.03	12.37	3.04	-2.99	0.05
	Hydrogen bond 3					Hydrogen bond 4				
PA-SA-W	5.35	14.14	3.89	-4.24	-0.35	2.04	6.35	1.63	-1.67	-0.04
PA-SA-SA	4.87	14.60	3.72	-3.80	-0.08	4.47	13.72	3.41	-3.40	0.02
PA-SA-PA	6.60	15.73	4.87	-5.81	-0.94	4.04	12.37	3.04	-2.99	0.05

The electronic energy density K(r) can be used to characterize the bonding strength of the hydrogen bonds, and K(r) is related to the Laplacian of the charge density by a local expression of the virial theorem [*Bader,* 1990],

$$\left(\frac{\hbar}{4m}\right)\nabla^2\rho(r) = K(r) + G(r) \tag{3.5}$$

where $K(r) = G(r) + V(r)$, G(r) is the electronic kinetic energy density, which is always positive and V(r) is the electronic potential energy density, which is always negative. m, $\hbar$ is the mass of an electron and the Planck constant respectively. As

discussed above, a positive Laplacian at a BCP indicates that the hydrogen bonding interaction is dominated by the contraction of the charge away from the interatomic surface toward each nuclear and hence depletion of the charge along the bond path. For the hydrogen bonding interactions in this study, the Laplacian is found to be positive, indicating that the electronic kinetic energy density is in local excess over the magnitude of the corresponding total electronic energy density in the virial theorem, $G(r)>|K(r)|$ (or $2G(r)>|V(r)|$). In addition, for strong hydrogen bonding interaction, the total electronic energy density K(r) was found to be negative, showing partially covalent and partially electrostatic in nature; whereas this quantity was positive for medium and weak hydrogen bonds, revealing only electrostatic interactions for this bonding. As shown in Table 3.10, the electronic energy density of the hydrogen bond 1 and 3 is all negative except for that of the dimer of sulfuric acid, and the values of the K(r) of the sulfuric acid–organic acid complexes at BCPs is generally higher than those of the organic acid–ammonia complexes, indicating again the hydrogen bonding of the former is much strong than the latter. Interestingly, the electronic energy densities of the SA-AM were found to be the highest and no explanation can be given. For hydrogen bond 2 and 4, however, the electronic energy densities of these hydrogen bonds at BCPs were all positive or small negative, revealing weaker interactions for these hydrogen bonds.

3.3.4 Molecular dynamics simulations of clusters

Molecular dynamic simulation provides a useful tool to explore the time dependent behavior of a molecular system at the microscopic level and it provides detailed information on the fluctuation and conformation changes of the molecular

system at an accessible time scale [*Rapaport,* 2004]. The microscopic information obtained by molecular dynamic simulation was employed to study the macroscopic thermodynamic properties of the system via statistical mechanics. It is extremely useful when the system cannot be investigated by the current experimental techniques. The molecular dynamic simulation was based on the classic Newton's equation of motion, **F = ma,** where **F** is the force exerted on each particle (a particle can be an atom or a molecule), **m** is the mass of the particle and **a** is its acceleration. Solving this equation of motion iteratively for each particle generated a trajectory, which described the kinetic parameters of the system (e.g. position, velocity and acceleration) as a function of time; that is the time evolution of the system. Since the force **F** can be expressed as the gradient of the potential energy, if the potential energy function describing the interactions between particles is known, the trajectory of the system can then be determined. The form of the potential energy surface is usually very complicated and a force field is needed to analytically describe the energy of the molecular system in terms of the coordinates of all its atoms in molecules. The energy of the molecular system can be generally broken down into bond interaction and non-bond interaction energy, both of which are composed of several components,

$$E(r^N) = E_{stretching} + E_{bending} + E_{torsion} + E_{cross} + E_{vdW} + E_{electrostatic} + E_{polarization} \qquad (3.6)$$

where the first four terms in the right hand side of the expression equation are the intramolecular bond interaction terms (e.g. the bond stretching, valence angle bending, valence torsion and inversion, and cross terms) and the last three terms are the non-bond intermolecular interaction terms (e.g. the van der Waals interactions, electrostatic

interactions and interactions induced by polarization). The force field used in this study is the second-generation consistent force field (CFF), whose parameters are determined from quantum mechanical calculations of the potential energy surfaces. CFF force fields contain 11 types of intramolecular energy terms including bond stretching, valence angle bending, valence torsion and inversion (valence dihedral angles and out of plane deformation), cross terms (bond-bond, bond-angle, angle-angle, angle-angle-torsion, angle-torsion, central bond-torsion and terminal bond torsion) and 2 types of intermolecular terms including electrostatic interactions and the van der Waals interactions. The accuracy of the CFF force has been validated for several common classes of molecules by comparing the CFF-calculated parameters (e.g. bond length, bond angle, vibrational frequencies and bonding energies) with the results from experiments.

We performed molecular dynamic simulations using the Cerius^2 Open Force Field module (OFF) with the CFF1.02 force field (Accelrys Inc). We prepared the molecular clusters using the Cerius^2 amorphous builder and set up a unit cubic cell with 100 nm in dimension using the crystal builder. The cluster with fixed composition was put into the center of the cube with periodic boundary for energy minimization to ensure the stability and minimum potential energy of the model cluster. The minimization was performed using Newton-Raphson algorithms, available in the OFF simulation engine. The minimization process was found to be efficient and was typically converged in a single minimization run within a reasonable computational time (within 30 min). It should be pointed out that since CFF force field fully accounts for hydrogen bonds in the

function expression, explicit specification was not required for the clusters with ample hydrogen bonds in this study. For non-bond interactions (e.g. electrostatic and van der Waals interactions), certain approximation is often employed to reduce the computational expense. In this case, a cut-off method was applied to the periodic system in the OFF module. Non-bond interactions were simply calculated to a cut-off distance and interactions beyond this distance were ignored. A cut-off distance of 44 nm was used in balance of calculation accuracy and computational expense. The dynamic simulation was performed using the Verlet leapfrog integrator under fixed composition, isobaric and isothermic (NPT) thermodynamic ensemble with periodic boundary condition. The external pressure of the system is set to zero. The size and the shape of the unit cell were allowed to vary to accommodate the adjustment of the pressure (kept at 1 atm) and the temperature was controlled by the T-Damping method. An integration timestep of 1 fs was used to ensure the stability and accuracy in the integration process and the number of 3×10^7 steps was carried out so that a total simulation time of ~30 ns was obtained, long enough to capture sufficient representative conformations.

We construct a cluster with 4 sulfuric acid, 1 cis-pinonic acid and 10 water using the Cerius[2] program suite to perform molecular dynamic simulations under the above mentioned conditions. One interesting feature of the cluster during the simulation was that the cis-pinonic acid was always to one side of the cluster, while the sulfuric acid and water was in the other side and their interactions were via hydrogen bonding and van de Waal force. As shown in Figure 3.6, the dimension of the cluster was estimated to be ~1.4 nm, consistent with the assumed critical size (~1 nm). Figure 3.7 shows the total

energy, kinetic energy and potential energy (in kcal) for a typical simulation run. The cluster achieved equilibration at ~5 ns and all the energies remain almost constant after that until it experienced a sudden conformational change as indicated by the sudden change of the energies at 20 ns. Figure 3.8 depicts the trajectory of the cell parameters (a, b, c) for the same run and similar change in cell parameters can be seen at 20 ns.

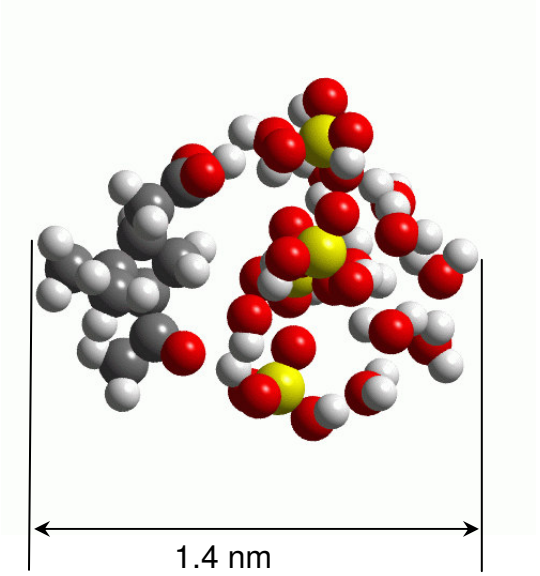

Figure 3.6. The shape and size of a cluster composed of 1 cis-pinonic acid, 4 sulfuric acid and 10 water.

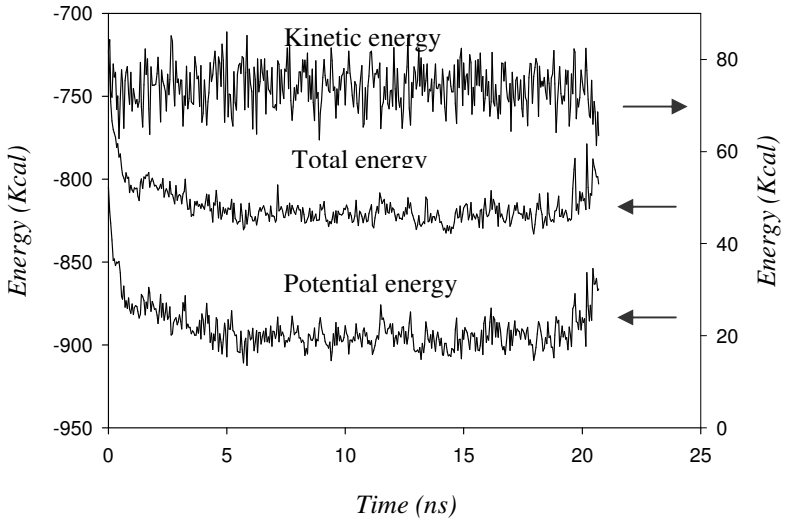

Figure 3.7. Fluctuation of the total energy, kinetic energy and potential energy during a typical simulation run.

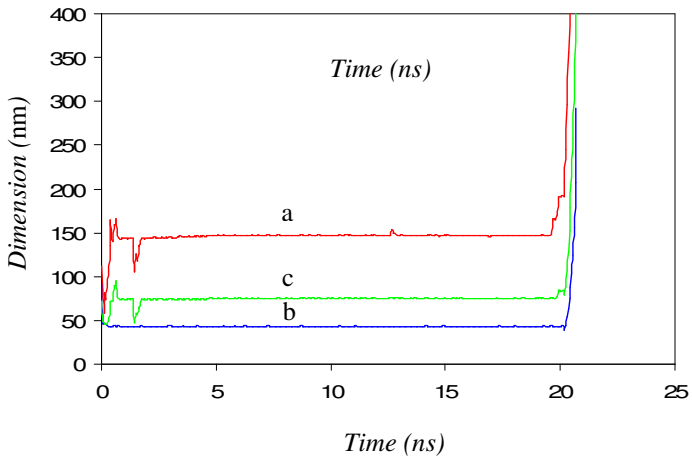

Figure 3.8. Fluctuation of the cell parameters (a, b, c) during the same simulation run.

3.4 Summary

Formation of molecular complexes and clusters of atmospheric aerosol nucleating precursors were investigated by theoretical methods. We performed quantum chemical calculations to explore the structures and energetics of complexes from sulfuric acid, organic acid, ammonia and water. Geometrical analysis shows that organic acid–sulfuric acid complexes bear a hydrogen bond pair with one strong and one medium strength of hydrogen bonding, while for organic acid–ammonia complexes, the hydrogen bond pair is much weaker. The binding energies for organic acid–sulfuric acid complexes are also higher than those for organic acid–ammonia complexes by several kcal mol^{-1}. Topological analysis employing quantum theory of atoms in molecules (QTAIM) shows that the charge density at BCPs of the hydrogen bonds of the organic acid–sulfuric acid are positive and falls in the range or exceeds the range of one strong and one medium hydrogen bonding criteria. Similar conclusions can be drawn according to the analysis of the Laplacian and energy density. Molecular dynamic simulations predicted a cluster of 1.4 nm in dimension with a composition of 1 cis-pinonic acid, 4 sulfuric acid and 10 water molecules. This study provides the geometrical, energetical and topological information of hydrogen-bonding interactions in the atmospheric complexes and helps to elucidate the structure, size, composition and other properties of atmospheric clusters.

CHAPTER IV

LABORATORY INVESTIGATION OF HETEROGENEOUS INTERACTIONS OF ATMOSPHERIC CARBONYLS AND SULFURIC ACID: IMPLICATIONS FOR SECONDARY ORGANIC AEROSOL FORMATION*

4.1 Introduction

Carbonyl compounds represent a significant amount of trace gaseous species in the troposphere. Atmospheric sources of carbonyls include anthropogenic and biogenic emission or products formed from photochemical oxidation of volatile organic compounds (VOCs) [*Seinfeld and Pandis,* 1998; *Finlayson-Pitts and Pitts,* 2000]. Concentrations of low molecular carbonyls (e.g. formaldehyde, acetaldehyde and acetone) were found to be as high as several μg m^{-3} in polluted air [*Granby et al.,* 1997; *Cardenas et al.,* 2000; *Wert et al.,* 2003]. High molecular weight aldehydes (e.g. octanal and 2, 4-hexadienal used in this study) emitted to the atmosphere from vegetation as a result of leaf wounding or from commercial cooking facility have been detected in numerous field studies [*Takeoka et al.,* 1996; *Ho et al.,* 2006]. One important prototype of dicarbonyl used in this study, methylgloxal (CH_3COCHO) has been measured to be 50 ppt to 2 ppbv in urban area and 3–120 μM in cloud droplet [*Grosjean et al.,* 1990; *Munger et al.,* 1995]. It is produced from photochemical oxidation of volatile organic compounds (VOCs) in the atmosphere. Oxidation of anthropogenic aromatics (toluene,

* Reproduced with permission of American Geophysical Union from Heterogeneous chemistry of octanal and 2, 4-hexadienal with sulfuric acid, Zhao, J., N.P. Levitt and R. Y. Zhang, 2004, *Geophysics Research Letters,* 32, Art. No. L09802. Copyright 2004 American Geophysical Union; and with permission of American Chemical Society from Heterogeneous Reactions of Methylglyoxal in Acidic Media: Implication for Secondary Organic Aerosol Formation, Zhao, J., R. Y. Zhang, N.P. Levitt, and J. Chen, 2006, *Environment Science & Technology*, 40, 7682-7687. Copyright 2006 American Chemical Society.

xylenes, or trimethylbenzenes) and biogenic isoprene leads to significant production of methylglyoxal in the urban and regional atmospheres [*Suh et al.,* 2002, 2003, 2006; *Zhao et al.,* 2005; *Fan and Zhang,* 2006]. For example, the molar molecular yield of methylglyoxal is about 90% from 1, 3, 5-trimethylbenzene oxidation and 0.16 from toluene oxidation [*Kalberer et al.,* 2004].

Organic aerosol has received considerable attention in recent years because atmospheric aerosol consists of a significant fraction (as high as 90%) of organic material. Organic aerosol emitted directly from various sources (e.g. combustion, biomass burning) is referred to primary organic aerosol (POA). Semi- and non-volatile organic compounds produced from photo-oxidation of volatile organic compounds (VOCs) have sufficiently low vapor pressure to undergo gas-to-particle conversion, leading to the formation of secondary organic aerosol (SOA) [*Kanakidou et al.,* 2005]. These low volatile compounds can also partition themselves between the gas and aerosol phase, increasing the organic fraction of the total aerosol mass. However, the interactions between low and medium molecular weight carbonyls and aerosol particles generally invoke little attention due to relatively high volatility. Meanwhile it is important to understand heterogeneous processes involving in carbonyls that influence their abundance and roles in the formation of secondary organic aerosols. Recent chamber experiments [*Jang et al.,* 2002; *Kalberer et al.,* 2004] have shown that heterogeneous acid-catalyzed reactions including hydration, polymerization, hemiacetal/acetal formation, aldol condensation or cationic rearrangement result in the formation of low volatile products which increase the amount of SOA mass. *Jang et al.*

[2002] performed chamber experiments to study heterogeneous aerosol-phase reactions of a series of aldehydes (e.g. glyoxal, hexanal, octanal, decanal, 2, 4-hexaldienal) with and without an acid catalyst. They found that the organic aerosol mass yields increase up to multifold in the presence of the acid catalyst. *Tolocka et al.* [2004] presented an experimental studies on the detection of oligomers from ozonolysis of alpha-pinene in the presence of acid seed aerosol. They tentatively attributed the oligomer formation to aldol condensations and gem-diol reactions. Reaction chamber experiment of *Kalberer et al.* [2004] showed that a substantial fraction (~ 50%) of the organic aerosol mass is composed of polymers and the polymerization results from reactions of carbonyls (e.g. methylglyoxal) and their hydrates formed from photooxidation of aromatic compounds. In contrast to the experiments of *Jang et al.* [2002], polymerization proceeds without any preexisting acid seed particles. The authors speculated that acids formed in the photooxidation are present in sufficiently high concentration to catalyze polymerization reactions. *Gao et al.* [2004] performed Teflon chamber experiment to examine the presence of oligomers in SOA from hydrocarbon ozonolysis. Oligomers were found to be formed both with and without seed particles and organic acids produced from photooxidation of hydrocarbons provide necessary acidity for acid-catalyzed reactions, consistent with the results by *Kalberer et al.* [2004]. Evidence of oligomer formation in evaporating aqueous glyoxal and methylglyoxal solutions was presented by *Loeffler et al.* [2006] and acids were found to have little effect on glyoxal oligomer formation. *Kroll et al.* [2005] presented chamber studies of the reactive uptake of simple carbonyls (e.g. octanal, 2, 4-hexadienal, glyoxal, methylglyoxal, 2, 4-pentanedione) onto inorganic

aerosols and no growth was observed for most carbonyls studied except for glyoxal and uptake of glyoxal does not depend on the particle acidity but rather on ionic strength of the seed. *Liggio et al.* [2005a, b] performed similar chamber study to investigate heterogeneous reactions of glyoxal on particulate matter and they have identified formation of low volatile acetals and sulfate esters in the aerosol phase. *Surratt et al.* [2007] have identified organosulfate esters from photooxidation of alpha-pinene and isoprene. Sulfate esters are found to account for a larger fraction of organic mass with increased acidity of the seed particles. The reactive uptake of pinonaldehyde on aerosols has been studied in a reaction chamber and the results showed that oligomerization of pinonaldehyde occurred under acidic conditions. Uptake coefficients of pinonaldehyde were in the range of 1.2×10^{-5}–1.3×10^{-3} and were primarily dependent upon aerosol water activity and acidity but independent of gas phase pinonaldehyde concentrations, indicating that the heterogeneous reactions of pinonaldehyde are of little importance as a gas phase loss mechanism but potentially of major importance as a source of secondary organic aerosols (SOA) [*Liggio and Li,* 2006]. Uptake of gas-phase hexanal on aerosols has been investigated and the acidic aerosols took up substantial amounts of organic material and the acid-catalyzed products has been identified as aldol condensation (2-butyl 2-octenal) and hemiacetal products, depending on the initial acid concentration of the aerosol, suggesting these reactions may impact aerosol optical properties as well as aerosol composition [*Garland et al.,* 2006]. Direct investigations of heterogeneous transformation of carbonyl compounds in sulfuric acid solution have been subjects of numerous studies. The uptake of formaldehyde [*Jayne et al.,* 1996; *Iraci and Tolbert,*

1997], acetone [e.g., *Duncan et al.,* 1998; *Kane et al.,* 1999; *Klassen et al.,* 1999], and acetaldehyde [*Michelsen et al.,* 2004] by aqueous sulfuric acid solutions has been studied at low temperatures. A recent study investigated transformation of 2, 4-pentanedione on H_2SO_4 and found aldol condensation at acidities as low as 20 wt % [*Nozière and Riemer,* 2003].

In this study, we perform direct uptake measurements of carbonyls on sulfuric acid solution. We chose larger aldehydes such as octanal and 2, 4-hexadienal and smaller dicarbonyl such as methylglyoxal as model carbonyls and monitored the gaseous carbonyls using ID–CIMS. Uptake coefficients and effective Henry's law constants were obtained from this study. Our results elucidate the distinctive reaction mechanisms for larger aldehydes and smaller dicarbonyls with sulfuric acid.

4.2 Experimental Methodology

The experiments were carried out in a flow reactor coupled to an ion drift–chemical ionization mass spectrometer (ID–CIMS) as shown in Figure 4.1 and more details of ID–CIMS can be found in Chapter II. Briefly, the Pyrex reactor was 50 cm long and with an internal radius of 1.25 cm. Liquid H_2SO_4 was placed within an inner Pyrex vessel, which was recessed to form a trough (2.0 cm wide and 0.7 cm deep) to hold the liquid solution. The geometric area of sulfuric acid was calculated from the dimension of the Pyrex vessel, which was ~ 40 cm^2. The temperature of the flow reactor was controlled by flowing cold methanol through the outer jacket of the reactor and was measured by a thermocouple. All carrier flows were monitored with calibrated electronic mass flow meters (Millipore Tylan 260 Series). The flow reactor was operated under the

laminar flow conditions with a pressure of ~ 1 Torr and flow velocities of 800–1000 cm sec^{-1}. Typical flow rate was 0.30–0.35 slpm. Helium was used as the main carrier gas. H_2SO_4 solutions were prepared by dilution of 96 wt % H_2SO_4 with de-ionized water. The acid reservoir was changed and the composition of the acid was checked before and after each experiment. The acid compositions were verified by density measurements and by titration with standardized NaOH. During the experiment water vapor was added to the flow reactor to reduce H_2O evaporation from the liquid and to minimize changes in the acid composition [*Zhang et al.,* 1993a, b].

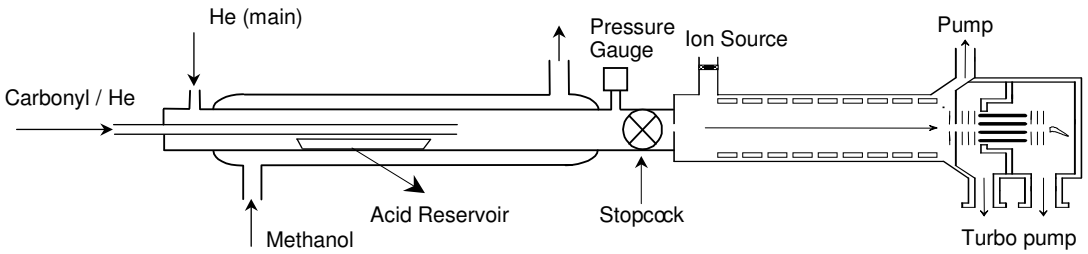

Figure 4.1. Schematic representation of the flow reactor coupled to the ion drift–chemical ionization mass spectrometry ID–CIMS).

Octanal (Avocado Research Chemical Ltd., 98%) and 2, 4-hexadienal (Aldrich, 95%) was used as received without further purification. A sample containing the aldehyde was placed in a temperature bath to regulate the concentration in the flow reactor. The vapor pressure of octanal and 2, 4-hexadienal under different bath temperature was estimated from *the CRC handbook* [2003]. The aldehyde purity was checked by ID–CIMS. The aldehyde vapor was introduced into the flow reactor through

a movable injector. The partial pressure of octanal and 2, 4-hexadienal in the flow reactor was estimated to be on the order of 10^{-7} Torr.

Commercially available methylglyoxal as a 40% aqueous solution (Aldrich) existed primarily in its monohydrate and dihydrate forms. To obtain the unpolymerized and water-free form, the following procedure was used: ca 20 ml of methylglyoxal aqueous solution was pumped under vacuum overnight in a flask covered with a black cloth in order to remove water and to prevent slow decomposition by room light [*Gurnick et al.,* 1981]. The resulting highly viscous and dark liquid was rapidly heated up to at least 180^{o}C until only a black and crispy residue remained. The distillate passed subsequently through columns containing anhydrous calcium sulfate ($CaSO_4$) and phosphorous pentoxide (P_2O_5) and was collected in a dry-ice trap (~ -78 ^{o}C). Freshly prepared methylglyoxal (green-yellowish liquid) was pumped at the temperature of dry ice for at least 30 min before use to remove impurities such as CO, H_2CO, and acetic acid from the sample. Purity of methylglyoxal was checked by the ID–CIMS before an uptake experiment. The saturation vapor pressure (P^0) of methylglyoxal was determined by [*Mackay et al.,* 1982; *Schwarzenbach,* 1993]

$$\ln\left(\frac{P^0}{760}\right) = \frac{\Delta S_{vap}(T_b)}{R}\left[1.8\left(1-\frac{T_b}{T}\right)+0.8\ln\left(\frac{T_b}{T}\right)\right] \ (torr) \qquad (4.1)$$

where R is the molar gas constant (8.314 J mol^{-1} K^{-1}), ΔS_{vap} is the entropy of vaporization (in J mol^{-1} K^{-1}), T_b is the boiling point and T is the temperature of the dry ice – acetone bath for the methylglyoxal bubbler (in K). ΔS_{vap} was calculated using a modified Trouton's method [*Zhao and Yalkowsky,* 1999; *Zhao et al.,* 1999] and boiling

points T_b were taken from the literature values [*CRC handbook,* 2003]. Methylglyoxal vapor was introduced into the flow reactor by a movable injector and its partial pressure in the flow reactor was estimated to be on the order of 10^{-6} to 10^{-7} Torr on the basis of the calculated vapor pressure.

The proton transfer reaction with H_3O^+ was used to detect gaseous carbonyls,

$$H_3O^+ + X \rightarrow XH^+ + H_2O \qquad (4.2)$$

where X and XH^+ denote the aldehyde and its protonated form, respectively. Octanal, 2, 4-hexadienal and methylglyoxal were monitored at their protonated peaks ($C_8H_{16}OH^+$(*m/z* = 129), $C_6H_8OH^+$(*m/z* = 97) and $CH_3COCHOH^+$(*m/z* = 73)), respectively. Figure 4.2 depicts mass spectra of the reagent ions and the methylglyoxal sample, showing the dominant $CH_3COCHOH^+$ peak along with trace protonated mono- and di-hydrates ($C_3H_4O_2 \bullet H_3O^+$, $C_3H_4O_2 \bullet (H_2O)_2H^+$) (*m/z* = 91 and 109, respectively).

Heterogeneous uptake of trace species into liquid droplets or aerosol particles involves several transport and kinetic processes including (1) gas-phase diffusion to the surface; (2) mass accommodation on the surface; (3) evaporation from the surface; (4) chemical reactions in the surface; (5) liquid-phase diffusion into bulk liquid or in the interfacial region; (6) solvation; and (7) liquid-phase chemical reactions in the condensed phase [*Molina et al.,* 1996]. A schematic representation of these processes (ignoring interfacial reactions and diffusion) is shown in Figure 4.3, and Figure 4.4 illustrates a simple resistance model (analogue to electric circuit), showing the key processes governing the trace species heterogeneous uptake by liquid droplets or aerosol particles. The overall heterogeneous processes can be described as uptake coefficient (γ),

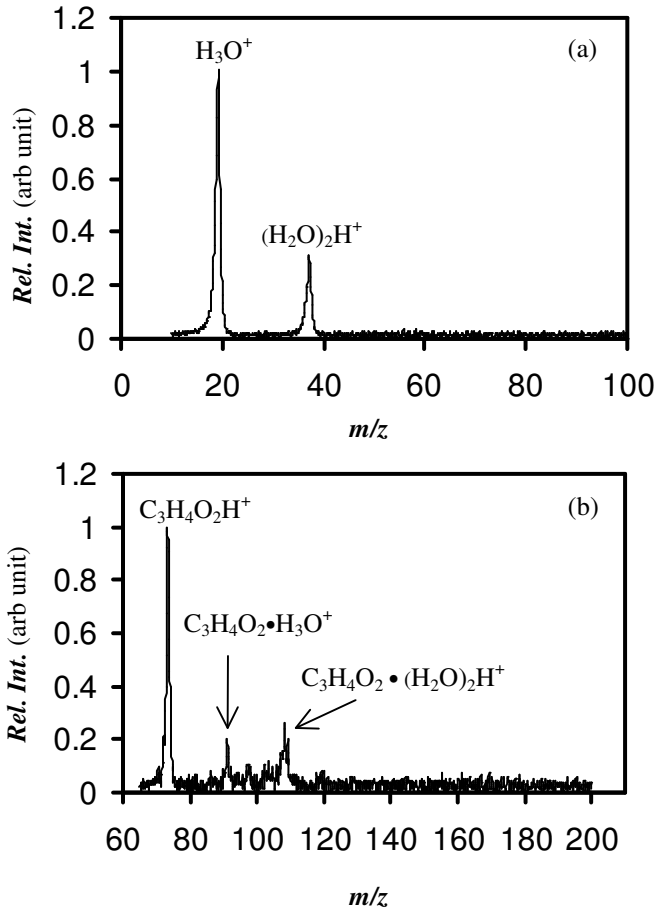

Figure 4.2. Spectral scans for the reagent ions (a, *m/z* = 10~100) and protonated methylgloxal (b, *m/z* = 60~200) for a typical experimental condition (before an uptake experiment).

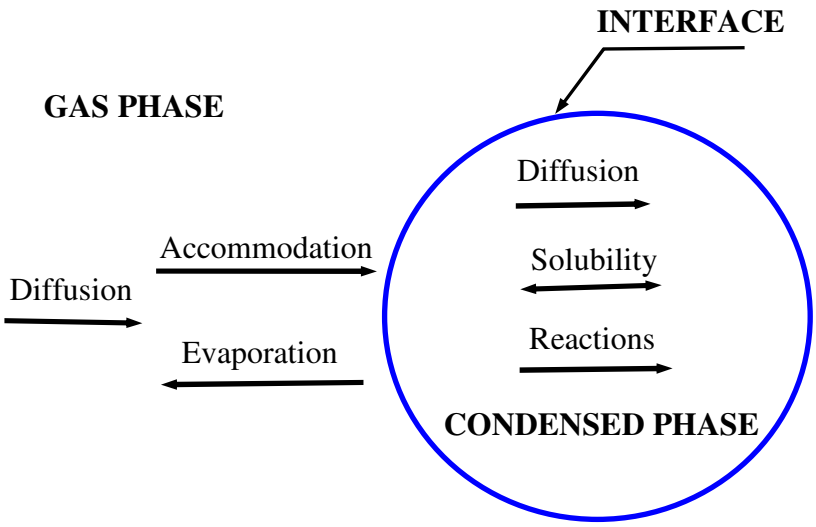

Figure 4.3. Schematic representations of kinetic processes of heterogeneous uptake of trace species into liquid droplets or aerosol particles

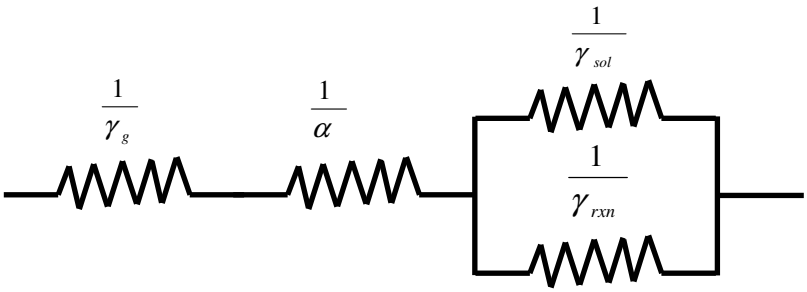

Figure 4.4. A simple resistance model of the kinetic processes shown in Figure 4.3.

$$\gamma = \frac{number\ \ of\ \ gas\ \ molecules\ \ removed\ \ in\ \ the\ \ condensed\ \ phase}{number\ \ of\ \ gas\ \ molecules\ \ colliding\ \ with\ \ the\ \ condensed\ \ phase} \quad (4.3)$$

The overall resistance model can be expressed as

$$\frac{1}{\gamma} = \frac{1}{\alpha} + \frac{1}{\gamma_g} + \frac{1}{\gamma_{sol} + \gamma_{rxn}} \quad (4.4)$$

The resistances $1/\gamma_g$, $1/\alpha$, $1/\gamma_{sol}$, $1/\gamma_{rxn}$ correspond to gas-phase diffusion, mass accommodation, liquid solubility and reactions in the condensed phase, respectively. We define mass accommodation coefficient α as the probability that a molecule enters the condensed phase upon colliding with the surface,

$$\alpha = \frac{number\ \ of\ \ gas\ \ molecules\ \ absorbed\ \ by\ \ the\ \ condensed\ \ phase}{number\ \ of\ \ gas\ \ molecules\ \ colliding\ \ with\ \ the\ \ condensed\ \ phase}$$

The term α can have a value between 0 and 1. The gas transport coefficient γ_g, the solubility coefficients γ_{sol}, and the reactive coefficient γ_{rxn} are normalized rates and can have values larger than unity. The gas phase transport resistance $1/\gamma_g$ is formulated as

$$\frac{1}{\gamma_g} = \frac{\omega d}{8 D_g} - \frac{1}{2} \quad (4.5)$$

Where ω is the mean thermal speed of the molecules, D_g is the gas-phase diffusion coefficient and d is the droplet or particle diameter. The term (-1/2) accounts for distortion of the Boltzmann collision rate when there is net gas uptake at the surface [*Molina et al.,* 1996]. The solubility and reactive coefficient are expressed as

$$\gamma_{sol} = \frac{4HRT}{\omega}\left(\frac{D_l}{\pi t}\right)^{1/2} \quad (4.6)$$

$$\gamma_{rxn} = \frac{4HRT}{\omega}(D_l k_1)^{1/2} \quad (4.7)$$

Where H is the Henry's law solubility constant, R is gas constant, D_l is the liquid-phase diffusion coefficient, k_1 is the liquid-phase reaction rate, and t is the gas/liquid exposure time.

Heterogeneous uptake of carbonyls on sulfuric acid using the asymmetrical flow tube reactor in this study can be treated with the above resistive model. Under low-pressure (~ 1 Torr) laminar flow conditions, the gas-phase diffusion has been omitted since its contribution is negligible for an uptake coefficient of $\gamma < 0.04$ in this study. The underestimation of the uptake coefficient without the gas-phase diffusion was estimated to be less than 20% for $\gamma < 0.04$. Then the model equation is simplified as

$$\frac{1}{\gamma} = \frac{1}{\alpha} + \frac{1}{\gamma_{sol} + \gamma_{rxn}} \tag{4.8}$$

The time-dependent uptake coefficient can be further expressed as [*Jayne et al.,* 1996]

$$1/\gamma(t) = a + bt^{1/2} \tag{4.9}$$

where a is a constant related to the accommodation coefficient and time-independent aqueous reaction rate constant and $b = \omega/4H^*RT(D_l/\pi)^{1/2}$. H^* is the effective Henry's law solubility constant. Hence the time-dependent uptake coefficient permits an estimate of the effective Henry's Law Constant. On the other hand, the uptake coefficient was calculated from the initial and time-dependent signals of the aldehyde

$$\gamma(t) = \frac{4k}{\omega}\left(\frac{V}{A}\right) \tag{4.10}$$

where V is the volume of the flow reactor, A is the geometric area of the exposed acid. The first-order rate coefficient (k) is related to the fractional change ($\Delta n/n$) in the gas-

phase concentration of the adsorbed/reactive molecule before and after exposure to sulfuric acid by

$$k = \frac{2F_g}{rA}\left(\frac{\Delta n}{n}\right) \tag{4.11}$$

where F_g is the carrier gas volume flow rate ($cm^3\ s^{-1}$).

To estimate the liquid-phase diffusion coefficient, we adopted a method suggested by *Klassen et al.* [1998]. The diffusion coefficient in liquid is given by

$$D_l = \frac{cT}{\eta} \tag{4.12}$$

Where T is the temperature, η is the temperature and composition dependent viscosity of liquid [*Williams and Long,* 1995]. c is a constant determined from the molar volume of solute with Le Bas additivity rules. For the species A in sulfuric acid, *Wilke and Chang* [1955] empirically calculated the value of c by

$$c = \frac{7.4\times10^{-8}(\kappa_{solvent})^{1/2}}{V_A^{0.6}} \tag{4.13}$$

where $\kappa_{solvent}$ is a solvent dependent empirical factor (e.g. $\kappa_{solvent}$ = 64 for sulfuric acid) and VA is Le Bas molar volume of solute A at its normal boiling temperature. V_A for octanal, and methylglyoxal is 185, 74 $cm^3\ mole^{-1}$, respectively and the corresponding c is 2.6 x 10^{-8}, 4.5 x 10^{-8} cm^2, respectively. From the time-dependent uptake curve, we can estimate the effective Henry's law solubility. For irreversible chemical loss, the following procedure was adopted to obtain the time-independent uptake coefficient. Initially, the movable injector was placed downstream of the vessel containing sulfuric acid. When the signal of the carbonyl became stable, the movable injector was then

moved upstream in a certain interval (e.g. 3 cm) to expose the carbonyl vapor to sulfuric acid solution. The decay of the signal (S) was then plotted as a function of the position of the movable injector (Z) relative to the initial downstream position (Z = 0). If the decay follows pseudo-first order, then the slope of the linear regression was determined by

$$slope = uk = \frac{\Delta \ln c}{\Delta Z} = \frac{\Delta \ln S}{\Delta Z} \tag{4.14}$$

The concentration of the carbonyl was proportional to the signal so that the relation Δlnc = ΔlnS was held. The pseudo-first order rate constant (k) was then determined and the uptake coefficient was calculated by using equation (4.10).

4.3 Results and Discussion

4.3.1 Heterogeneous chemistry of octanal and 2,4-hexadienal with sulfuric acid

Uptake measurements were performed by exposing a certain length of the acid to the aldehyde vapor, while monitoring the aldehyde signal using the ID-CIMS. Adsorption and desorption to/from the liquid phase were evident from the decline and recovery in the aldehyde signal, respectively. Figure 4.5 shows temporal profiles of octanal as it was repeatedly exposed and not exposed to a 20 cm length of a 81 wt % sulfuric acid at 273 K. The gaseous octanal concentration dropped instantly upon exposure to H_2SO_4 and returned to its original value as the H_2SO_4 liquid was saturated. Terminating the exposure resulted in an opposite peak due to desorption. The shapes of adsorption and desorption were identical, suggesting that octanal was physically taken up by H_2SO_4 without undergoing irreversible aqueous-phase reactions. Similar uptake was observed over the H_2SO_4 content of 60–85 wt % and at temperatures of 250-298K.

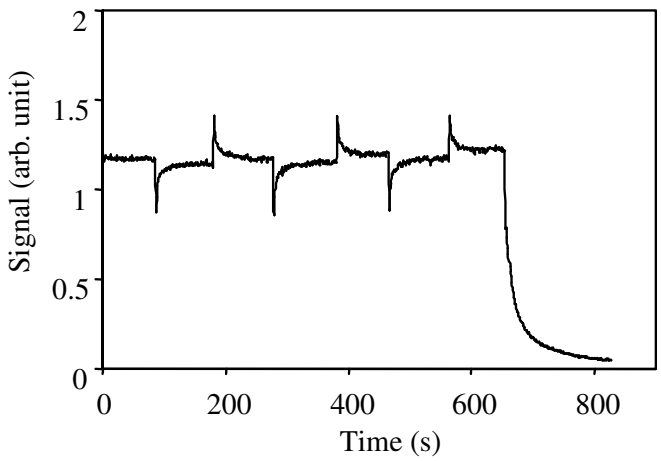

Figure 4.5. Temporal profiles of octanal when repeatedly exposed and not exposed to a 20 cm length of sulfuric acid. The acid content of H_2SO_4 was estimated to be 81 wt %. Experimental conditions are T = 273 K, P = 1.0 Torr. The octanal flow was terminated after 650 s.

From the data displayed in Figure 4.5, the time-dependent uptake coefficients were calculated from the initial and time-dependent octanal signals. Figure 4.6a shows a plot of γ_{obs} as a function of time. The uptake coefficient is initially large but decreases rapidly with time, indicating saturation at longer time. Shown in Figure 4.6b is a plot of $1/\gamma_{obs}$ versus $t^{½}$, with a calculated H^* value of 3650 M atm^{-1} from the best fit of the data. The measured H^* of octanal in H_2SO_4 increased when the acidity increased and temperature decreased (Table 4.1). The increasing H^* with acidity reflects an enhanced aldol condensation, to be discussed below. Octanal uptake on H_2SO_4 resembles the reversible loss of acetone on H_2SO_4 (< 75 wt %), except that the H^* value is much

smaller than that of acetone in sulfuric acid (1.8×10^5 M atm^{-1} for 75 wt % H_2SO_4 at 273 K) [*Kane et al.,* 1999]. In concentrated H_2SO_4 (>75 wt %), acetone was found to undergo irreversible reactions identified by the reaction products, mesityl oxide and trimethyl benzene [*Duncan et al.,* 1998; *Kane et al.,* 1999].

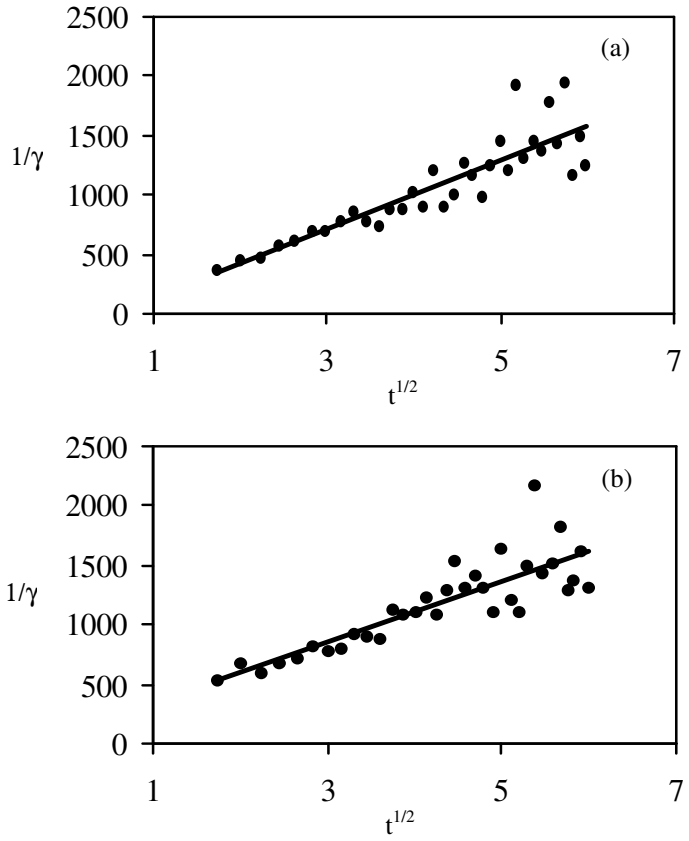

Figure 4.6. Plot of 1/γ as a function of $t^{1/2}$ for (a) data displayed in Figure 4.5, (b) 1/γ as an acid content of 65.1 wt % at T = 273 K and P = 1.1 Torr. H* is determined to be 3650 and 2450 M atm^{-1} for (a) and (b), respectively.

Table 4.1. Summary of H^* Measurements for Octanal in H_2SO_4. Each Point is the Average of at Least Three Measurements and the Error Corresponds to One Standard Deviation (1σ).

T (K)	H_2SO_4 (wt %)	H (M atm^{-1})
263	59	2212 ± 298
263	79	6004 ± 414
273	61	2337 ± 338
273	81	4519 ± 710
283	65	2133 ± 325
283	81	3707 ± 161
296	67	2257 ± 100
296	80	2323 ± 366

To further survey the aqueous reactions between octanal and H_2SO_4, we performed an additional series of experiments by mixing equal volumes (~1 mL) of octanal and H_2SO_4 at room temperature. The experiment with 80 wt % H_2SO_4 displayed the change of color and formation of products, in contrast to the 40 and 60 wt % solutions. Mixing of octanal and 80 wt % H_2SO_4 (both colorless) yielded initially a light yellow solution. A portion of the solution subsequently turned dark brown. Addition of H_2O (1–3 mL) to the octanal/H_2SO_4 mixture changed the color back to light yellow, suggesting a reversible process. Such a color change is well known to be characteristic of aldol condensation of carbonyls in acidic media [*Liler,* 1971]. For most carbonyl compounds, initial protonation and enolization result in aldol condensation (Figure 4.7), which in high acidity leads to formation of long-chain unsaturated polymers, responsible for the discoloration of the solutions [*Liler,* 1971]. Aldol condensation increases with

acidity [*Liler,* 1971], explaining larger uptake and higher *H** values of octanal in more concentrated H_2SO_4.

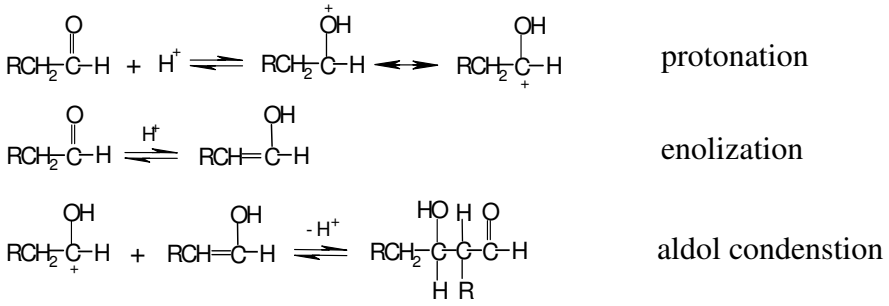

Figure 4.7. Mechanistic presentation of aldol condensation of octanal and 2, 4-hexadienal in sulfuric acid solution.

Figure 4.8 depicts uptake measurements of 2, 4-hexadienal on two H_2SO_4 solutions: (a) 66 wt % at 283 K and (b) 82 wt % at 296 K. Loss of 2, 4-hexadienal on H_2SO_4 was more pronounced than that of octanal. For 82 wt % H_2SO_4 at 296 K, the uptake exhibited little saturation on the time scale of the experiment, indicating an irreversible chemical process. For 66 wt % H_2SO_4 at 283 K, the uptake decreased rapidly at shorter times upon the exposure, but an irreversible loss was evident at longer time. The reversible and irreversible features of 2, 4-hexadienal on H_2SO_4 were also evident in the desorption peaks. Figure 4.9 demonstrates the loss of 2, 4-hexadienal as a function of the injector position when the injector was withdrawn at a 3 cm length interval. For 66 wt % H_2SO_4 the equilibrium value in the 2, 4-hexadienal signal was employed to derive the uptake coefficient. Both decays followed pseudo-first order kinetics, with the γ

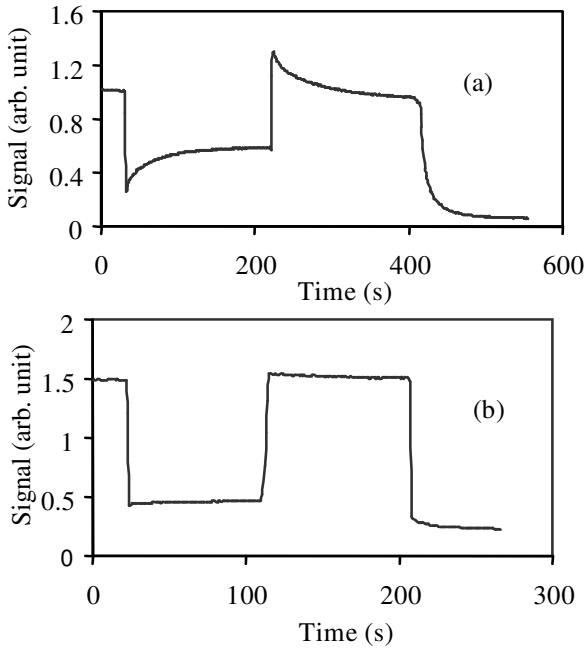

Figure 4.8. Temporal profiles of 2, 4-hexadienal when exposed and not exposed to a 20 cm length of sulfuric acid. The acid content of H_2SO_4 is 66 wt % for (a) and 82 wt % for (b). Experimental conditions are T = 283 K, P = 1.1 Torr for (a) and T = 296 K, P = 1.1 Torr for (b). The 2,4-hexadienal flow was terminated after 400 s for (a) and 200 s for (b).

values of 9.7 x 10^{-3} for 66 wt % H_2SO_4 at 283 K and 3.1 x 10^{-2} for 82 wt % H_2SO_4 at 296 K. Results of the uptake coefficient of 2, 4-hexadienal on sulfuric acid are summarized in Table 4.2, showing an increasing uptake coefficient with acidity.

Results of mixing 2, 4-hexadienal and sulfuric acid at room temperature were also performed. No change of color was observed for the 40 wt % solution. For 60 and 80 wt % H_2SO_4, the color of the entire mixture turned dark brown immediately after mixing. Black solid precipitation quickly formed, and the amount of solid formed increased with acidity. H_2O addition to the darkened 2, 4-hexadienal/sulfuric acid

mixtures caused a color change to light yellow. For the 60 wt % H_2SO_4, some precipitated solid dissolved upon H_2O addition, but little dissolved for 80 wt % H_2SO_4. Interestingly, for the 80 wt % solution, addition of acetone did not cause dissolution of the black solid. Those observations are also consistent with aldol condensation which in high acidity leads to formation of highly unsaturated polymers and ultimately precipitable solid products. The formation of highly unsaturated polymers appears to account for the irreversible loss of 2, 4-hexadienal in sulfuric acid (Figure 4.8), although the gaseous reactant concentration used in the uptake experiment was too low to allow observation of the precipitable products in the liquid.

Previous environmental chamber studies have suggested that acid-catalyzed heterogeneous reactions of carbonyls including octanal and 2, 4-hexadienal are responsible for measured SOA mass increases [*Jang et al.,* 2003]. Several aqueous reaction mechanisms have been proposed to explain the measurements, including hydration, hemiacetal and acetal formation, polymerization, and aldol condensation. For

Table 4.2. Summary of γ Values of 2,4-hexadienal in H_2SO_4. Each Point is the Average of at Least Three Measurements and the Error Corresponds to One Standard Deviation (1σ).

T (K)	H_2SO_4 (wt %)	γ
263	61	0.0076 ± 0.0007
273	81	0.0343 ± 0.0092
273	64	0.0083 ± 0.0023
283	81	0.0362 ± 0.0065
283	68	0.0091 ± 0.0017
296	81	0.0310 ± 0.0012

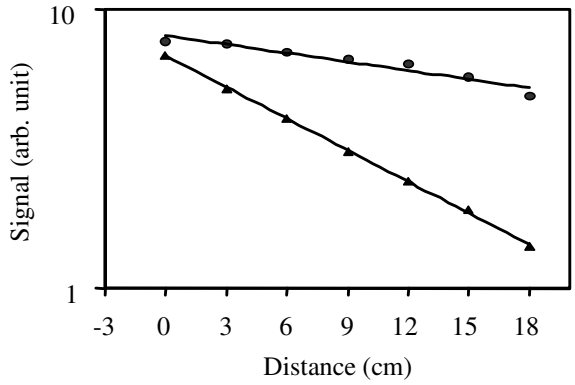

Figure 4.9. Intensity of 2,4-hexadienal as a function of injector distance. The solid circles represent uptake on 66 wt % H_2SO_4 with the experimental conditions similar to those in Figure 4.8a The solid triangles represent uptake on 82 wt % H_2SO_4 with the experimental conditions similar to those in Figure 4.8b.

octanal and 2, 4-hexadienal, hydration and polymerization are expected to be unimportant since the equilibrium constant for hydration decreases rapidly as the size of the aldehyde increases [*Betterton and Hoffmann,* 1988] and the water activity in H_2SO_4 is small. Our measurements show reversible uptake and decreasing H^* with acidity for octanal in 60 to 80 wt % H_2SO_4. For 2, 4-hexadienal, irreversible uptake was observed, and the measured uptake coefficient decreased considerably with decreasing acidity. Our observed interaction (in the uptake and mixing experiments) of octanal and 2, 4-hexadienal with H_2SO_4 is explained by aldol condensation and, in high acidity, further formation of high-unsaturated polymers. The conjugated 2, 4-hexadienal is more reactive in H_2SO_4, because protonation of conjugated carbonyls leads to resonance

stabilization which increases the basicity [e.g., *Zalewski and Dunn,* 1969]. In the troposphere the acidity of sulfate aerosols changes drastically with altitudes (or temperatures), ranging from 60-80 wt % in the upper troposphere to less than 1 wt % in the lower troposphere (assuming pH = 3 at 298 K) [*Zhang et al.,* 1993a]. The heterogeneous interaction of those carbonyls can be important in the upper troposphere where sulfate aerosols are more concentrated. Since the measured uptake of octanal and 2, 4-hexadienal decreases rapidly with acidity, aldol condensation and subsequent formation of highly unsaturated polymers from both species is likely less important in the lower troposphere.

4.3.2 Heterogeneous chemistry of methylglyoxal with sulfuric acid

The uptake measurements were performed at various concentrations of sulfuric acid and temperatures to investigate the heterogeneous chemistry of methylglyoxal. Uptake of methylglyoxal on H_2SO_4 exhibited distinct patterns, depending on the acidity and temperature. The concentration of methylglyoxal in the gas phase dropped considerably upon exposure to 80 wt % H_2SO_4 and later returned close to its original value as the H_2SO_4 liquid was saturated (Figure 4.10a). Terminating the methylglyoxal exposure resulted in an opposite peak due to desorption. The shapes of adsorption and desorption were nearly identical, suggesting that methylglyoxal was primarily taken up reversibly, although some methylglyoxal appeared to remain in the solution due to a small irreversible uptake. In contrast, loss of methylglyoxal on H_2SO_4 was more pronounced on 58 wt % H_2SO_4 (Figure 4.10b). The uptake showed little saturation on the time scale of the experiment, indicating an irreversible chemical loss. The uptake on

68 wt % H_2SO_4 exhibited an intermediate behavior compared to those on 80 and 58 wt % H_2SO_4, consisting of noticeable reversible and irreversible components (Figure 4.10c).

The time-dependent uptake coefficients were calculated from the initial and time-dependent methylglyoxal signals. Plots of the inverse uptake coefficient against the square root of time are shown in Figures 4.11a and 4.11c. The line fitted to the data in Figure 4.11a extrapolated closely to the origin, consistent with reversible uptake under high acidity. Extrapolation of the fitting line in Figure 4.11c showed an offset from the origin, because of a reactive loss. The effective Henry law's constant (H^*) was determined from the slope of the linear least-square fit of the data (eq. 4.9) and summarized in Table 4.3. The measured H^* depended on both temperature and acidity, increasing with decreasing temperature and decreasing acidity. The H^* value increased from 6.7 x 10^3 to 25 x 10^3 M atm^{-1} for 80 to 64 wt % H_2SO_4 at 273 K, while for 68-69 wt % H_2SO_4 H^* increased from 15 x 10^3 to 34 x 10^3 M atm^{-1} from 273 to 263 K. The H^* value of 2600 M atm^{-1} for 81 wt % H_2SO_4 at room temperature was smaller than that of 3700 M atm^{-1} previously reported for methylglyoxal in pure water solution [*Betterton and Hoffmann,*1988]. For the irreversible uptake, the decay of the methylglyoxal signal followed pseudo-first order kinetics; a time-independent uptake coefficient of 7.6 x 10^{-3} was obtained from Figure 4.11b. A recent study of reactive uptake of glyoxal on acidic aerosols reported uptake coefficients of 8.0 x 10^{-4} to 7.3 x 10^{-3} at room temperature [*Liggio et al.,* 2005].

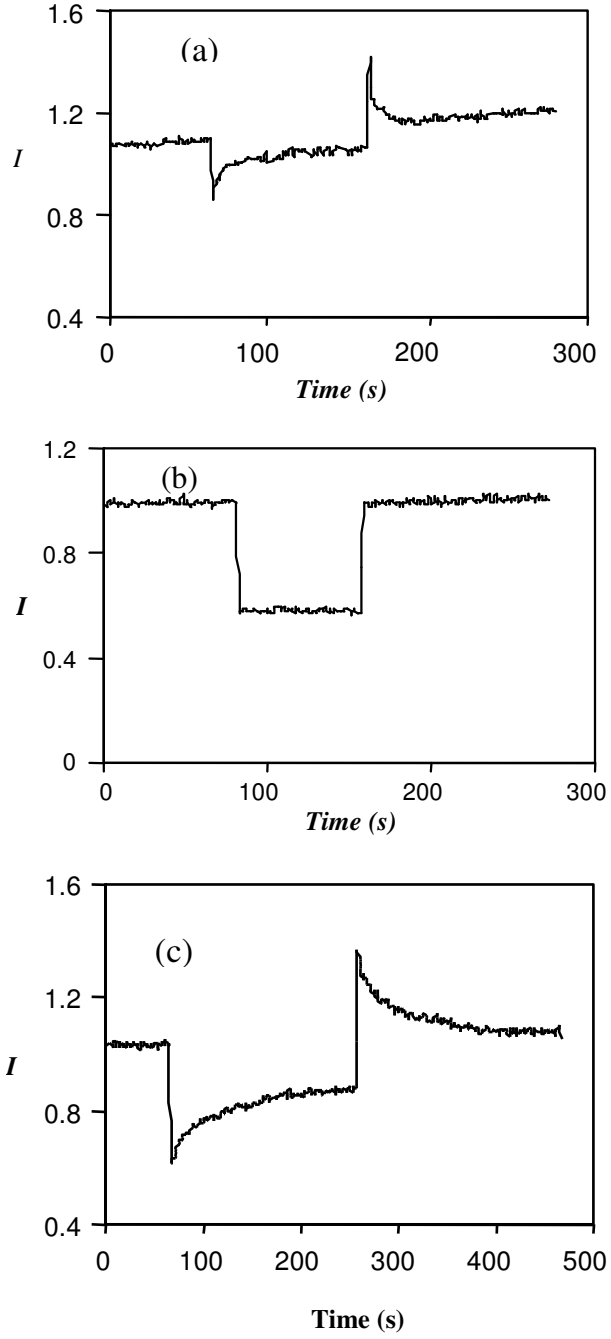

Figure 4.10. Temporal profiles (I, intensity) of methylgloxal when exposed to a 20 cm length of a vessel containing (a) a 80 wt % H_2SO_4 at T = 273 K, (b) a 58 wt % H_2SO_4 at T = 253 K (c) 68 wt % H_2SO_4 at T = 263 K.

For a given temperature, the uptake of methylglyoxal on H_2SO_4 decreased with acidity, indicating a dependence on water activity. This implies that aqueous reactions of methylglyoxal in H_2SO_4 are dominated by hydration and subsequent polymerization. The amount of available water in the solution impacts the equilibrium between the free (unhydrated) and hydrated forms of methylglyoxal. In concentrated H_2SO_4, the small water activity hinders hydration and further polymerization reactions, corresponding to a solubility-limited reversible uptake. In dilute H_2SO_4 with large water activity, the equilibrium is shifted nearly completely toward the hydrated forms of methylglyoxal, with a negligible reversible reaction. In our experiments, the partial pressure of methylglyoxal was very low (on the order of 10^{-6} to 10^{-7} Torr) so that uptake of methylglyoxal did not change appreciably the water activity in the solution. Subsequent polymerization reactions lead to formation of low-vapor pressure oligomers that remain in the aqueous-phase, explaining the irreversible uptake in dilute H_2SO_4.

Plausible mechanisms of the aqueous reactions of methylglyoxal in H_2SO_4 are depicted in Figure 4.12, showing hydration reactions and formation of various oligomers. Initial dissolution and hydration of methylglyoxal (**1**) result in the diol formation (**2**), and further hydration produces a tetrol (**3**). These two hydrates have been identified as the major forms in pure water solution, consisting of 56-62% for monohydrate (diol) and 38-44% for dihydrate (tetrol) [*Nemet et al.,* 2004]. Acetal polymerization with methylglyoxal as the main monomer unit leads to formation of acetal polymers (**4** and **5**). Alternatively, self-reactions and cross-reactions between diols and/or tetrols produce other oligomers. Evidence has been provided for the formation of dimers (**6**, **8**, and **10**)

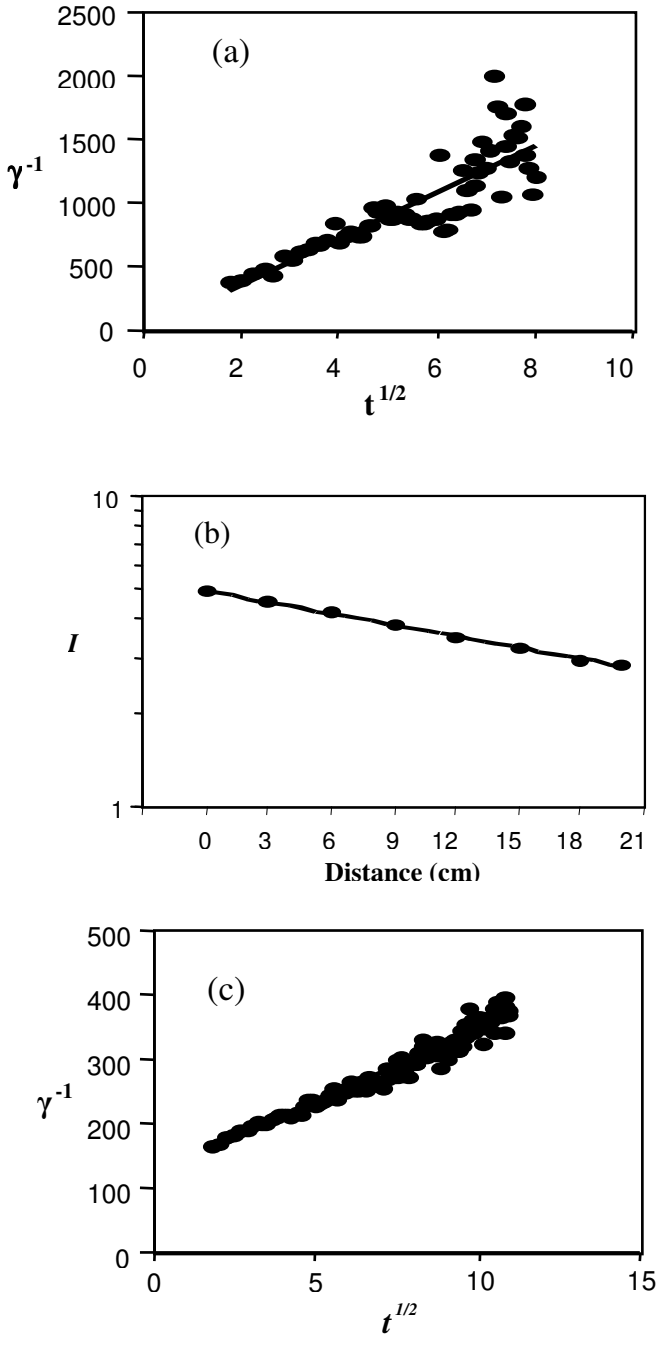

Figure 4.11. Plots of 1/γ vs t½, corresponding to Figure 4.10.

Table 4.3. Summary of H^* for Methylglyoxal in H_2SO_4. Each Point Averages Over at Least Three Measurements.

T (K)	H_2SO_4 (wt %)	H^*(x 10^3 M atm^{-1})
253	79	55.5 ± 13.7
263	68	33.6 ± 6.4
263	79	21.2 ± 6.5
273	64	24.9 ± 2.0
273	69	15.2 ± 3.2
273	80	6.7 ±1.6
283	73	5.9 ± 0.1
283	80	4.0 ± 0.9
296	81	2.6 ± 0.2

and cyclic trimer (**12**) in aqueous methylglyoxal solution [*Nemet et al.,* 2004]. The self-reaction of tetrols (**3**) or diols (**2**) results in the formation of a cyclic dimer (**6**) or a non-cyclic dimer (**10**), respectively. The cross-reaction between diols and tetrols leads to the formation of a dimer (**8**). The formation of a cyclic trioxane (**12**) is attributable to a termolecular reaction of diols (**2**). The produced dimers (**6**, **8**, and **10**) or a trimer (**12**) further engage in reactions with diols or tetrols, yielding higher oligomers (e.g., **7**, **9**, **11**, and **13**). In addition, cyclic oligomers **6** and **7** are likely formed from hydration of **10** and **11**, followed by cyclization of **8** and **9**, respectively.

Polymers were identified as major components in atmospheric organic aerosols from photooxidation of aromatic compounds in the environmental chamber experiments [*Kalberer et al.,* 2004]. Measurements using laser desorption ionization – mass spectrometry (LDI-MS) confirmed the formation of oligomers up to nonamer (i.e., *via* **3**, **4**, and **5**) in aqueous solution of methylglyoxal; other mass peaks were also identified

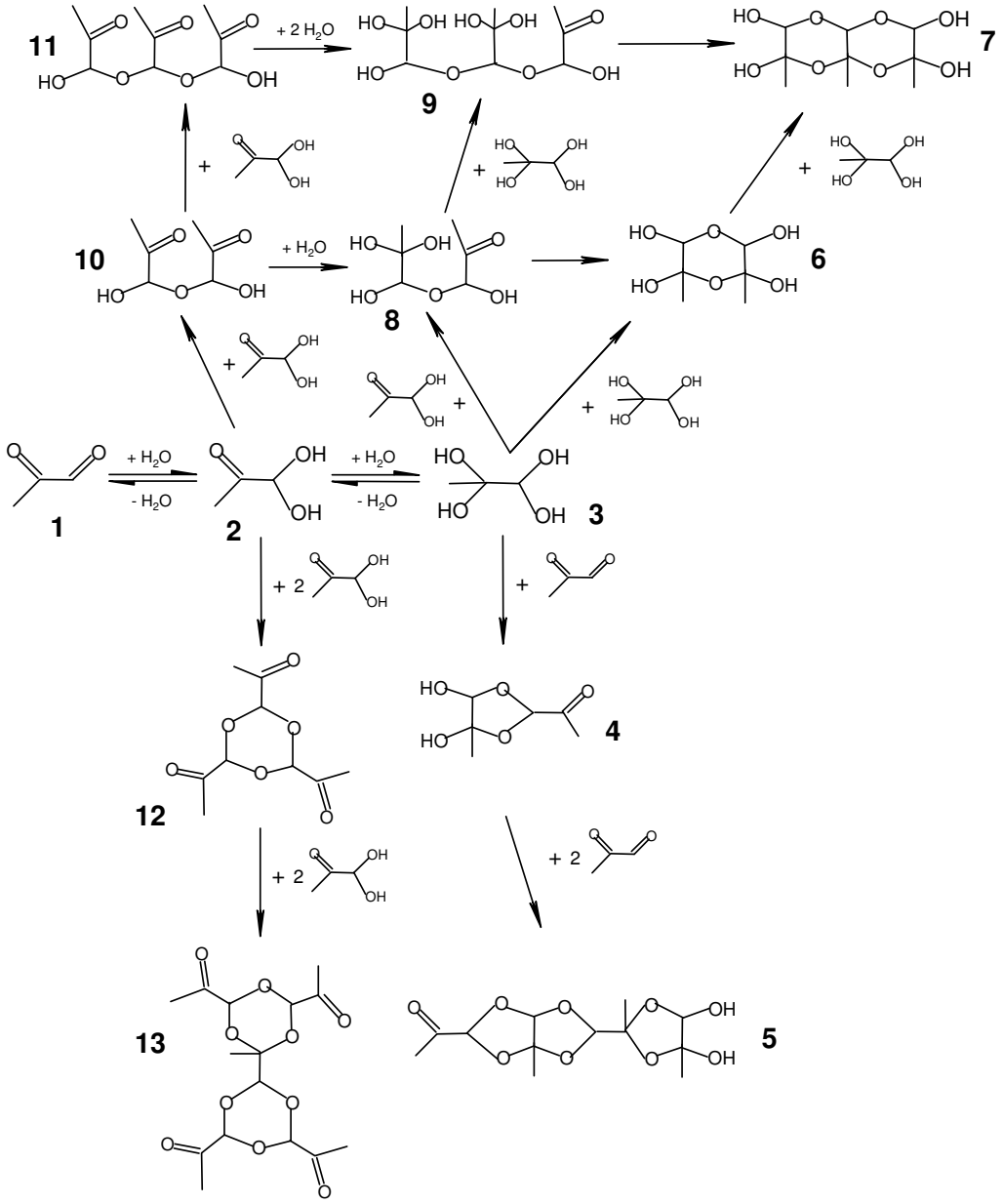

Figure 4.12. Possible aqueous reaction mechanism of methylglyoxal in H_2SO_4.

likely to be formed from polymerization of **5**, **7**, **9**, or **11** [*Kalberer et al.,* 2004]. For an analogue α-dicarbonyl, acetal polymer structures represent the dominant forms of oligomers in aqueous glyoxal solutions between 1 and 10 M [*Whipple,* 1970]. Esterification of alcohols by sulfuric acid also occurs at room temperature in bulk solution [*Garner et al.,* 1950; *Deno and Newman,* 1950; *Clark and Williams,* 1957]. *Liggio et al.* [2005a, b] have identified formation of low volatile acetals and sulfate esters in the aerosol phase for the heterogeneous reaction of glyoxal on aerosol particles. *Surratt et al.* [2007] have identified organosulfate esters from photooxidation of alpha-pinene and isoprene. We did not observe an irreversible uptake of methylglyoxal in concentrated H_2SO_4, suggesting that the reactions of the hydrated methylglyoxal or oligomers containing the alcohol functional group with sulfuric acid was negligible compared to hydration and polymerization.

The uptake of methylglyoxal in H_2SO_4 was distinct from those of larger aldehydes. For example, the interaction of octanal and 2,4-hexadienal with H_2SO_4 has been explained by aldol condensation that increases with acidity [*Zhao et al.,* 2005]. While with negligible hydration rates, octanal, 2,4-hexadienal, and other high molecular weight carbonyl compounds undergo primarily protonation and enolization, which are then followed by aldol condensation and formation of large unsaturated polymers in high acidity. In contrast, the smaller α-dicarbonyls (e.g., glyoxal and methylgloxal) generally correspond to large hydration rates, leading to aqueous reactions such as hydration, polymerization, even in the absence of an acidic media. The heterogeneous reactions of α-dicarbonyls in acidic aerosols were proposed to be acid-catalyzed [*Jang et al.,* 2002].

We found little evidence for acid-catalyzed reactions of methylglyoxal, since in concentrated H_2SO_4 (high H^+ concentrations) the uptake decreased dramatically with the acidity.

4.4 Summary

The uptake measurements of octanal and 2, 4-hexadienal in H_2SO_4 permit direct assessment of the interaction between the aldehyde and H_2SO_4. Octanal was physically absorbed by sulfuric acid without undergoing irreversible reaction, and the measured Henry's constant decreases with decreasing acidity and increasing temperature. Irreversible uptake characteristic of chemical reactions was observed for 2, 4-hexadienal and the uptake coefficient decreased with decreasing acidity. The mixing experiments provide additional evidence for the nature of the interaction between aldehyde and H_2SO_4, confirming the occurrence of aldol condensation and in concentrated solutions formation of high-unsaturated polymers. The heterogeneous interaction of those carbonyls can be important in the upper troposphere where sulfate aerosols are more concentrated. In the lower troposphere, however, aldol condensation and subsequent formation of high-unsaturated polymers of carbonyl compounds may not be a significant contributor to SOA formation, since the aerosol acidity is small.

We have investigated the heterogeneous chemistry of methylglyoxal with liquid H_2SO_4 over the temperature range of 250-298 K and acidic range of 55-85 wt %. This study provides direct assessment of the heterogeneous interaction between methylglyoxal and H_2SO_4. We have reported the first measurements of heterogeneous uptake of methylglyoxal on liquid H_2SO_4. From the time-dependent uptake the effective

Henry's law solubility constant (H^*) was determined. Uptake of methylglyoxal on sulfuric acid decreases with acidity. Hydration and polymerization likely explain our measured uptake of methylglyoxal in H_2SO_4. The measurements did not show an acid-catalyzed uptake of methylglyoxal and revealed negligible sulfate esterification of methylglyoxal in H_2SO_4. Our results suggest that heterogeneous reactions of methylglyoxal likely contribute to SOA formation in slightly acidic media and hydration and polymerization of methylglyoxal in the atmospheric aerosol-phase are dependent on the hygroscopicity, rather than the acidity of the aerosols. Because a low-pressure fast flow reactor was used in the present work, the sulfuric acid concentrations used were rather high.

CHAPTER V

SUMMARY

Aerosol particles have profound impact on human health, atmospheric radiation, and cloud microphysics and these impacts are strongly dependent on the particle sizes. However, large uncertainties still exist regarding the formation, growth, distribution and the physical and chemical properties of aerosols. Formation and growth of atmospheric particles is an important topic and also an active research area in atmospheric chemistry. In this work, laboratory and theoretical studies have been performed to investigate the formation and growth of particles in the atmosphere focusing on (1) Laboratory investigation of new particle formation and growth; (2) Theoretical study of complexes and clusters of the atmospheric nucleating precursors and (3) Laboratory investigation of heterogeneous interactions of atmospheric carbonyls with sulfuric acid. The nucleation zone was characterized by the concentration distribution and distribution of the saturation ratio of sulfuric acid along the condenser. The nucleation rate was found to be dependent on the concentration of the precursors and the number of precursor molecules in the critical cluster is thus determined according to this dependence. The nucleation rate was considerably enhanced in the presence of ppt level of cis-pinonic acid or ammonia. Results from quantum chemical calculations and quantum theory of atoms in molecules (QTAIM) reveal that formation of strong hydrogen-bonding between organic acid and sulfuric acid is likely responsible for a reduction of the nucleation barrier by modifying the hydrophobic properties of the organic acid and allowing further addition of hydrophilic species such as sulfuric acid, water, and possibly ammonia to the

hydrophilic side of the complex. This promotes growth of the nascent cluster to overcome the nucleation barrier and continual growth by condensation and thus enhances the nucleation in the atmosphere. Molecular dynamic simulation has been performed to look into the time evolution and estimate the size of the clusters.

Direct measurement has been performed to investigate heterogeneous uptake of atmospheric carbonyls on sulfuric acid using a laminar flow reactor coupled to the ID-CIMS. Important parameters (e.g., uptake coefficients and Henry's Law constants) have been obtained from the time-dependent or time-independent uptake profiles. The results indicated that the acid-catalyzed reactions of larger aldehydes (e.g. octanal and 2,4-hexadienal) in sulfuric acid solution were attributed to aldol condensation in high acidity. However such reactions do not contribute much to SOA formation due to the low acidity under tropospheric conditions. On the other hand, heterogeneous reactions of light dicarbonyls such as methylglyoxal likely contribute to SOA formation in slightly acidic media. The reactions of methylglyoxal in the atmospheric aerosol-phase involve hydration and subsequent polymerization, which are dependent on the hygroscopicity, rather than the acidity of the aerosols.

REFERENCES

Al Natsheh, A., A. B. Nadykto, K. V. Mikkelsen, F. Q. Yu, and J. Ruuskanen (2004), Sulfuric acid and sulfuric acid hydrates in the gas phase: A DFT investigation, *J. Phys. Chem. A*, *108*, 8914-8929.

Alabugin, I. V., M. Manoharan, S. Peabody, and F. Weinhold (2003), Electronic basis of improper hydrogen bonding: A subtle balance of hyperconjugation and rehybridization, *J. Am. Chem. Soc.*, *125*, 5973-5987.

Alley, W. M. (2001), Ground water and climate, *Ground Water*, *39*, 161-161.

Arstila, H., K. Laasonen, and A. Laaksonen (1998), Ab initio study of gas-phase sulphuric acid hydrates containing 1 to 3 water molecules, *J. Chem. Phys.*, *108*, 1031-1039.

Atkinson, R. (1990), Gas-phase tropospheric chemistry of organic-compounds - A review, *Atmos. Environ., A Gen. topics*, *24*, 1-41.

Bader, R. F. W. (1990), *Atoms in molecules: A quantum theory*, 438 p., Clarendon Press, Oxford.

Bader, R. F. W., T. H. Tang, Y. Tal, and F. W. Bieglerkonig (1982), Properties of atoms and bonds in hydrocarbon molecules, *J. Am. Chem. Soc.*, *104*, 946-952.

Ball, S. M., D. R. Hanson, F. L. Eisele, and P. H. McMurry (1999), Laboratory studies of particle nucleation: Initial results for H_2SO_4, H_2O, and NH_3 vapors, *J. Geophys. Res.-Atmos*, *104*, 23709-23718.

Bandy, A. R., and J. C. Ianni (1998), Study of the hydrates of H_2SO_4 using density functional theory, *J. Phys. Chem. A*, *102*, 6533-6539.

Becker, R., and W. Doring (1935), Kinetic treatment of germ formation in supersaturated vapour, *Annalen Der Physik*, *24*, 719-752.

Berndt, T., O. Boge, T. Conrath, F. Stratmann, and J. Heintzenberg (2000), Formation of new particles in the system $H_2SO_4(SO_3)/H_2O/(NH_3)$ - First results from a flow-tube study, *J. Aerosol Sci.*, *31*, 554-555.

Berndt, T., O. Boge, and F. Stratmann (2006), Formation of atmospheric H_2SO_4/H_2O particles in the absence of organics: A laboratory study, *Geophys. Res. Lett.*, *33*, L15817, doi:10.1029/2006GL026660.

Berndt, T., O. Boge, F. Stratmann, J. Heintzenberg, and M. Kulmala (2005), Rapid formation of sulfuric acid particles at near-atmospheric conditions, *Science*, *307*, 698-700.

Betterton, E. A., and M. R. Hoffmann (1988), Henry law constants of some environmentally important aldehydes, *Environ. Sci. Technol.*, *22*, 1415-1418.

Biegler-Konig, F. (2000), Calculation of atomic integration data, *J. Comput. Chem.*, *21*, 1040-1048.

Biegler-Konig, F., and J. Schonbohm (2002), Update of the AIM2000-program for atoms in molecules, *J. Comput. Chem.*, *23*, 1489-1494.

Biegler-Konig, F., J. Schonbohm, and D. Bayles (2001), Software news and updates - AIM2000 - A program to analyze and visualize atoms in molecules, *J. Comput. Chem.*, *22*, 545-559.

Bieglerkonig, F. W., R. F. W. Bader, and T. H. Tang (1982), Calculation of the average properties of atoms in molecules .2., *J. Comput. Chem.*, *3*, 317-328.

Bilde, M., and S. N. Pandis (2001), Evaporation rates and vapor pressures of individual aerosol species formed in the atmospheric oxidation of alpha- and beta-pinene, *Environ. Sci. Technol.*, *35*, 3344-3349.

Bostanov, V., E. Mladenova, and D. Kashchiev (2000), Nucleation rate in electrocrystallization of cadmium on the Cd(0001) crystal face, *J. Electroanal. Chem.*, *481*, 7-12.

Boulaud, D., G. Madelaine, and D. Vigla (1977), Experimental-study on nucleation of water-vapor sulfuric-acid binary-system, *J. Chem. Phys.*, *66*, 4854-4860.

Boy, M., U. Rannik, K. E. J. Lehtinen, V. Tarvainen, H. Hakola, and M. Kulmala (2003), Nucleation events in the continental boundary layer: Long-term statistical analyses of aerosol relevant characteristics, *J. Geophys. Res.-Atmos*, *108*, 4667, doi:10.1029/2003JD003838.

Capouet, M., and J. F. Muller (2006), A group contribution method for estimating the vapour pressures of alpha-pinene oxidation products, *Atmos. Chem. Phys.*, *6*, 1455-1467.

Cardenas, L. M., D. J. Brassington, B. J. Allan, H. Coe, B. Alicke, U. Platt, K. M. Wilson, J. M. C. Plane, and S. A. Penkett (2000), Intercomparison of formaldehyde measurements in clean and polluted atmospheres, *J. Atmos. Chem., 37*, 53-80.

Carslaw, K. S., S. L. Clegg, and P. Brimblecombe (1995), A Thermodynamic model of the System HCl-HNO_3-H_2SO_4-H_2O, including solubilities of HBr, from less than 200 to 328 K, *J. Phys. Chem.*, *99*, 11557-11574.

Charlson, R. J., J. E. Lovelock, M. O. Andreae, and S. G. Warren (1987), Oceanic phytoplankton, atmospheric sulfur, cloud albedo and climate, *Nature*, *326*, 655-661.

Charlson, R. J., J. H. Seinfeld, A. Nenes, M. Kulmala, A. Laaksonen, and M. C. Facchini (2001), Atmospheric science - Reshaping the theory of cloud formation, *Science*, *292*, 2025-2026.

Chen, D. R., D. Y. H. Pui, D. Hummes, H. Fissan, F. R. Quant, and G. J. Sem (1998), Design and evaluation of a nanometer aerosol differential mobility analyzer (Nano-DMA), *J. Aerosol Sci., 29*, 497-509.

Cheng, M. T., and Y. I. Tsai (2000), Characterization of visibility and atmospheric aerosols in urban, suburban, and remote areas, *Sci. Total Environ.*, *263*, 101-114.

Clark, D. J., and G. Williams (1957), Esterification by sulphuric acid .2. Ethyl alcohol, *J. Chem. Soc.*, 4218-4221.

Coffman, D. J., and D. A. Hegg (1995), A preliminary-study of the effect of ammonia on particle nucleation in the marine boundary-layer, *J. Geophys. Res.-Atmos*, *100*, 7147-7160.

Couling, S. B., J. Fletcher, A. B. Horn, D. A. Newnham, R. A. McPheat, and R. G. Williams (2003), First detection of molecular hydrate complexes in sulfuric acid aerosols, *PCCP*, *5*, 4108-4113.

Curtiss, L. A., and M. Blander (1988), Thermodynamic properties of gas-phase hydrogen-bonded complexes, *Chem. Rev.*, *88*, 827-841.

Curtius, J., R. Weigel, H. J. Vossing, H. Wernli, A. Werner, C. M. Volk, P. Konopka, M. Krebsbach, C. Schiller, A. Roiger, H. Schlager, V. Dreiling, and S. Borrmann (2005),

Observations of meteoric material and implications for aerosol nucleation in the winter Arctic lower stratosphere derived from in situ particle measurements, *Atmos. Chem. Phys.*, *5*, 3053-3069.

Deno, N. C., and M. S. Newman (1950), Mechanism of sulfation of alcohols, *J. Am. Chem. Soc.*, *72*, 3852-3856.

Ding, C. G., and K. Laasonen (2004), Partially and fully deprotonated sulfuric acid in $H_2SO_4(H_2O)(n)$ (n=6-9) clusters, *Chem. Phys. Lett.*, *390*, 307-313.

Ding, C. G., K. Laasonen, and A. Laaksonen (2003), Two sulfuric acids in small water clusters, *J. Phys. Chem. A*, *107*, 8648-8658.

Doyle, G. J. (1961), Self-nucleation in sulfuric acid-water system, *J. Chem. Phys.*, *35*, 795-799.

Drossinos, Y., and P. G. Kevrekidis (2003), Classical nucleation theory revisited, *Phys. Rev. E*, *67*, 026127.

Duncan, J. L., L. R. Schindler, and J. T. Roberts (1998), A new sulfate-mediated reaction: Conversion of acetone to trimethylbenzene in the presence of liquid sulfuric acid, *Geophys. Res. Lett.*, *25*, 631-634.

Eisele, F. L., and D. R. Hanson (2000), First measurement of prenucleation molecular clusters, *J. Phys. Chem. A*, *104*, 830-836.

Eisele, F. L., M. D. Perkins, and E. W. Mcdaniel (1981), Measurement of the mobilities of Cl^-, $NO_2^-.H_2O$, $NO_3^-.H_2O$, $CO_3^-.H_2O$, and $CO_4^-.H_2O$ in N_2 as a function of temperature, *J. Chem. Phys.*, *75*, 2473-2475.

Eisele, F. L., and D. J. Tanner (1993), Measurement of the gas-phase concentration of H_2SO_4 and methane sulfonic-acid and estimates of H_2SO_4 production and loss in the atmosphere, *J. Geophys. Res.-Atmos*, *98*, 9001-9010.

Emmeluth, C., and M. A. Suhm (2003), A chemical approach towards the spectroscopy of carboxylic acid dimer isomerism, *PCCP*, *5*, 3094-3099.

Fan, J. W., and R. Y. Zhang (2006), Atmospheric oxidation mechanism of p-xylene: A density functional theory study, *J. Phys. Chem. A*, *110*, 7728-7737.

Fan, J. W., J. Zhao, and R. Y. Zhang (2005), Theoretical study of OH addition to alpha-pinene and beta-pinene, *Chem. Phys. Lett.*, *411*, 1-7.

Farkas, L. (1927), The speed of germinitive formation in over saturated vapours., *Z.Fur Phys. Chem.*, *125*, 236-242.

Fiacco, D. L., S. W. Hunt, and K. R. Leopold (2002), Microwave investigation of sulfuric acid monohydrate, *J. Am. Chem. Soc.*, *124*, 4504-4511.

Finlayson-Pitts, B. J., and J. N. Pitts (2000), *Chemistry of the upper and lower atmosphere : theory, experiments and applications*, xxii, 969 p., Academic Press, San Diego, CA.

Fortner, E. C., J. Zhao, and R. Y. Zhang (2004), Development of ion drift-chemical ionization mass spectrometry, *Anal. Chem.*, *76*, 5436-5440.

Frisch, M. J., G. W. Trucks, H. B. Schlegel, G. E. Scuseria,M. A. Robb, J. R. Cheeseman, J. A. Montgomery, Jr., T. Vreven, K. N. Kudin, J. C. Burant, J. M. Millam, S. S. Iyengar, J. Tomasi, V. Barone, B. Mennucci, M. Cossi, G. Scalmani, N. Rega, G. A. Petersson, H. Nakatsuji, M. Hada, M. Ehara, K. Toyota, R. Fukuda, J.

Hasegawa, M. Ishida, T. Nakajima, Y. Honda, O. Kitao, H. Nakai, M. Klene, X. Li, J. E. Knox, H. P. Hratchian, J. B. Cross, C. Adamo, J. Jaramillo, R. Gomperts, R. E. Stratmann, O. Yazyev, A. J. Austin, R. Cammi, C. Pomelli, J. W. Ochterski, P. Y. Ayala, K. Morokuma, G. A. Voth, P. Salvador, J. J. Dannenberg, V. G. Zakrzewski, S. apprich, A. D. Daniels, M. C. Strain, O. Farkas, D. K. Malick, A. D. Rabuck, K. Raghavachari, J. B. Foresman, J. V. Ortiz, Q. Cui, A. G. Baboul, S. Clifford, J. Cioslowski, B. B. Stefanov, G. Liu, A. Liashenko, P. Piskorz, I. Komaromi, R. L. Martin, D. J. Fox, T. Keith, M. A. Al-Laham, C. Y. Peng, A. Nanayakkara, M. Challacombe, P. M. W. Gill, B. Johnson, W. Chen, M. W. Wong, C. Gonzalez, and J. A. Pople (2003), *Gaussian 03, Revision B.05,* Gaussian, Inc., Pittsburgh, PA.

Fuller, E. N., P.D. Schettle, and J. C. Giddings (1966), A new method for prediction of binary gas-phase diffusion coeffecients, *Ind. Eng. Chem.*, *58*, 19-24.

Gao, S., M. Keywood, N. L. Ng, J. Surratt, V. Varutbangkul, R. Bahreini, R. C. Flagan, and J. H. Seinfeld (2004), Low-molecular-weight and oligomeric components in secondary organic aerosol from the ozonolysis of cycloalkenes and alpha-pinene, *J. Phys. Chem. A*, *108*, 10147-10164.

Garland, R. M., M. J. Elrod, K. Kincaid, M. R. Beaver, J. L. Jimenez, and M. A. Tolbert (2006), Acid-catalyzed reactions of hexanal on sulfuric acid particles: Identification of reaction products, *Atmos. Environ.*, *40*, 6863-6878.

Garner, H. K., and H. J. Lucas (1950), Preparation and hydrolysis of some acetals and esters of D(-)-2,3-butanediol, *J. Am. Chem. Soc.*, *72*, 5497-5501.

Gilli, P., V. Bertolasi, V. Ferretti, and G. Gilli (1994), Covalent nature of the strong homonuclear hydrogen-bond - Study of the O-H---O system by crystal-structure correlation methods, *J. Am. Chem. Soc.*, *116*, 909-915.

Gilli, P., V. Bertolasi, L. Pretto, and G. Gilli (2006), Outline of a transition-state hydrogen-bond theory, *J. Mol. Struct.*, *790*, 40-49.

Glasius, M., M. Lahaniati, A. Calogirou, D. Di Bella, N. R. Jensen, J. Hjorth, D. Kotzias, and B. R. Larsen (2000), Carboxylic acids in secondary aerosols from oxidation of cyclic monoterpenes by ozone, *Environ. Sci. Technol.*, *34*, 1001-1010.

Gora, R. W., S. J. Grabowski, and J. Leszczynski (2005), Dimers of formic acid, acetic acid, formamide and pyrrole-2-carboxylic acid: An ab initio study, *J. Phys. Chem. A*, *109*, 6397-6405.

Granby, K., C. S. Christensen, and C. Lohse (1997), Urban and semi-rural observations of carboxylic acids and carbonyls, *Atmos. Environ.*, *31*, 1403-1415.

Grosjean, D., A. H. Miguel, and T. M. Tavares (1990), Urban air-pollution in Brazil - Acetaldehyde and other carbonyls, *Atmos. Environ. B-Urb*, *24*, 101-106.

Guenther, A., C. N. Hewitt, D. Erickson, R. Fall, C. Geron, T. Graedel, P. Harley, L. Klinger, M. Lerdau, W. A. Mckay, T. Pierce, B. Scholes, R. Steinbrecher, R. Tallamraju, J. Taylor, and P. Zimmerman (1995), A global-model of natural volatile organic-compound emissions, *J. Geophys. Res.-Atmos*, *100*, 8873-8892.

Gurnick, M., J. Chaiken, T. Benson, and J. D. Mcdonald (1981), Vibrational and rotational spectroscopy of the 1st electronically allowed transition of alpha-dicarbonyls, *J. Chem. Phys.*, *74*, 99-105.

Handbook of chemistry and physics, 83rd edition (2003), (Ed.: David R Lide) CRC press, New York.

Hanson, D. R., and F. Eisele (2000), Diffusion of H_2SO_4 in humidified nitrogen: Hydrated H_2SO_4, *J. Phys. Chem. A*, *104*, 1715-1719.

Hanson, D. R., and F. L. Eisele (2002), Measurement of prenucleation molecular clusters in the NH_3, H_2SO_4, H_2O system, *J. Geophys. Res.-Atmos*, *107*, 4158, doi:10.1029/2001JD001100.

Heist, R. H., and H. Reiss (1974), Hydrates in supersaturated binary sulfuric acid water vapor, *J. Chem. Phys.*, *61*, 573-581.

Ho, S. S. H., J. Z. Yu, K. W. Chu, and L. L. Yeung (2006), Carbonyl emissions from commercial cooking sources in Hong Kong, *J. Air Waste Mange.*, *56*, 1091-1098.

Horvath, H. (1995), Size segregated light-absorption coefficient of the atmospheric aerosol, *Atmos. Environ.*, *29*, 875-883.

Ianni, J. C., and A. R. Bandy (1999), A density functional theory study of the hydrates of NH_3 center dot H_2SO_4 and its implications for the formation of new atmospheric particles, *J. Phys. Chem. A*, *103*, 2801-2811.

Ianni, J. C., and A. R. Bandy (2000), A theoretical study of the hydrates of $(H_2SO_4)_2$ and its implications for the formation of new atmospheric particles, *J.Mol. Struct. - Theochem*, *497*, 19-37.

Iraci, L. T., and M. A. Tolbert (1997), Heterogeneous interaction of formaldehyde with cold sulfuric acid: Implications for the upper troposphere and lower stratosphere, *J. Geophys. Res.-Atmos*, *102*, 16099-16107.

IPCC (2007), Working group I to the fourth assessment report of the Intergovernmental Panel on Climate Change, Paris.

Jaeckervoirol, A., P. Mirabel, and H. Reiss (1987), Hydrates in supersaturated binary sulfuric acid-water vapor - A reexamination, *J. Chem. Phys.*, *87*, 4849-4852.

Jaenicke, R., and T. Hanusch (1993), Simulation of the optical-particle counter forward scattering spectrometer probe-100 (FSSP-100) - Consequences for size distribution measurements, *Aerosol Sci. Technol.*, *18*, 309-322.

Jang, M., N. M. Czoschke, and A. L. Northcross (2004), Atmospheric organic aerosol production by heterogeneous acid-catalyzed reactions, *Chem. Phys. Chem.*, *5*, 1647-1661.

Jang, M., S. Lee, and R. M. Kamens (2003), Organic aerosol growth by acid-catalyzed heterogeneous reactions of octanal in a flow reactor, *Atmos. Environ.*, *37*, 2125-2138.

Jang, M. S., N. M. Czoschke, S. Lee, and R. M. Kamens (2002), Heterogeneous atmospheric aerosol production by acid-catalyzed particle-phase reactions, *Science*, *298*, 814-817.

Jayne, J. T., D. R. Worsnop, C. E. Kolb, E. Swartz, and P. Davidovits (1996), Uptake of gas-phase formaldehyde by aqueous acid surfaces, *J. Phys. Chem.*, *100*, 8015-8022.

Kalberer, M., D. Paulsen, M. Sax, M. Steinbacher, J. Dommen, A. S. H. Prevot, R. Fisseha, E. Weingartner, V. Frankevich, R. Zenobi, and U. Baltensperger (2004), Identification of polymers as major components of atmospheric organic aerosols, *Science*, *303*, 1659-1662.

Kanakidou, M., J. H. Seinfeld, S. N. Pandis, I. Barnes, F. J. Dentener, M. C. Facchini, R. Van Dingenen, B. Ervens, A. Nenes, C. J. Nielsen, E. Swietlicki, J. P. Putaud, Y. Balkanski, S. Fuzzi, J. Horth, G. K. Moortgat, R. Winterhalter, C. E. L. Myhre, K. Tsigaridis, E. Vignati, E. G. Stephanou, and J. Wilson (2005), Organic aerosol and global climate modelling: A review, *Atmos. Chem. Phys.*, *5*, 1053-1123.

Kane, S. M., R. S. Timonen, and M. T. Leu (1999), Heterogeneous chemistry of acetone in sulfuric, acid solutions: Implications for the upper troposphere, *J. Phys. Chem. A*, *103*, 9259-9265.

Kavouras, I. G., N. Mihalopoulos, and E. G. Stephanou (1998), Formation of atmospheric particles from organic acids produced by forests, *Nature*, *395*, 683-686.

Kim, T. O., T. Ishida, M. Adachi, K. Okuyama, and J. H. Seinfeld (1998), Nanometer-sized particle formation from $NH_3/SO_2/H_2O$/air mixtures by ionizing irradiation, *Aerosol Sci. Technol.*, *29*, 111-125.

Klassen, J. K., J. Lynton, D. M. Golden, and L. R. Williams (1999), Solubility of acetone in low-temperature (210-240 K) sulfuric acid solutions, *J. Geophys. Res.-Atmos*, *104*, 26355-26361.

Knutson, E. O., and K. T. Whitby (1975), Anomalous unipolar diffusion charging of polystyrene latex aerosols, *J. Colloid Interface Sci.*, *53*, 493-495.

Koch, S., R. Winterhalter, E. Uherek, A. Kolloff, P. Neeb, and G. K. Moortgat (2000), Formation of new particles in the gas-phase ozonolysis of monoterpenes, *Atmos. Environ.*, *34*, 4031-4042.

Kollman, P. A., and L. C. Allen (1972), Theory of hydrogen-bond, *Chem. Rev.*, *72*, 283-303.

Korhonen, P., M. Kulmala, A. Laaksonen, Y. Viisanen, R. McGraw, and J. H. Seinfeld (1999), Ternary nucleation of H_2SO_4, NH_3, and H_2O in the atmosphere, *J. Geophys. Res.-Atmos*, *104*, 26349-26353.

Kroll, J. H., N. L. Ng, S. M. Murphy, R. C. Flagan, and J. H. Seinfeld (2005), Secondary organic aerosol formation from isoprene photooxidation under high-NO_x conditions, *Geophys. Res. Lett.*, *32*, L18808, doi:10.1029/2005GL023637

Kulmala, M., A. Laaksonen, and L. Pirjola (1998), Parameterizations for sulfuric acid/water nucleation rates, *J. Geophys. Res.-Atmos*, *103*, 8301-8307.

Kulmala, M., K. E. J. Lehtinen, and A. Laaksonen (2006), Cluster activation theory as an explanation of the linear dependence between formation rate of 3nm particles and sulphuric acid concentration, *Atmos. Chem. Phys.*, *6*, 787-793.

Kulmala, M., H. Vehkamaki, T. Petajda, M. Dal Maso, A. Lauri, V. M. Kerminen, W. Birmili, and P. H. McMurry (2004), Formation and growth rates of ultrafine atmospheric particles: A review of observations, *J. Aerosol Sci., 35*, 143-176.

Kurdi, L., and E. Kochanski (1989), Theoretical-studies of sulfuric-acid monohydrate - Neutral or ionic Complex, *Chem. Phys. Lett.*, *158*, 111-115.

Kurten, T., M. R. Sundberg, H. Vehkamaki, M. Noppel, J. Blomqvist, and M. Kulmala (2006), Ab initio and density functional theory reinvestigation of gas-phase sulfuric acid monohydrate and ammonium hydrogen sulfate, *J. Phys. Chem. A*, *110*, 7178-7188.

Kurten, T., L. Torpo, C. G. Ding, H. Vehkamaki, M. R. Sundberg, K. Laasonen, and M. Kulmala (2007), A density functional study on water-sulfuric acid-ammonia clusters and implications for atmospheric cluster formation, *J. Geophys. Res.-Atmos*, *112*, D04210, doi:10.1029/2006JD007391.

Kurten, T., L. Torpo, M. R. Sundberg, V. M. Kerminen, H. Vehkamaki, and M. Kulmala (2007), Estimating the NH_3 : H_2SO_4 ratio of nucleating clusters in atmospheric conditions using quantum chemical methods, *Atmos. Chem. Phys.*, *7*, 2765-2773.

Larson, L. J., A. Largent, and F. M. Tao (1999), Structure of the sulfuric acid-ammonia system and the effect of water molecules in the gas phase, *J. Phys. Chem. A*, *103*, 6786-6792.

Lei, W. F., A. Derecskei-Kovacs, and R. Y. Zhang (2000), Ab initio study of OH addition reaction to isoprene, *J. Chem. Phys.*, *113*, 5354-5360.

Lei, W. F., and R. Y. Zhang (2000), Chlorine atom addition reaction to isoprene: A theoretical study, *J. Chem. Phys.*, *113*, 153-157.

Liggio, J., and S. M. Li (2006), Organosulfate formation during the uptake of pinonaldehyde on acidic sulfate aerosols, *Geophys. Res. Lett.*, *33*, L13808, doi:10.1029/2006GL026079.

Liggio, J., S. M. Li, and R. Mclaren (2005), Heterogeneous reactions of glyoxal on particulate matter: Identification of acetals and sulfate esters, *Environ. Sci. Technol.*, *39*, 1532-1541.

Liggio, J., S. M. Li, and R. Mclaren (2005), Reactive uptake of glyoxal by particulate matter, *J. Geophys. Res.-Atmos*, *110*, D10304, doi:10.1029/2004JD005113.

Liler, M. (1971), *Reaction mechanisms in sulphuric acid and other strong acid solutions*, xiii, 350 p., Academic Press, New York.

Loeffler, K. W., C. A. Koehler, N. M. Paul, and D. O. De Haan (2006), Oligomer formation in evaporating aqueous glyoxal and methyl glyoxal solutions, *Environ. Sci. Technol.*, *40*, 6318-6323.

Lothe, J., and G. M. Pound (1962), Reconsiderations of nucleation theory, *J. Chem. Phys.*, *36*, 2080-2085.

Lothe, J., and G. M. Pound (1969), Replacement factor in a linear chain, *Phys. Rev.*, *182*, 339-&.

Mackay, D., A. Bobra, D. W. Chan, and W. Y. Shiu (1982), Vapor-pressure correlations for low-volatility environmental chemicals, *Environ. Sci. Technol.*, *16*, 645-649.

Marrero, T. R., and R. H. Luecke (1996), Molecular gaseous diffusion coefficients of long chain alkanes, alcohols, esters and acids, *AlChE J.*, *42*, 2365-2368.

McGraw, R., and R. J. Weber (1998), Hydrates in binary sulfuric acid-water vapor: Comparison of CIMS measurements with the liquid-drop model, *Geophys. Res. Lett.*, *25*, 3143-3146.

McMurry, P. H., M. Fink, H. Sakurai, M. R. Stolzenburg, R. L. Mauldin, J. Smith, F. Eisele, K. Moore, S. Sjostedt, D. Tanner, L. G. Huey, J. B. Nowak, E. Edgerton, and D. Voisin (2005), A criterion for new particle formation in the sulfur-rich Atlanta atmosphere, *J. Geophys. Res.-Atmos*, *110*, D22S02, doi:10.1029/2005JD005901.

Mertes, S., F. Schroder, and A. Wiedensohler (1995), The particle-detection efficiency curve of the TSI-3010 CPC as a function of the temperature difference between saturator and condenser, *Aerosol Sci. Technol.*, *23*, 257-261.

Michelsen, R. R., S. F. M. Ashbourn, and L. T. Iraci (2004), Dissolution, speciation, and reaction of acetaldehyde in cold sulfuric acid, *J. Geophys. Res.-Atmos*, *109*, D23205, doi:10.1029/2004JD005041.

Molina, M. J., L. T. Molina, and C. E. Kolb (1996), Gas-phase and heterogeneous chemical kinetics of the troposphere and stratosphere, *Annu. Rev. Phys. Chem.*, *47*, 327-367.

Munger, J. W., D. J. Jacob, B. C. Daube, L. W. Horowitz, W. C. Keene, and B. G. Heikes (1995), Formaldehyde, glyoxal, and methylglyoxal in air and cloud water at a rural mountain site in central Virginia, *J. Geophys. Res.-Atmos*, *100*, 9325-9333.

Nadykto, A. B., and F. Q. Yu (2007), Strong hydrogen bonding between atmospheric nucleation precursors and common organics, *Chem. Phys. Lett.*, *435*, 14-18.

Nandi, C. K., M. K. Hazra, and T. Chakraborty (2005), Vibrational coupling in carboxylic acid dimers, *J. Chem. Phys.*, *123*, 24310.

Napari, I., M. Kulmala, and H. Vehkamaki (2002), Ternary nucleation of inorganic acids, ammonia, and water, *J. Chem. Phys.*, *117*, 8418-8425.

Napari, I., M. Noppel, H. Vehkamaki, and M. Kulmala (2002), An improved model for ternary nucleation of sulfuric acid-ammonia-water, *J. Chem. Phys.*, *116*, 4221-4227.

NCEA (1996), Air quality criteria for particulate matter, edited, National Center for Environmental Assessment, Office of Research and Development, U.S. Environmental Protection Agency, Research Triangle Park, NC.

Nemet, I., V. T. Drazen, and L. Varga-Defterdarovic (2004), Spectroscopic studies of methylglyoxal in water and dimethylsulfoxide. *Bioorg. Chem.*, *32*, 560-570.

Noppel, M. (1998), Binary nucleation of water-sulfuric acid system: A reexamination of the classical hydrates interaction model, *J. Chem. Phys.*, *109*, 9052-9056.

Noppel, M., H. Vehkamaki, and M. Kulmala (2002), An improved model for hydrate formation in sulfuric acid-water nucleation, *J. Chem. Phys.*, *116*, 218-228.

Nowak, J. B., L. G. Huey, A. G. Russell, D. Tian, J. A. Neuman, D. Orsini, S. J. Sjostedt, A. P. Sullivan, D. J. Tanner, R. J. Weber, A. Nenes, E. Edgerton, and F. C. Fehsenfeld (2006), Analysis of urban gas phase ammonia measurements from the 2002 Atlanta Aerosol Nucleation and Real-Time Characterization Experiment (ANARChE), *J. Geophys. Res.-Atmos*, *111*, D17308, doi:10.1029/2006JD007113.

Noziere, B., and D. D. Riemer (2003), The chemical processing of gas-phase carbonyl compounds by sulfuric acid aerosols-2,4-pentanedione, *Atmos. Environ.*, *37*, 841-851.

Ochterski, J. W. (2000), *Thermochemistry in Gaussian,* Gaussian Inc. Wallingford, CT.

O'Dowd, C. D., P. Aalto, K. Hameri, M. Kulmala, and T. Hoffmann (2002), Aerosol formation - Atmospheric particles from organic vapours, *Nature*, *416*, 497-498.

Pakiari, A. H., and K. Eskandari (2006), The chemical nature of very strong hydrogen bonds in some categories of compounds, *J. Mol. Struct. -Theochem*, *759*, 51-60.

Perkins, M. D., F. L. Eisele, and E. W. Mcdaniel (1981), Temperature-dependent mobilities NO_2^-,NO_3^-,CO_3^-,CO_4^-, and O_2^+ in O_2, *J. Chem. Phys.*, *74*, 4206-4207.

Perry, R. H., J. O. Maloney, D. W. Green, and Knovel (Firm) (1997), *Perry's chemical engineers' handbook,* McGraw-Hill, New York.

Rapaport, D. C. (2004), *The art of molecular dynamics simulation*, 2nd ed., xiii, 549 p., Cambridge University Press, Cambridge.

Re, S., Y. Osamura, and K. Morokuma (1999), Coexistence of neutral and ion-pair clusters of hydrated sulfuric acid $H_2SO_4(H_2O)_n$ (n=1-5) - A molecular orbital study, *J. Phys. Chem. A*, *103*, 3535-3547.

Reed, A. E., L. A. Curtiss, and F. Weinhold (1988), Intermolecular interactions from a natural bond orbital, donor-acceptor viewpoint, *Chem. Rev.*, *88*, 899-926.

Reiss, H. (1950), The kinetics of phase transitions in binary systems, *Phys.*, *18*, 840-848.

Reiss, H. (1977), Replacement free-energy in nucleation theory, *Adv. Colloid Interface Sci.*, *7*, 1-66.

Reiss, H., D. I. Margolese, and F. J. Schelling (1976), Experimental-study of nucleation in vapor mixtures of sulfuric-acid and water, *J. Colloid Interface Sci.*, *56*, 511-526.

Renninger, R. G., F. C. Hiller, and R. C. Bone (1981), Self-nucleation in the sulfuric acid-water system - Comment, *J. Chem. Phys.*, *75*, 1584-1585.

Salcedo, D., P. W. Villalta, V. Varutbangkul, J. C. Wormhoudt, R. C. Miake-Lye, D. R. Worsnop, J. O. Ballenthin, W. F. Thorn, A. A. Viggiano, T. M. Miller, R. C. Flagan, and J. H. Seinfeld (2004), Effect of relative humidity on the detection of sulfur

dioxide and sulfuric acid using a chemical ionization mass spectrometer, *Int. J. Mass Spectrom.*, *231*, 17-30.

Schoon, N., C. Amelynck, P. Bultinck, and E. Arijs (2002), Study of ion/molecule reactions of atmospherically important negative ions with methane sulfonic acid, *Int. J. Mass Spectrom.*, *221*, 209-218.

Schulz, H., V. Harder, A. Ibald-Mulli, A. Khandoga, W. Koenig, F. Krombach, R. Radykewicz, A. Stampfl, B. Thorand, and A. Peters (2005), Cardiovascular effects of fine and ultrafine particles, *J. Aerosol Med., 18*, 1-22.

Schwarzenbach, R. P. (1993), Organic contaminants in water, *Abs. Papers Am. Chem. Soc.*, *205*, 278-CHED.

Seaton, A., W. Macnee, K. Donaldson, and D. Godden (1995), Particulate air-pollution and acute health-effects, *Lancet*, *345*, 176-178.

Seinfeld, J. H., and S. N. Pandis (1998), *Atmospheric chemistry and physics: From air pollution to climate change*, xxvii, 1326 p., Wiley, New York.

Shugard, W. J., R. H. Heist, and H. Reiss (1974), Theory of vapor-phase nucleation in binary-mixtures of water and sulfuric-acid, *J. Chem. Phys.*, *61*, 5298-5305.

Sloth, M., M. Bilde, and K. V. Mikkelsen (2004), Interaction energies between aerosol precursors formed in the photo-oxidation of alpha-pinene, *Mol. Phys.*, *102*, 2361-2368.

Stolzenburg, M. R. (1988), An ultrafine aerosol size distribution measuring system, Ph.D. Dissertation, University of Minnesota, Minneapolis.

Su, T., and M. T. Bowers (1973), Ion-polar molecule collisions - Effect of molecular-size on ion-polar molecule rate constants, *J. Am. Chem. Soc.*, *95*, 7609-7610.

Su, T., and M. T. Bowers (1975), Parameterization of average dipole orientation theory - Temperature-dependence, *Int. J. Mass Spectrom. Ion Processes*, *17*, 211-212.

Suh, I., W. F. Lei, and R. Y. Zhang (2001), Experimental and theoretical studies of isoprene reaction with NO_3, *J. Phys. Chem. A*, *105*, 6471-6478.

Suh, I., D. Zhang, R. Y. Zhang, L. T. Molina, and M. J. Molina (2002), Theoretical study of OH addition reaction to toluene, *Chem. Phys. Lett.*, *364*, 454-462.

Suh, I., R. Y. Zhang, L. T. Molina, and M. J. Molina (2003), Oxidation mechanism of aromatic peroxy and bicyclic radicals from OH-toluene reactions, *J. Am. Chem. Soc.*, *125*, 12655-12665.

Suh, I., J. Zhao, and R. Y. Zhang (2006), Unimolecular decomposition of aromatic bicyclic alkoxy radicals and their acyclic radicals, *Chem. Phys. Lett.*, *432*, 313-320.

Surratt, J. D., J. H. Kroll, T. E. Kleindienst, E. O. Edney, M. Claeys, A. Sorooshian, N. L. Ng, J. H. Offenberg, M. Lewandowski, M. Jaoui, R. C. Flagan, and J. H. Seinfeld (2007), Evidence for organosulfates in secondary organic aerosol, *Environ. Sci. Technol.*, *41*, 517-527.

Takeoka, G., C. Perrino, and R. Buttery (1996), Volatile constituents of used frying oils, *J. Agric. Food. Chem.*, *44*, 654-660.

Tolocka, M. P., M. Jang, J. M. Ginter, F. J. Cox, R. M. Kamens, and M. V. Johnston (2004), Formation of oligomers in secondary organic aerosol, *Environ. Sci. Technol.*, *38*, 1428-1434.

Viehland, L. A., and D. W. Fahey (1983), The mobilities of NO_3^-, NO_2^-, NO^+, and Cl^- in N_2: A measure of inelastic energy-loss, *J. Chem. Phys.*, *78*, 435-441.

Viggiano, A. A., J. V. Seeley, P. L. Mundis, J. S. Williamson, and R. A. Morris (1997), Rate constants for the reactions of $XO_3^-(H_2O)(n)$ (X = C, HC, and N) and $NO_3^-(HNO_3)(n)$ with H_2SO_4: Implications for atmospheric detection of H_2SO_4, *J. Phys. Chem. A*, *101*, 8275-8278.

Viisanen, Y., M. Kulmala, and A. Laaksonen (1997), Experiments on gas-liquid nucleation of sulfuric acid and water, *J. Chem. Phys.*, *107*, 920-926.

Volmer, M., and A. Weber (1926), Germ-formation in oversaturated figures, *Z.Fur Phys. Chem.*, *119*, 277-301.

Wang, S. C., and R. C. Flagan (1990), Scanning electrical mobility spectrometer, *Aerosol Sci. Technol.*, *13*, 230-240.

Weber, R. J., P. H. McMurry, R. L. Mauldin, D. J. Tanner, F. L. Eisele, A. D. Clarke, and V. N. Kapustin (1999), New particle formation in the remote troposphere: A comparison of observations at various sites, *Geophys. Res. Lett.*, *26*, 307-310.

Wert, B. P., M. Trainer, A. Fried, T. B. Ryerson, B. Henry, W. Potter, W. M. Angevine, E. Atlas, S. G. Donnelly, F. C. Fehsenfeld, G. J. Frost, P. D. Goldan, A. Hansel, J. S. Holloway, G. Hubler, W. C. Kuster, D. K. Nicks, J. A. Neuman, D. D. Parrish, S. Schauffler, J. Stutz, D. T. Sueper, C. Wiedinmyer, and A. Wisthaler (2003), Signatures of terminal alkene oxidation in airborne formaldehyde measurements during TexAQS 2000, *J. Geophys. Res. -Atmos*, *108*, 4104, doi:10.1029/2002JD002502, 2003.

Whipple, E. B. (1970), Structure of glyoxal in water, *J. Am. Chem. Soc.*, *92*, 7183-7186.

Wilemski, G. (1984), Composition of the critical nucleus in multicomponent vapor nucleation, *J. Chem. Phys.*, *80*, 1370-1372.

Wilemski, G. (1987), Revised classical binary nucleation theory for aqueous alcohol and acetone vapors, *J. Phys. Chem.*, *91*, 2492-2498.

Wilke, C. R., and P. Chang (1955), Correlation of diffusion coefficients in dilute solutions, *AlChE J.*, *1*, 264-270.

Williams, L. R., and F. S. Long (1995), Viscosity of supercooled sulfuric-acid-solutions, *J. Phys. Chem.*, *99*, 3748-3751.

Winterhalter, R., R. Van Dingenen, B. R. Larsen, N. R. Jensen, and J. Hjorth (2003), LC-MS analysis of aerosol particles from the oxidation of α-pinene by ozone and OH radicals, *Atmos. Chem. Phys. Discuss*., 3, 1-39.

Wyslouzil, B. E., J. H. Seinfeld, R. C. Flagan, and K. Okuyama (1991), Binary nucleation in acid water-systems .2. Sulfuric acid-water and a comparison with methanesulfonic acid-water, *J. Chem. Phys.*, *94*, 6842-6850.

Yu, F. Q. (2005), Quasi-unary homogeneous nucleation of H_2SO_4-H_2O, *J. Chem. Phys.*, *122*, 074501.

Yu, F. Q. (2006), Effect of ammonia on new particle formation: A kinetic H_2SO_4-H_2O-NH_3 nucleation model constrained by laboratory measurements, *J. Geophys. Res.-Atmos*, *111*, D01204, doi:10.1029/2005JD005968.

Yu, F. Q., and R. P. Turco (2001), From molecular clusters to nanoparticles: Role of ambient ionization in tropospheric aerosol formation, *J. Geophys. Res.-Atmos*, *106*, 4797-4814.

Zalewski, R. I., and G. E. Dunn (1969), Protonation of conjugated carbonyl groups in sulfuric acid solutions .2. Protonation and basicity of alpha beta-unsaturated alicyclic ketones, *Can. J. Chem.*, *47*, 2263-&.

Zhang, D., and R. Zhang (2005), Ozonolysis of alpha-pinene and beta-pinene: Kinetics and mechanism, *J. Chem. Phys.*, *122*, 114308.

Zhang, D., and R. Y. Zhang (2002), Mechanism of OH formation from ozonolysis of isoprene: A quantum-chemical study, *J. Am. Chem. Soc.*, *124*, 2692-2703.

Zhang, D., R. Y. Zhang, and D. T. Allen (2003), C-C bond fission pathways of chloroalkenyl alkoxy radicals, *J. Chem. Phys.*, *118*, 1794-1801.

Zhang, R., M. T. Leu, and L. F. Keyser (1997), Heterogeneous chemistry of HO_2NO_2 in liquid sulfuric acid, *J. Phys. Chem. A*, *101*, 3324-3330.

Zhang, R., P. J. Wooldridge, J. P. D. Abbatt, and M. J. Molina (1993), Physical-chemistry of the H_2SO_4/H_2O binary-system at low-temperatures - Stratospheric implications, *J. Phys. Chem.*, *97*, 7351-7358.

Zhang, R. Y., I. Suh, J. Zhao, D. Zhang, E. C. Fortner, X. X. Tie, L. T. Molina, and M. J. Molina (2004), Atmospheric new particle formation enhanced by organic acids, *Science*, *304*, 1487-1490.

Zhang, R. Y., P. J. Wooldridge, and M. J. Molina (1993), Vapor-pressure measurements for the $H_2SO_4/HNO_3/H_2O$ and $H_2SO_4/HCl/H_2O$ Systems - Incorporation of stratospheric acids into background sulfate aerosols, *J. Phys. Chem.*, *97*, 8541-8548.

Zhao, J., and R. Y. Zhang (2004), Proton transfer reaction rate constants between hydronium ion (H_3O^+) and volatile organic compounds, *Atmos. Environ.*, *38*, 2177-2185.

Zhao, J., R. Y. Zhang, K. Misawa, and K. Shibuya (2005), Experimental product study of the OH-initiated oxidation of m-xylene, *J. Photochem. Photobio. A.*, *176*, 199-207.

Zhao, J., R. Y. Zhang, and S. W. North (2003), Oxidation mechanism of delta-hydroxyisoprene alkoxy radicals: Hydrogen abstraction versus 1,5 H-shift, *Chem. Phys. Lett.*, *369*, 204-213.

Zhao, L. W., P. Li, and S. H. Yalkowsky (1999), Predicting the entropy of boiling for organic compounds, *J. Chem. Inf. Comp. Sci.*, *39*, 1112-1116.

Zhao, L. W., N. Ni, and S. H. Yalkowsky (1999), A modification of Trouton's rule by simple molecular parameters for hydrocarbon compounds, *Ind. Eng. Chem. Res.*, *38*, 324-327.

VITA

Jun Zhao was born in 1971 in China. He received his B.E in chemical engineering in 1995 from the South China University of Technology. After four-years in an industrial career, he went back to the graduate school at the South China University of Technology, where he focused his research on the development of catalysts in application to the transformation of carbon dioxide to dimethyl carbonate. He joined Dr. Renyi Zhang's group at Texas A&M University in September 2001 and participated in several projects. To date, he has published papers in 11 peer-reviewed journals. He received his Ph.D. in December 2007. He can be reached at Department of Atmospheric Sciences, Texas A&M University, College Station, Texas 77843-3150.